

Tiago Carrilho Biló

The changing Brazil Current system between 23°S-31°S: vertical structure and mesoscale dynamics

(Corrected Version)

A thesis submitted in partial fulfillment of
the requirements for the degree of Master of
Sciences in Oceanography, with emphasis in
Physical Oceanography, *Instituto Oceanográfico, Universidade de São Paulo*.

Advisor: Prof. Dr. Ilson Carlos Almeida
da Silveira.

São Paulo
2015

Universidade de São Paulo

Instituto Oceanográfico

The Santos Bifurcation three-dimensional structure and dynamical consequences (23°S-30°S)

by

Tiago Carrilho Biló

A thesis submitted in partial fulfillment of the requirements for the degree of Master of Sciences in Oceanography, with emphasis in Physical Oceanography, *Instituto Oceanográfico, Universidade de São Paulo.*

Evaluated in _____ / _____ / _____

Prof. Dr.

Grade

Prof. Dr.

Grade

Prof. Dr.

Grade

“Olha ... eu não sei o que aconteceu, se aconteceu não to sabendo. Mas eu acho que o futebol não é isso o que aconteceu, porque eu não sei o que aconteceu. Mais o futebol foi o que aconteceu hoje, gols, jogadas bonitas e to feliz por isso ...”

João Paulo, jogador de futebol, 2015

“You see ... I don’t know what happened, if it happened I’m not aware of it. But I think that soccer isn’t what just happened, because I don’t know what happened. In addition, soccer was this what just happened today, goals, beautiful plays and I’m happy for it ...”

João Paulo, soccer player, 2015

Contents

	Page
List of Figures	v
List of Tables	vi
List of Acronyms	vii
Acknowledgements	ix
Abstract	x
Resumo	xi
<hr/>	
1 Introduction to the thesis	1
1.1 On the thesis structure	1
1.2 A regional overview of the large and meso scales circulation of the southwestern Atlantic	1
1.2.1 The South Atlantic Subtropical Gyre and the Brazil Current	1
1.2.2 The Brazil Current mesoscale activity between 23°S and 30°S	3
1.3 Thesis motivation, hypothesis and objectives	4
2 On the Brazil Current Meandering at 23°S-30°S	7
2.1 Introduction	8
2.2 Quasi-synoptic observations	9
2.2.1 The data set	9
2.2.2 The Brazil Current system	11
2.3 Linear instability analysis	25
2.3.1 The Model	25
2.3.2 The background states parameterization	28
2.3.3 Necessary conditions for instability and idealized experiments	37
2.3.4 Model Performance	39
2.3.5 Stability properties and energy pathway	40
2.4 Summary and conclusions	51

3 The Brazil Current cyclonic meandering at 27°S-31°S: water mass composition, vertical structure, surface signature and formation frequency	54
3.1 Introduction	55
3.2 The meanders vertical and horizontal structures	55
3.2.1 Velocity patterns and water masses	55
3.2.2 Evidences of shelf-slope mass exchanges and water trapping	60
3.3 The Brazil Current variability and cyclones recurrence	65
3.4 Summary and conclusions	66
4 Final remarks	69
<hr/>	
Appendix	71
A Model parameters and idealized experiments background states	71
B Perturbations and energy conversion terms from the idealized experiments	76
<hr/>	
Bibliography	87

List of Figures

1.1	Schematics of the surface circulation of the South Atlantic	2
1.2	Schematic representation of the Stommel's possible explanation for the differences in transport of the Gulf Stream and the BC	3
1.3	Schematic representation from <i>Soutelino et al. (2013)</i> of the western boundary currents off east/southeast Brazil as inferred from observations by <i>Stramma and England (1999)</i> and <i>Boebel et al. (1999)</i>	3
1.4	Advanced High Resolution Radiometer sea surface temperature (SST) image for July 20, 1993. Adapted from <i>Campos et al. (1996)</i>	5
2.1	Data set acquired during (a) the CERES IV cruise (June 2010) and (b) the CARBOM cruise (November 2013)	11
2.2	Velocity vectors obtained from VMADCP measurements at 100 m depth (red arrows) and LADCP observations at 800 m depth (blue arrows) taken during the (a) CERES IV (June 2010) and the (b) CARBOM (November 2013) cruises	12
2.3	Velocity vectors obtained from VMADCP measurements at 100 m depth (black arrows), taken during the CERES IV cruise, superimposed on the distribution of (a) salinity at 10 m (thermosalinograph), (b) temperature at 10 m (thermosalinograph) and (c) chlorophyll-a concentration at the surface (satellite image)	14
2.4	Temperature (°C) sectional distributions over the continental shelf and shelf break vicinities measured during the CERES IV cruise	15
2.5	The TS Diagram for the CERES IV (orange dots) and CARBOM (blue dots) cruises .	16
2.6	Cross-sectional velocity distribution at transect 24S from the CERES IV (upper panel) and the CARBOM cruises (lower panel)	18
2.7	Cross-sectional velocity distribution at transect 25S from the CERES IV (upper panel) and the CARBOM cruises (lower panel)	20
2.8	Velocity magnitude at transect 25S from the the CARBOM cruise	21
2.9	Cross-sectional velocity distribution at transect 26S from the CERES IV (upper panel) and the CARBOM cruises (lower panel)	22
2.10	Cross-sectional velocity distribution at transect 29S the CARBOM cruise	23
2.11	Cross-sectional velocity distribution at transect 30S the CARBOM cruise	24
2.12	Parameterization of the topographic profiles (solid line) at transects (a) 24S, (b) 26S and (c) 30S	31
2.13	The observed cross-sectional velocity distributions (upper panels) and the respective parametrized velocity field (lower panels) at transect (a) 24S, (b) 26S and (c) 30S . . .	33

2.14	Absolute velocity difference distributions between the observed and the parametric model at transect (a) 24S, (b) 26S and (c) 30S	34
2.15	Profiles of the BC horizontal ($\frac{\partial V}{\partial x}$, left panels) and vertical ($\frac{\partial V}{\partial z}$, right panels) velocity shears at transect (a) 24S, (b) 26S and (c) 30S	36
2.16	Profiles of the IWBC horizontal ($\frac{\partial V}{\partial x}$, left panels) and vertical ($\frac{\partial V}{\partial z}$, right panels) velocity shears at transect (a) 24S and (b) 26S	37
2.17	Product of the velocity V and the cross-sectional gradient of the basic potential vorticity ($\frac{\partial q}{\partial x}$) in the background state at transect (a) 24S, (b) 26S and (c) 30S.	38
2.18	(a) Growth rates and (b) phase speeds of the most unstable mode from the experiments 24S, 26S and 30S	42
2.19	Amplitudes of the perturbations fields ($\frac{\tilde{u}(x,\zeta)}{H_0}$, $\frac{\tilde{v}(x,\zeta)}{H_0}$ and $\frac{\tilde{b}(x,\zeta)}{H_0}$) and the energy conversion terms HHF, VHF and RS from experiment 24S.	44
2.20	Amplitudes of the perturbations fields ($\frac{\tilde{u}(x,\zeta)}{H_0}$, $\frac{\tilde{v}(x,\zeta)}{H_0}$ and $\frac{\tilde{b}(x,\zeta)}{H_0}$) and the energy conversion terms HHF, VHF and RS from experiment 26S.	45
2.21	Amplitudes of the perturbations fields ($\frac{\tilde{u}(x,\zeta)}{H_0}$, $\frac{\tilde{v}(x,\zeta)}{H_0}$ and $\frac{\tilde{b}(x,\zeta)}{H_0}$) and the energy conversion terms HHF, VHF and RS from experiment 30S.	46
2.22	Energy flux diagrams in 10^3 W m^{-1} (kW m^{-1}) from experiment (a) 24S, (b) 26S and (c) 30S. The red arrows with solid tail represent the baroclinic energy conversions terms and the blue arrows with solid tail the barotropic energy conversion terms. The arrows with dashed tail indicate how much energy are related with non-local instability processes.	47
2.23	(a) Growth rates and (b) phase speeds of the most unstable mode from the numerical experiments at transect 24S (upper panels), 26S (middle panels) and 30S (lower panels)	50
3.1	(a) The data set explored in this study. The circles (triangles) represent the locations of the CTD-LADCP stations of the CARBOM (MR03-K04 Leg 4) cruise and the diamonds the positions of the mooring lines. (b) CARBOM stations and its respective identification numbers. The large red numbers corresponds to the mean latitude of the each transect.	56
3.2	(a) Scattered TS Diagram overlaid on the <i>Mémery et al.</i> (2000) climatological water masses interfaces. Sectional velocity and water masses distributions observed during the (b) MR03 and (c) CARBOM cruises	59
3.3	The mapped stream function (Ψ) at (a) 30 m and (b) 700 m depth. The respective mapping errors are presented in panels (c) VMADCP and (d) LADCP	60
3.4	Horizontal salinity distributions at (a) 10 m, (b) 30 m and (c) 70 m depth. Panel (d) presents the temperature and salinity profiles from transect 29.02S where the STSW is present	62
3.5	Daily sea surface winds distributions for the period between 11/13/2013 and 11/21/2013	63
3.6	Distribution at 5 m depth of the concentration of (a) silicate, (b) phosphate, (c) nitrate, (d) ammonium and (e) chlorophyll-a	64
3.7	Same cyclonic meander event captured by the (a) daily SST and (b) 8-day composite sea surface chlorophyll-a satellite L4 images from MUR and MODIS respectively	65

3.8	Summary of the EOF analysis of the mooring lines array from the WOCE Experiment for the time period 01/05/1991 - 11/25/1992 (<i>Hogg et al., 1999</i>). (a) Mean cross-sectional velocity array; (b) the first statistical mode eigenstructure and energy spectrum; and (c) the second statistical mode eigenstructure and energy spectrum	67
A.1	The parametrized velocity field from the idealized experiment 24S _{nt}	71
A.2	The parametrized velocity field from the idealized experiment 24S _{bc}	72
A.3	The parametrized velocity field from the idealized experiment 26S _{nt}	73
A.4	The parametrized velocity field from the idealized experiment 26S _{bc}	74
A.5	The parametrized velocity field from the idealized experiment 30S _{nt}	74
A.6	The parametrized velocity field from the idealized experiment 30S _{bc}	75
B.1	Amplitudes of the perturbations fields ($\frac{\tilde{u}(x,\zeta)}{H_0}$, $\frac{\tilde{v}(x,\zeta)}{H_0}$ and $\frac{\tilde{b}(x,\zeta)}{H_0}$) and the energy conversion terms HHF, VHF and RS from experiment 24S _{nt}	77
B.2	Amplitudes of the perturbations fields ($\frac{\tilde{u}(x,\zeta)}{H_0}$, $\frac{\tilde{v}(x,\zeta)}{H_0}$ and $\frac{\tilde{b}(x,\zeta)}{H_0}$) and the energy conversion terms HHF, VHF and RS from experiment 24S _{bc}	78
B.3	Amplitudes of the perturbations fields ($\frac{\tilde{u}(x,\zeta)}{H_0}$, $\frac{\tilde{v}(x,\zeta)}{H_0}$ and $\frac{\tilde{b}(x,\zeta)}{H_0}$) and the energy conversion terms HHF, VHF and RS from experiment 26S _{nt}	79
B.4	Amplitudes of the perturbations fields ($\frac{\tilde{u}(x,\zeta)}{H_0}$, $\frac{\tilde{v}(x,\zeta)}{H_0}$ and $\frac{\tilde{b}(x,\zeta)}{H_0}$) and the energy conversion terms HHF, VHF and RS from experiment 26S _{bc}	80
B.5	Amplitudes of the perturbations fields ($\frac{\tilde{u}(x,\zeta)}{H_0}$, $\frac{\tilde{v}(x,\zeta)}{H_0}$ and $\frac{\tilde{b}(x,\zeta)}{H_0}$) and the energy conversion terms HHF, VHF and RS from experiment 30S _{nt}	81
B.6	Amplitudes of the perturbations fields ($\frac{\tilde{u}(x,\zeta)}{H_0}$, $\frac{\tilde{v}(x,\zeta)}{H_0}$ and $\frac{\tilde{b}(x,\zeta)}{H_0}$) and the energy conversion terms HHF, VHF and RS from experiment 30S _{bc}	82

List of Tables

2.1	Start and end dates of each quasi-synoptic transect from CERES and CARBOM experiments used in this work	10
2.2	Mean depths of water mass interfaces and their associated standard deviations calculated from the CERES IV and CARBOM set of 170 CTD profiles.	16
2.3	Primary characteristics of the BC cross-sectional velocity signal at each transect	25
2.4	Stability properties and energy conversion terms HHF, VHF, RS integrated over the transect area of the different numerical experiments	52
A.1	Scales of the background states used in the numerical experiments	71
A.2	Parameters of the background states used in the numerical experiments to the north of the Santos Bifurcation	72
A.3	Parameters of the background states used in the numerical experiments to the south of the Santos Bifurcation	73

List of Acronyms

SASG	South Atlantic Subtropical Gyre
AAIW	Antarctic Intermediate Water
BC	Brazil Current
SEC	South Equatorial Current
NBUC	North Brazil Under Current
NBC	North Brazil Current
DWBC	Deep Western Boundary Current
CTD	Conductivity, Temperature and Depth
IWBC	Intermediate Western Boundary Current
LADCP	lowered Acoustic Doppler Current Profiler
VMADCP	vessel-mounted Acoustic Doppler Current Profiler
CODAS	Common Ocean Data Access System
PE	primitive equations
QG	quasi-geostrophic
SACW	South Atlantic Central Water
UCDW	Upper Circumpolar Deep Water
NADW	North Atlantic Deep Water
TW	Tropical Water
MKE	mean kinetic energy
MPE	mean potential energy
EKE	eddy kinetic energy
EPE	eddy potential energy

RS	Reynolds stress
HHF	horizontal heat flux
VHF	vertical heat flux
RMS	root-mean-square
NOAA	National Oceanic and Atmospheric Administration
eT	e-folding time scale
MODIS	Moderate Resolution Imaging Spectroradiometer
MUR	Multi-scale Ultra-high Resolution
SST	sea surface temperature
WOCE	World Ocean Circulation Experiment
STSW	Subtropical Shelf Water
EOF	Empirical Orthogonal Functions

Acknowledgements

First of all, I deeply thank my friend and advisor Prof. Dr. Ilson C. A. da Silveira for his guidance. I owe him everything I am and conquered in my short carrier to his advising, patience and trust. Always thoughtful and concerned about my carrier, Ilson encouraged me all the time in the past seven years, providing great opportunities and exposing me to interesting problems. He also shared with me his passion for combining observations with theory, which definitely shaped my view about physical oceanography.

Secondly, I thank my parents Rosimeire and Claudio, and my brother Lucas. Their unconditional support always pushed me forward in the pursuit of professional and personal fulfilment. This work would not have been possible without them I and hope to let them proud.

My sincere thanks to Prof. Dr. Glenn R. Flierl. He opened the doors of one of the most renewed universities in the world for me. Dr. Flierl's precise suggestions and willingness to discuss and listen to my own findings and conclusions, made me more independent and rigorous scientist. Moreover, the contact with outstanding researchers and bright students at MIT and WHOI was highly stimulating.

I will not forget the period spent as a visiting student at MIT for reasons that transcend the academic achievements. I brought from Boston many great memories, real friends and a wonderful person who I expect to spend the rest of my life with (my little Asian/Brazilian girlfriend Rosangela Hoshi).

I would like to express all my gratitude for my great instructors/mentors in physical oceanography: Belmiro Castro, Edmo Campos, Paulo Polito, Olga Sato, Marcelo Dottori, Ilson Silveira, Sueli Godoi and Alberto Piola. I hope I demonstrated everything I have learned from you in this thesis.

Many thanks to all my past and present labmates. Special thanks to André Palóczy, César Rocha, Rafael Soutelino, Leandro Ponsoni, Leandro Calado, Patrícia Baldasso, Ana Paula Krelling, Ronaldo Sato, Iury Simões, and the MAUCARATIS (Pinguim, Gil, Yamashita and Pedro) for helping when I needed and making our lab (LaDO) a nice place to work in.

Finally I would like to thank my buddies Nancy Kazumi, Filipe Galiforni, Renato Oliveira, Natasha Hoff, Olavo Badaró, Rodrigo Carlini, Vinícius Bonadio, Caio Cerqueira, Thiago Zampa and José Maurício Ronaldo for all the good moments.

I acknowledge the Petróleo Brasileiro SA (PETROBRAS) for promoting the CERES experiment data set. A special thanks to my friend, and responsible for the CERES project, Dr. Wellington Ceccopieri Belo. He made possible the LaDO-PETROBRAS partnership and supported high-quality research. This work is part of the project *Rede de Estudos da Corrente do Brasil na Margem Continental Sudeste-Sul* (REMARSUL) funded by Coordination of Improvement of Personal Higher Education (CAPES). I also acknowledge Msc. Mayza Pompeu and professor Dr. Salvador Ayrton Gaeta for the nutrient analysis.

Financial support for this work was provided by São Research Foundation (FAPESP) under grants 2013/10475-6 (MSc scholarship) and 2014/00973-1 (BEPE).

Abstract

We use hydrographic and direct velocity observations from two quasi-synoptic cruises in conjunction with a primitive equation linear instability model, to investigate the Brazil Current (BC) downstream change effect between 23°S-30°S on the temporal mixed-instabilities properties. The quasi-synoptic data revealed that the BC is ~400-500 m deep to the north of the so-called Santos Bifurcation (26°S-28°S) and extends down to 1000 m to the south of it. We estimated that the BC receives at least 7 Sv from the Santos Bifurcation, which drastically alters the BC's velocity vertical structure and meanders characteristics as it flows poleward. Based on direct velocity measurements, we computed the mixed-instability properties at three different latitudes (24°S, 26°S and 30°S). The instability analysis revealed unstable current systems to mesoscale perturbations with maximum growth rates of 0.12, 0.19 and 0.06 day⁻¹ at 24°S, 26°S and 30°S respectively. The corresponding downstream phase speeds are -0.19, -0.24 and -0.26 m s⁻¹. The analysis of the mean-to-eddy energy conversion terms show that the barotropic instability drains 60-90% less energy from the background state than the baroclinic instability. Nevertheless, the maximum growth rates are at least the double in magnitude when both instabilities occur simultaneously. The topography presents a stabilizing effect for both kind of instabilities along all the BC path.

At the vicinities of the Cape Santa Marta (28°S), we explored the recurrent cyclonic meanders of the BC. Combining a wide range of observations, we provided a overview of such features and the relations between its velocity patterns, the water properties (temperature, salinity, nutrients), chlorophyll-a distribution and the BC variability. The top-bottom quasi-synoptic velocity measurements depicted cyclonic meanders over the continental slope with diameters larger than 100 km and vertically extending to approximately 1500 m depth. Moreover, the observed eddies seems to trap and recirculate a small portion (~1.5 to 4 Sv) of the BC main flow (-13.16 to -17.89 Sv), which is consisted of Tropical Water (TW), South Atlantic Central Water (SACW), Antarctic Intermediate Water (AAIW) and Upper Circumpolar Deep Water (UCDW). Additionally, we presented observational evidence that the meanders actively influence the transport of nutrient-rich shelf waters to the open ocean enhancing the primary productivity at the photic zone over the continental slope. Satellite imagery show that these cyclonic events occur 5-6 times per year and are generally associated with wave-like perturbations on the flow with mean wavelength of ~219 km. Finally, Empirical Orthogonal Functions (EOF) analysis computed from an array of mooring lines show that more than half of the along-isobath velocity variance on the continental slope is explained by the BC mesoscale activity.

Keywords: Brazil Current, Santos Bifurcation, mesoscale activity, baroclinic instability, barotropic instability.

Resumo

As propriedades de instabilidade temporal mista da Corrente do Brasil (CB), entre 23°S-30°S, foram investigadas combinando dados hidrográficos e medições diretas de velocidade com modelagem numérica. As observações revelaram uma CB com ~400-500 m de profundidade ao norte da Bifurcação de Santos (26°S-28°S). Em contrapartida, a CB ao sul da bifurcação se mostrou muito mais profunda (> 1000 m) devido ao aporte de aproximadamente 7 Sv de águas em profundidades intermediárias (~500-1500 m) oriundas do ramo sul da Bifurcação de Santos. Baseado-se nas observações, experimentos numéricos foram conduzidos em três latitudes (24°S, 26°S and 30°S), com o intuito de se estudar as propriedades da instabilidade geofísica da CB. Tais experimentos mostraram que o sistema de correntes é instável para perturbações de mesoescala com taxas de crescimento máximas de 0,12, 0,19 and 0,06 dia⁻¹ nas latitudes de 24°S, 26°S and 30°S, respectivamente. A análise das taxas de transferências de energia das correntes médias para as perturbações revelou que a instabilidade barotrópica é de 60 a 90% menor que a instabilidade baroclínica. No entanto observou-se que as propriedades das instabilidades da BC são altamente sensíveis à presença de instabilidade barotrópica. A topografia demonstrou possuir um efeito estabilizador ao longo de toda trajetória da CB.

Ao largo do Cabo de Santa Marta (28°S) os meandros ciclônicos da CB tiveram suas características exploradas do ponto de vista observacional. Combinando uma grande variedade de observações, foi obtido uma visão geral de tais feições, assim como as relações entre seus padrões de velocidade, propriedades da água do mar (temperatura, salinidade, nutrientes), distribuição de clorofila A e a variabilidade da BC. As observações quasi-sinóticas de velocidade em toda a coluna mostraram que os meandros possuem diâmetro superiores à 100 km e extensão vertical de aproximadamente 1500 m. Desta forma, observou-se feições que recirculam uma pequena parte (~1.5 à 4 Sv) do eixo principal da CB (-13.16 à -17.8 Sv) composta por Água Tropical, Água Central do Atlântico Sul, Água Intermediária Antártica e Água Circumpolar Superior. Além disso, evidências de que tais meandros influenciam ativamente no transporte de águas da Plataforma Continental, ricas em nutrientes, para regiões profundas do Talude Continental foram encontradas. A análise de imagens de satelitárias indicaram que essas feições são efetivamente recorrentes na região e ocorrem entre 5 a 6 vezes por ano. Para concluir, registros correntográficos indicaram que aproximadamente metade da variância da componente da velocidade ao logo das isóbatas, sobre o talude continental, é devido à atividade de mesoescala da CB.

Descritores: Corrente do Brasil, Bifurcação de Santos, fenômenos de mesescala, instabilidade baroclínica, instabilidade barotrópica.

Chapter 1

Introduction to the thesis

1.1 On the thesis structure

This thesis is written in a manuscript format and it comprises two self-contained chapters (Chapters 2 and 3). In both article-like chapters we study the Brazil Current (BC) meandering at 23°S-31°S from observations and numerical modelling. In this chapter, we provide an overview of the BC circulation pattern and mesoscale activity (Section 1.2) and the thesis motivation, hypothesis and objectives (Section 1.3). Chapter 4 summarizes our primary findings.

1.2 A regional overview of the large and meso scales circulation of the southwestern Atlantic

1.2.1 The South Atlantic Subtropical Gyre and the Brazil Current

The South Atlantic Subtropical Gyre (SASG) is the most prominent wind driven large scale circulation feature of the South Atlantic in the first ~1000 meters of water column. Due to the combination of the presence of continents, Earth's rotation and sphericity, it consists of an asymmetric anticyclonic gyre that is intensified at the western boundary of the oceanic basin *Talley et al.* (2011).

The BC is the western boundary current of the SASG (Figure 1.1). As it flows south/southwestward over the southeast Brazilian shelf break and continental slope between ~15°S-27°S, the BC presents an unique vertical velocity structure compared to other subtropical western boundary currents. Observations consistently depict the BC as a shallow and weak current compared to its counterparts in the Northern Hemisphere, the Gulf Stream and the Kuroshio (*Talley et al.*, 2011, e. g.). In this region, the BC transports Tropical Water (TW) near-surface and South Atlantic Central Water (SACW) at pycnocline depths. In contrast, at intermediate levels (~500-1800 m) there is a counterflow called the Intermediate Western Boundary Current (IWBC), flowing north/northeastward, transporting mainly Antarctic Intermediate Water (AAIW) (e. g., *Stramma and England*, 1999).

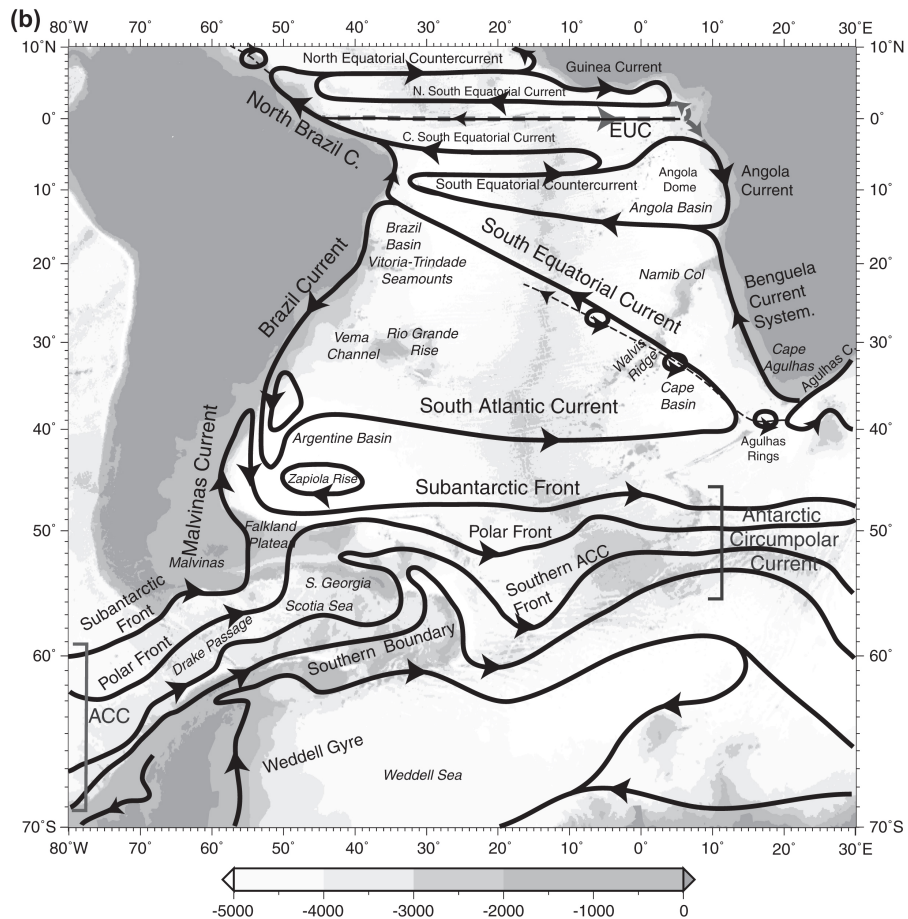


Figure 1.1: Schematics of the surface circulation of the South Atlantic. The black lines and arrow represent the main currents and their sense. The SASG ($\sim 10^{\circ}\text{S}$ - 40°S) is delimited by the South Equatorial Current (north), the BC (west) and South Atlantic Current (south). The light grey shades indicate the major topographic features. Source: [Talley et al. \(2011\)](http://booksite.academicpress.com/DPO) - <http://booksite.academicpress.com/DPO>

In a broad sense, the BC could be thought as the Sverdrup's return transport of the wind-driven large-scale circulation. However its singular velocity pattern may be explained in part by the interaction of the buoyancy-driven and wind-driven circulations as suggested by Henry Stommel in [Stommel \(1965\)](#). At that time, Henry Stommel proposed that the primary difference between the BC and the Gulf Stream's transport relies on the direction of the thermohaline circulation (now commonly referred as buoyancy-driven circulation) at intermediate depths in the South and North Atlantic (Figure 1.2).

Observations south of 28°S have shown that the entire water column over the shelf break and continental slope flows poleward transporting TW, SACW and AAIW (e. g., [Zemba, 1991](#); [Müller et al., 1998](#)). The transport differences between these two sectors of the BC is very variable since estimates of the BC volume transport reported in the literature varies from -5 to -16 Sv ($1 \text{ Sv} = 10^6 \text{ m}^3 \text{ s}^{-1}$) to the north of 25° ([Signorini, 1978](#); [Miranda and Filho, 1979](#); [Evans et al., 1983](#); [Stramma, 1989](#); [Garfield, 1990](#); [Campos et al., 1995](#); [Silveira et al., 2001](#); [Biló et al., 2014](#)) and from 10 to 27 Sv to the south of 28°S ([Garfield, 1990](#); [Zemba, 1991](#); [Rocha et al., 2014](#)).

The vertical structure change in these western boundary currents is linked to the complex depth-dependent bifurcation system of the South Equatorial Current (SEC) over the Brazilian continental margin (e. g., [Stramma and England, 1999](#); [Boebel et al., 1999](#); [Rodrigues et al., 2007](#)). The float observations from [Boebel et al. \(1999\)](#) and [Legeais et al. \(2013\)](#) indicate that at intermediate levels

the so-called Santos Bifurcation occur between 25°S and 27°S and incorporates the AAIW flow to the BC over the continental slope (blue arrows in Figure 1.3).

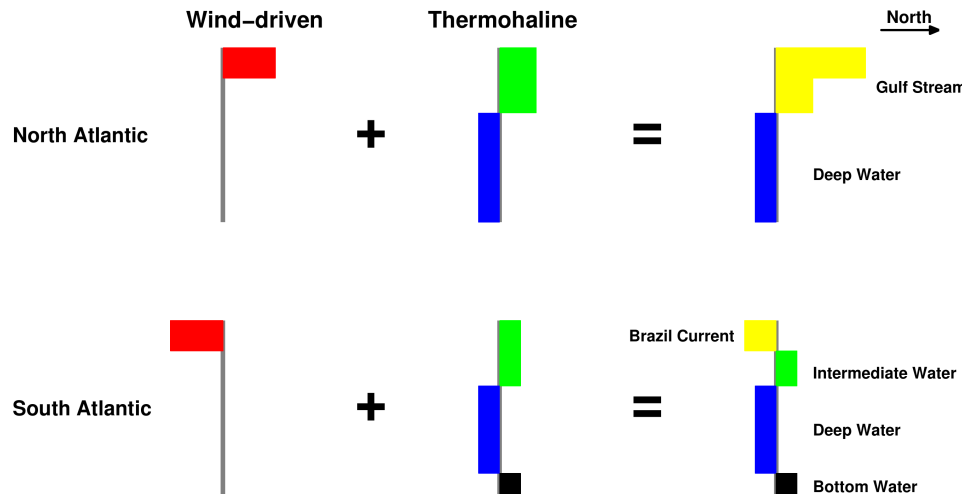


Figure 1.2: Schematic representation of the Stommel's possible explanation for the differences in transport of the Gulf Stream and the BC. Coloured rectangles represent water masses flows. Adapted from [Stommel \(1965\)](#). Courtesy: César B. Rocha.

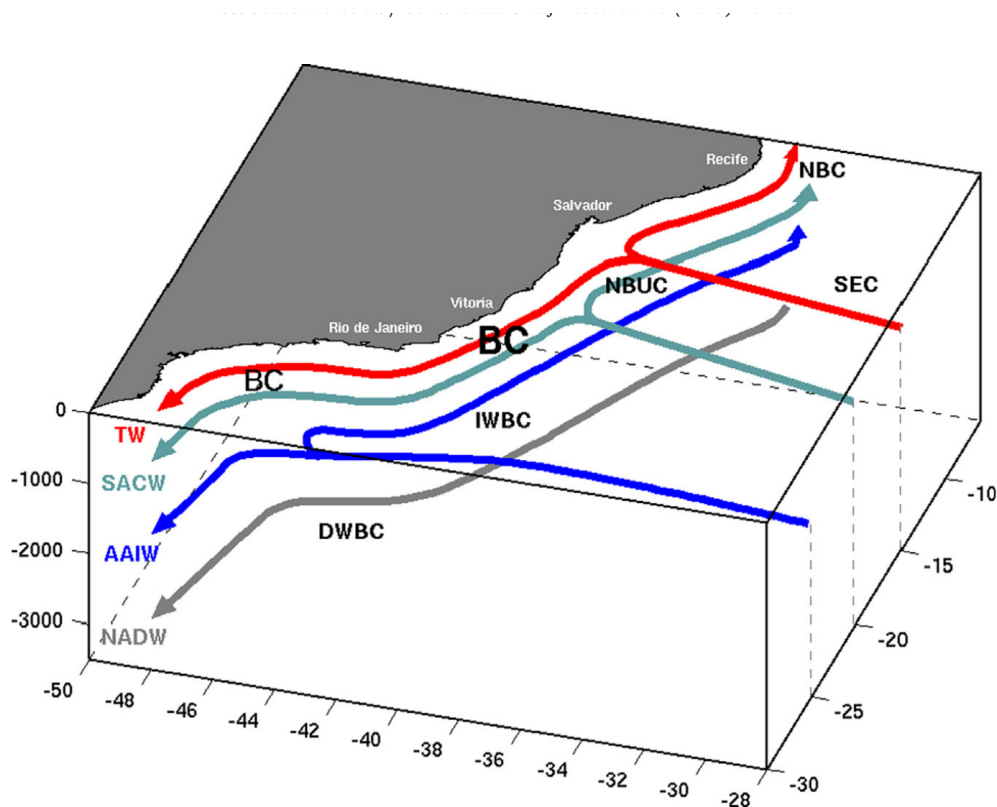


Figure 1.3: Schematic representation from [Soutelino et al. \(2013\)](#) of the western boundary currents off east/southeast Brazil as inferred from observations by [Stramma and England \(1999\)](#) and [Boebel et al. \(1999\)](#). Currents represented: Brazil Current (BC), Intermediate Western Boundary Current (IWBC), Deep Western Boundary Current (DWBC), North Brazil Under Current (NBUC) and North Brazil Current (NBC). Water masses depicted: Tropical Water (TW), South Atlantic Central Water (SACW), Antarctic Intermediate Water (AAIW) and North Atlantic Deep Water (NADW).

1.2.2 The Brazil Current mesoscale activity between 23°S and 30°S

Another interesting characteristic of the BC is its intense mesoscale activity. Meanders and eddies have been reported and studied by several authors from the BC genesis site ($\sim 15^{\circ}\text{S}$) to the Brazil-Malvinas confluence ($\sim 39^{\circ}\text{S}$) (*Signorini*, 1978; *Garfield*, 1990; *Campos et al.*, 1995; *Oliveira et al.*, 2009; *Soutelino et al.*, 2013), however few studies have addressed its dynamics. Between 22°S and 30°S the BC meanders are commonly reported as a sequence of cyclones and anticyclones as shown in Figure 1.4 (e. g., *Campos et al.*, 1995, 1996; *Silveira et al.*, 2008; *Lorenzetti et al.*, 2009).

Silveira et al. (2008) were the first to address the dynamics of the formation of such features. They showed that the mean BC at 22.7°S is baroclinically unstable. These authors were successful in predicting the length scales of the mesoscale variability in the region with an one-dimensional quasi-geostrophic (QG) stability model. The most-unstable waves produced by the model have growth rates about 0.06 (0.05) days^{-1} , wavelength about 266 (388) km and very small propagation speeds (quasi-stationary waves).

In order to elucidate the role of the BC-IWBC interaction in the development of meanders and eddies between 20°S - 28°S , *Fernandes et al.* (2009) implemented an idealized two-layer shallow water numerical model for the region. They approximated the horizontal velocity profiles of the currents system to opposing Gaussian jets over a realistic bathymetry. Their numerical experiment generated weakly unstable waves ($\sim 0.02 \text{ day}^{-1}$) of 430 km and phase propagation $\sim -0.2 \text{ m s}^{-1}$ (negative speeds indicate propagation poleward). These waves mostly grow in amplitude 20°S - 25°S , on the other hand to the south of 25°S the larger meanders gradually decrease their amplitudes. *Fernandes et al.* (2009)'s results seem to explain the southward eddy-motion description by *Garfield* (1990) from satellite imagery, however the differences with the *Silveira et al.* (2008)'s work at 22.7°S , suggest that other factors, as horizontal velocity structure (barotropic instability) and the rough topography, might have important impact in eddy formation.

More recently *Rocha et al.* (2014) carried out a similar stability analysis to *Silveira et al.* (2008) at 22.7°S , 25°S and 28°S in order to study the influence of the BC downstream changes in the baroclinic instability phenomena. The authors found that all the regions present a system baroclinically unstable with most-unstable waves of 230 km and growth rate of 0.035 day^{-1} at 22.7°S , 190 km and 0.056 day^{-1} at 25°S , and 180 km and 0.030 day^{-1} at 28°S . In agreement with *Silveira et al.* (2008), the unstable QG waves at 22.7°S have very small phase speeds (0.03 m s^{-1}). Conversely, the perturbations at 25°S and 28°S present significant phase propagation with -0.13 m s^{-1} and -0.15 m s^{-1} , respectively. These authors also found that the most unstable waves at 25°S and 28°S are slightly more efficient in extracting energy from the mean flow than at 22.7°S .

Based on a primitive equations (PE) numerical simulation, *Mano et al.* (2009) described energy fluxes during the a growing cyclonic meander at 22°S . Although the basic phenomenology is qualitatively consistent with the baroclinic instability arguments from *Silveira et al.* (2008), the meandering seems to be much more complicated. The *Oliveira et al.* (2009)'s study of surface energetics from drifting buoys shows that the eddy kinetic energy is relevant along all the BC path and part of its variability may be accounted for by barotropic instabilities.

Additionally, in the Santos Basin (23°S - 28°S) dipoles are recurrently observed in SST distributions (e. g., Figure 1.4). *Miranda* (2013) built a QG semi-analytical model to study the dynamics of the BC

dipoles. The author demonstrates how the barotropic instabilities and topography are able to generate propagating dipoles in the region.

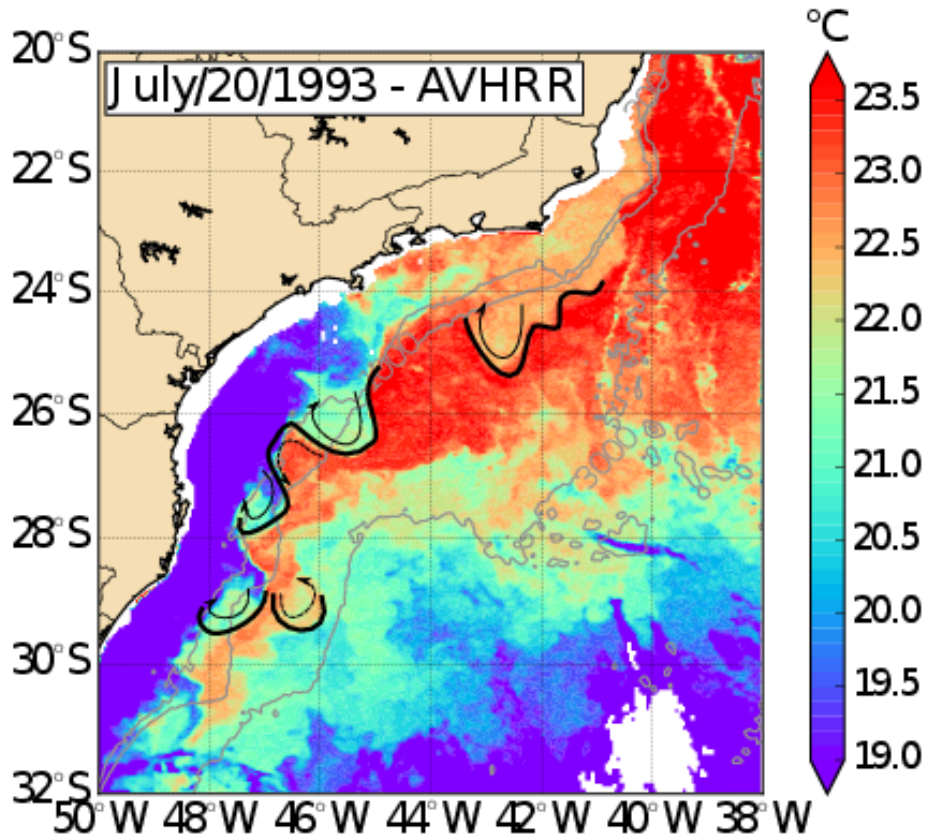


Figure 1.4: Advanced High Resolution Radiometer sea surface temperature (SST) image for July 20, 1993. The BC mesoscale activity is represented by a sequence of crests (warm) and troughs (cold). The arrows highlight the cyclonic (solid) and anticyclonic (dashed) meanders. Adapted from [Campos et al. \(1996\)](#).

1.3 Thesis motivation, hypothesis and objectives

Even today most of the available information about the velocity structure and volume transport of the BC is based on geostrophic calculations. Direct velocity observations are still rare and sparse in space and time (e. g., [Rocha et al., 2014](#); [Biló et al., 2014](#)). Moreover studies that addressed the BC downstream changes from velocity observations, or based their analysis on currentmeters records sparsely placed at different locations of the BC path ([Müller et al., 1998](#); [Rocha et al., 2014](#)), or are limited to a fix depth ([Boebel et al., 1999](#); [Oliveira et al., 2009](#); [Legeais et al., 2013](#)).

In a such changing system the characteristics of its stability properties also changes. Different studies carried out barotropic and baroclinic stability analysis between 23°S and 31°S, however none have explored the consequences of those processes occurring simultaneously (**the mixed-instability problem**) and the effects of the continental slope topography in this region. Moreover, the estimates

of growth rates and phase speeds of unstable waves rely on the quasi-geostrophic (QG) approximation. No instability computations employed primitive equations (PE) so far.

In that sense, there is a lack of important information concerning the BC horizontal and vertical downstream changes at 23°S-31°S and the dynamics of the BC meandering growth and propagation. Motivated by these open questions, we formulated the hypotheses bellow:

Hypothesis 1 *Although the downstream changes on the BC meander characteristics and growth are mainly due to the BC thickening and baroclinic instability, the barotropic instability and topography have a significant impact on the linear instability properties along the BC path;*

Hypothesis 2 *The BC meandering off Cape Santa Marta ($\sim 28^{\circ}\text{S}$) is as frequent as the meanders described north of the Santos Bifurcation (25°S-27°S), and presents a vertical extension of more than 1000 m transporting TW, SACW, AAIW and UCDW.*

In particular the Chapter 2's specific objectives are to draw a three-dimensional picture of the circulation over the southeast Brazilian shelf break and continental slope and to investigate the mixed-instability properties of the BC (23°S-30°S), by answering the following scientific questions:

1. What are the differences between the instabilities to the north and to the south of the Santos Bifurcation?
2. What are the instability driving-mechanisms?
3. What are the effects of topography?

The Chapter 3's main objective is to describe the characteristics of the BC variability and cyclonic meanders near Cape Santa Marta (28°S).

Chapter 2

On the Brazil Current Meandering at 23°S-30°S

Abstract

We use hydrographic and direct velocity observations from two quasi-synoptic cruises in conjunction with a primitive equation linear instability model, to investigate the Brazil Current (BC) downstream change effect between 23°S-30°S on the temporal mixed-instabilities properties. The quasi-synoptic data revealed that the BC is ~400-500 m deep to the north of the so-called Santos Bifurcation (26°S-28°S) and extends down to 1000 m to the south of it. We estimated that the BC receives at least 7 Sv from the Santos Bifurcation, which drastically alters the BC's velocity vertical structure and meanders characteristics as it flows poleward. Based on direct velocity measurements, we computed the mixed-instability properties at three different latitudes (24°S, 26°S and 30°S). The instability analysis revealed unstable current systems to mesoscale perturbations with maximum growth rates of 0.12, 0.19 and 0.06 day⁻¹ at 24°S, 26°S and 30°S respectively. The corresponding downstream phase speeds are -0.19, -0.24 and -0.26 m s⁻¹. The analysis of the mean-to-eddy energy conversion terms show that the barotropic instability drains 60-90% less energy from the background state than the baroclinic instability. Nevertheless, the maximum growth rates are at least the double in magnitude when both instabilities occur simultaneously. The topography presents a stabilizing effect for both kind of instabilities along all the BC path.

Keywords: Brazil Current, Santos Bifurcation, mesoscale activity, baroclinic instability, barotropic instability.

2.1 Introduction

The Brazil Current (BC) is likely the most peculiar and least studied of the world's major western boundary currents. Observations between 20°S and 25°S consistently depict the BC as a shallow and weak current compared to its counterparts in the Northern Hemisphere, the Gulf Stream and the Kuroshio current, as it flows poleward over the southeast Brazilian shelf break and continental slope (e. g., [Talley et al., 2011](#)). In this region, the BC transports Tropical Water (TW) near-surface (< 200 m) and South Atlantic Central Water (SACW) at pycnocline depths ([Campos et al., 1995](#)). At intermediate levels (~500-1800 m), there is a counterflow called Intermediate Western Boundary Current (IWBC), flowing equatorward, transporting mainly Antarctic Intermediate Water (AAIW) and Upper Circumpolar Deep Water (UCDW) (e. g., [Silveira et al., 2004](#)). In a broad sense, the BC could be thought as the Sverdrup's return transport of the wind-driven large-scale circulation of the South Atlantic, however its singular velocity vertical structure may be explained in part by the interaction of the buoyancy-driven and wind-driven circulations, as suggested by [Stommel \(1965\)](#).

Observations south of 28°S have shown that the entire water column over the shelf break and continental slope flows poleward transporting TW, SACW, AAIW and UCDW (e. g., [Zemba, 1991](#); [Müller et al., 1998](#)). This interesting feature is linked to the complex depth-dependent bifurcation system over the Brazilian continental margin that feeds and thickens the BC along its poleward path (e. g., [Stramma and England, 1999](#); [Boebel et al., 1999](#); [Rodrigues et al., 2007](#)). The analysis of trajectories of Lagrangian floats performed by [Boebel et al. \(1999\)](#) and [Legeais et al. \(2013\)](#) showed that at intermediate levels (800-1200 m) the so-called Santos Bifurcation occur between 25°S and 27°S.

Unfortunately, most of our understanding about the BC-IWBC system relies on quasi-synoptic hydrographic observations, which constrained the development of quantitative descriptions of these currents and its downstream changes ([Signorini, 1978](#); [Miranda and Filho, 1979](#); [Evans et al., 1983](#); [Stramma, 1989](#); [Garfield, 1990](#); [Campos et al., 1995](#); [Lima, 1997](#); [Silveira et al., 2001](#)). Between 23°S and 30°S, only four studies provide quantitative descriptions of the BC-IWBC system based on direct velocity measurements: ([Evans and Signorini, 1985](#)); ([Müller et al., 1998](#)); ([Rocha et al., 2014](#)); ([Biló et al., 2014](#)). [Evans and Signorini \(1985\)](#) presented a series of cross-isobath velocity profiles at approximately 23°S, which revealed that the BC extends to depths of 400-500 m and a counterflow is present underneath, reaching depths about 1000 m. [Müller et al. \(1998\)](#) and [Rocha et al. \(2014\)](#) addressed the BC vertical thickening by comparing records from currentmeter mooring lines at different latitudes. Finally, [Biló et al. \(2014\)](#) presented a quasi-synoptic velocity transect measured by lowered Acoustic Doppler Current Profiler (LADCP), providing by the first time estimates of BC-IWBC system volume transport from direct velocity measurements at ~26°S.

Another interesting characteristic of the BC is its intense mesoscale activity. Meanders and eddies were reported and studied by several authors (e. g., [Signorini, 1978](#); [Garfield, 1990](#); [Campos et al., 1995, 1996](#); [Silveira et al., 2008](#); [Mano et al., 2009](#); [Rocha et al., 2014](#)); however few studies have addressed its dynamics. [Silveira et al. \(2008\)](#) showed that the BC-IWBC system at 22.7°S is baroclinically unstable. These authors were successful in predicting the length scales of the mesoscale variability in the region with an one-dimensional quasi-geostrophic (QG) stability model. The most-unstable waves produced by the model have growth rates about 0.06 (0.05) days⁻¹, wavelength about 266 (388) km

and very small propagation speeds (quasi-stationary waves).

In order to elucidate the role of the BC-IWBC interaction in the development of meanders and eddies between 20°S-28°S, *Fernandes et al.* (2009) implemented an idealized two-layer shallow water equations numerical model for the region. They approximated the horizontal velocity profiles of the BC System to opposing Gaussian jets over a realistic bathymetry. Their numerical experiment generated weakly unstable waves (~ 0.02 day $^{-1}$) of 430 km and phase propagation ~ -0.2 m s $^{-1}$ (negative speeds indicate propagation poleward). These waves mostly grow in amplitude 20°S-25°S, on the other hand to the south of 25°S the larger meanders gradually decrease their amplitudes. *Fernandes et al.* (2009)'s results seem to explain the southward eddy-motion described by *Garfield* (1990) from satellite imagery, however the differences with the *Silveira et al.* (2008)'s work at 22.7°S, suggest that other factors, as horizontal velocity structure (barotropic instability) and the rough topography, might have important impact in the initial stages of eddy formation.

Recently, *Rocha et al.* (2014) carried out a similar stability analysis to *Silveira et al.* (2008) at 22.7°S, 25°S and 28°S in order to study the influence of the downstream changes in the baroclinic instability phenomena. The authors found that all the regions present a BC system¹ baroclinically unstable with most-unstable waves of 230 km and growth rate of 0.035 day $^{-1}$ at 22.7°S, 190 km and 0.056 day $^{-1}$ at 25°S, and 180 km and 0.030 day $^{-1}$ at 28°S. In agreement with *Silveira et al.* (2008), the unstable QG waves at 22.7°S have very small phase speeds (0.03 m s $^{-1}$). Conversely, the perturbations at 25°S and 28°S present phase propagation with -0.13 m s $^{-1}$ and -0.15 m s $^{-1}$, respectively. These authors also found that the most unstable waves at 25°S and 28°S are slightly more efficient in extracting energy from the mean flow than at 22.7°S.

Based on a primitive equations (PE) numerical simulation, *Mano et al.* (2009) described energy fluxes during the growing of a cyclonic meander at 22°S. Although the basic phenomenology is qualitatively consistent with the baroclinic instability arguments from *Silveira et al.* (2008), the meandering seems to be much more complicated. The *Oliveira et al.* (2009)'s study of surface energetics from drifting buoys shows that the eddy kinetic energy is relevant along all the BC path and part of its variability may be accounted for by barotropic instability. Additionally, in the Santos Basin (23°S-28°S) dipoles are recurrently observed in the sea surface temperature images. *Miranda* (2013) built a QG semi-analytical model to study the dynamics of the BC dipoles. The author demonstrates how the barotropic instabilities and topography are able to generate propagating dipoles in the region.

In summary, different studies carried out barotropic and baroclinic stability analysis between 23°S and 30°S, however none have explored the consequences of those processes occurring simultaneously (**the mixed-instability problem**) and the effects of the continental slope rough topography in this region. In that sense, there is a lack of important information concerning the dynamics of the BC meandering growth and propagation.

Here, we draw a three-dimensional picture of the circulation over the southeast Brazilian shelf break and continental slope and investigated the mixed-instability properties of the BC (23°S-30°S). Our guiding questions are: (1) What are the differences between the instabilities to the north and to the south of the Santos Bifurcation? (2) What are the instability driving mechanisms? (3) What are the effects of topography? To address these questions we analyse two quasi-synoptic data sets in

¹From now on the BC and the IWBC underneath it will be referred as BC system for simplicity. This term was proposed in Portuguese by *Godoi* (2005) and introduced in the English language by *Rocha et al.* (2014).

conjunction with a PE linear instability model.

2.2 Quasi-synoptic observations

2.2.1 The data set

We mainly explored two quasi-synoptic data sets in this work, in order to accomplish our objectives and answer the guiding questions. The first data set is the forth leg of the CERES experiment which consisted of five quasi-synoptic hydrographic surveys to investigate the BC and its recirculation cells within the Santos Basin (e. g., *Biló et al.*, 2014). This cruise was carried out in June 2010 and consists of a set of stations where top-bottom hydrographic and velocity profiling were taken with Conductivity, Temperature and Depth (CTD) and LADCP, respectively. Underway, 75 kHz vessel-mounted Acoustic Doppler Current Profiler (VMADCP) observations from surface to approximately 400 m and shipboard thermosalinograph measurements at ~10 m depth were also obtained. These measurements are disposed in four transects, as shown by Table 2.1 and panel **a** of Figure 2.1².

The second data set was acquired in November of 2013 and it is part of the INCT-CARBOM experiment, which aims to study carbon fluxes in the Brazilian continental margin. The CARBOM cruise consists of seven quasi-synoptic transects where CTD, LADCP and VMADCP measurements were conducted. It's important to mention that the four transects further north in our study region are repetitions of the correspondent transects in the CERES IV cruise (24S, 24.5S, 25S and 26S from Figure 2.1), so it can also be referred as the fifth survey of the CERES Experiment.

Table 2.1: Start and end dates of each quasi-synoptic transect from CERES and CARBOM experiments used in this study.

Transect ID	Start date	End date
CERES IV		
24S	08-Jun.-2010	11-Jun.-2010
24.5S	11-Jun.-2010	14-Jun.-2010
25S	14-Jun.-2010	18-Jun.-2010
26S	18-Jun.-2010	21-Jun.-2010
CARBOM		
24S	01-Nov.-2013	03-Nov.-2013
24.5S	04-Nov.-2013	06-Nov.-2013
25S	08-Nov.-2013	10-Nov.-2013
26S	12-Nov.-2013	14-Nov.-2013
28S	18-Nov.-2013	19-Nov.-2013
29S	20-Nov.-2013	21-Nov.-2013
30S	22-Nov.-2013	23-Nov.-2013

²The transects identification names were given based on its respective mean latitudes

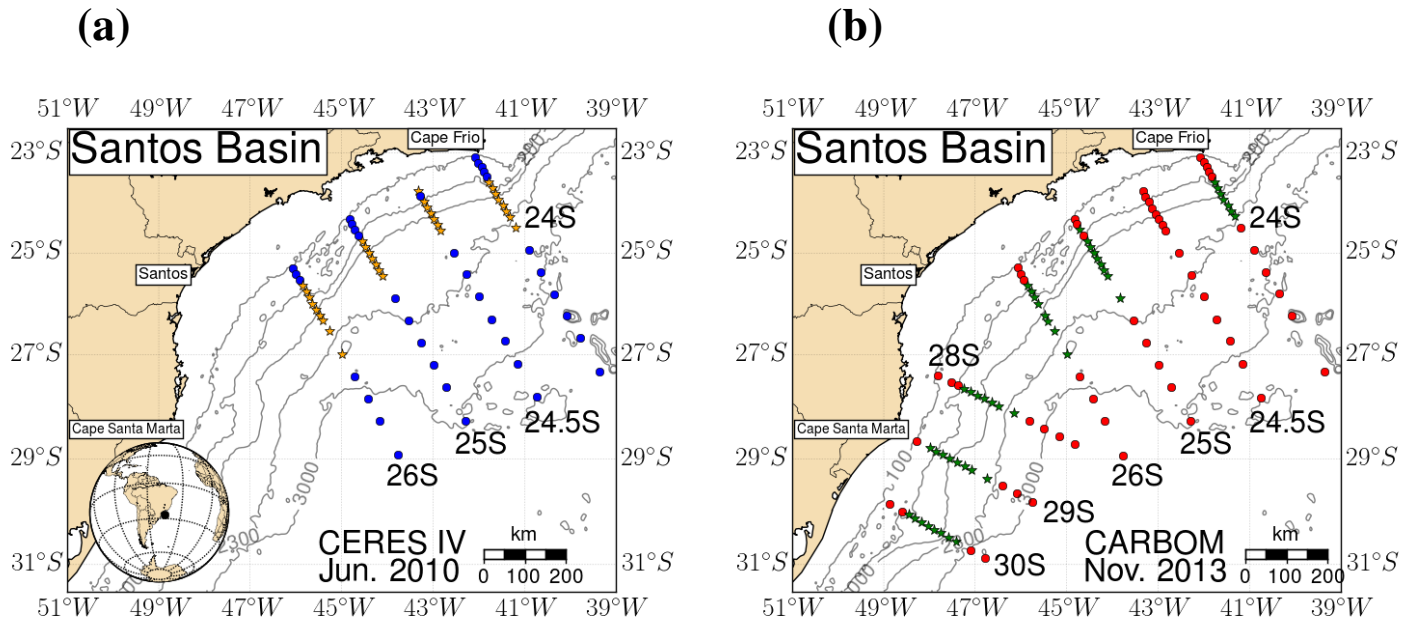


Figure 2.1: Data set acquired during (a) the CERES IV cruise (June 2010) and (b) the CARBOM cruise (November 2013). The circles represent the locations where only CTD profiles are available and the stars indicate the stations where LADCP and CTD data were acquired simultaneously. The black numbers are the corresponding transects identification.

During the surveys, velocity profiles were obtained using the same downward-looking 300 kHz LADCP Workhorse Sentinel from RD Instruments. The average velocity profile at each station was calculated following the procedures described by [Fischer and Visbeck \(1993\)](#) and [Visbeck \(2002\)](#). The ocean velocities in the first 400 m, which were measured simultaneously by a 75 KHz VMADCP Ocean Surveyor (also from RD Instruments), were included in the LADCP data processing to additionally constrain the solution of the inverse problem. This methodology reduces errors because the constraints from bottom tracking and the upper ocean velocities force the average velocity profile to agree with these more accurate data (e.g., [Visbeck, 2002](#); [Schott et al., 2005](#)). In general, the estimated accuracy of the LADCP varied from 3 cm s^{-1} in the constrained domain to 5 cm s^{-1} in the middle of the water column ($400 \text{ m} \leq \text{depth} \leq \text{bottom}-100 \text{ m}$). The VMADCP data processing was conducted using the processing software Common Ocean Data Access System (CODAS) from the Currents Group of the University of Hawaii.

In this section we focus on the description of the velocity sectional distribution measured with the LADCP (stars presented in Figure 2.1), giving emphasis on the BC and IWBC. The other observations are used as auxiliary information to help us interpret the measured velocity signals. Moreover, these data consist of an important framework for the instability study in Section 2.3.

2.2.2 The Brazil Current system

Overall horizontal patterns

A general picture of the BC system captured by our observations set is shown in Figure 2.2. These maps of vectors represent the velocity horizontal distributions in the BC (100 m) and in the IWBC (800 m) domain. The 100 m and 800 m depths were carefully chosen, because they present a clear signal of

the currents system and are close to BC and IWBC respective maximum velocities area (e. g., *Legeais et al.*, 2013; *Biló et al.*, 2014). Please note that the vectors from different cruises are not in the same scale for better visualization.

Between 23°S and 31°S, the shelf break position location is approximately represented by the 200 m isobath. Moreover, the location of the continental slope bottom varies from ~2000 m in the Santos Plateau area (23°S-28°S) to approximately 2700 m depth to the south of 28.5°S (*Castro and de Miranda*, 1998). In that sense, we should expect to find the BC system velocity signal between the 200 m and 2300 m isobaths in the Figure 2.2.

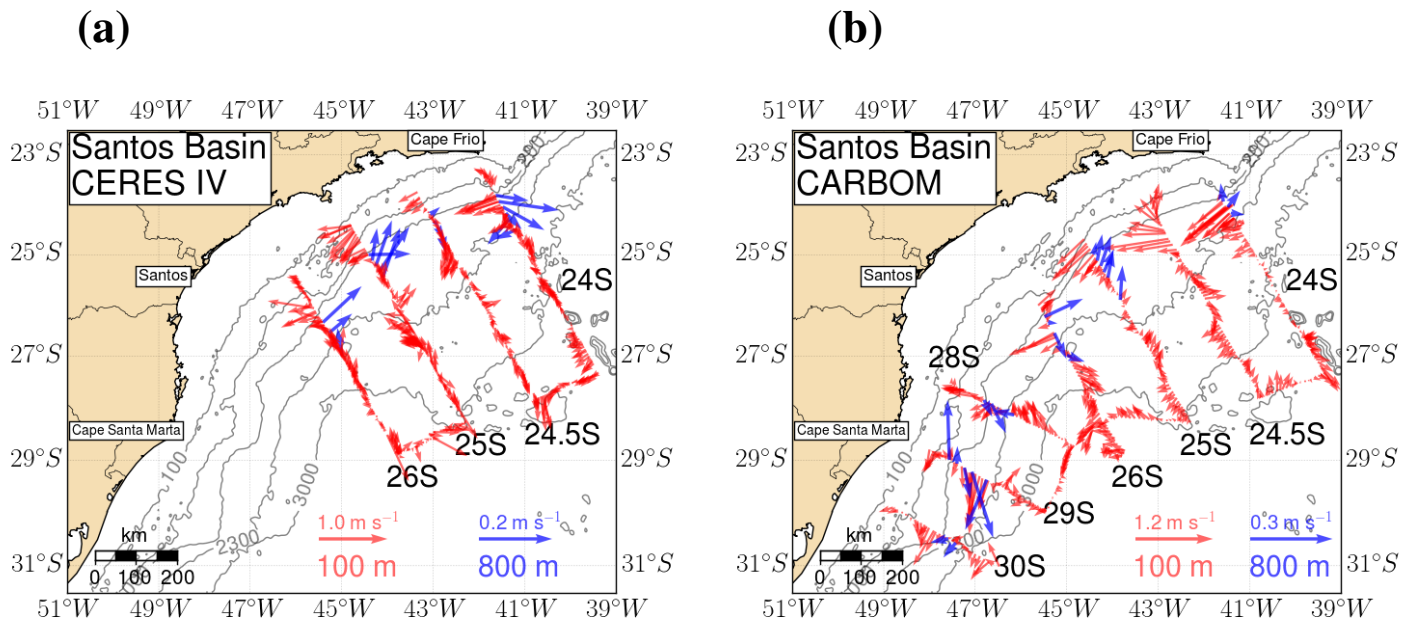


Figure 2.2: Velocity vectors obtained from VMADCP measurements at 100 m depth (red arrows) and LADCP observations at 800 m depth (blue arrows) taken during the (a) CERES IV (June 2010) and the (b) CARBOM (November 2013) cruises. The contoured isobaths (gray lines) are 100, 200, 1000, 2300 and 3000 m.

During the the CERES IV cruise (panel **a**, Figure 2.2) we observe a very interesting scenario concerning the BC system. At transect 24S, the parabolic-shaped BC is well defined by the largest southwestward vectors over the continental slope. Further south, the BC seems to anticyclonically meander as it crosses the transects 24.5S and 25S, where no clear velocity signal of the boundary current is observed over the slope. In fact, at 24.5S the largest vectors are close to the 2300 m isobath and over the outer shelf, which differs entirely to the velocity signal at transect 25S, where the fastest velocities are placed over the shelf-break and outer shelf. At transect 26S it is possible to distinguish the BC signal again between the 200 m and 1000 m isobaths.

At 800 m depth, the IWBC signal is distinguishable flowing northeastward in the study region. Note that, at transect 24.5S, the velocities are considerable smaller and the vector closer to the 1000 m isobath is the only one with a northward velocity component, which suggests that part of the IWBC is crossing the 24.5S transect and part might be recirculating. The float trajectories presented by *Legeais et al.* (2013) show that such activity exists indicating the presence of meanders and water recirculation.

During the CARBOM cruise (panel **b**, Figure 2.2) the BC system path is clear at all transects over

the continental slope. Moreover the CARBOM larger spacial coverage allows us to identify the Santos Bifurcation area between transects 26S and 28S due to the divergence of the vectors at 800 m depth. Note that at transects 26S and 29S cyclonic eddy-like structures are present due to the change from equatorward flow to poleward flow as we move away from the coast.

Its is important to stress out that we did not provided an explanation concerning the BC path and its possible meandering activity at transects 24.5S and 25S from CERES IV cruise, until now. So, before moving forward with the description of the velocity sectional distributions we should shed light on the matter. Its well known that the BC flows carrying oligotrophic, warm and salty TW ($T > 20^\circ\text{C}$, $S > 36$) in the upper mixed-layer and the cooler SACW at pycnocline depths ($10^\circ\text{C} < T < 18^\circ\text{C}$, $35 < S < 36$) (*Emilson, 1961; Stramma and England, 1999*). In the mixed-layer, the TW is in contact with cooler and fresher coastal waters creating a thermal and haline contrast between the water masses, moreover shelf waters tend to be more biological productive than the oceanic ones due to a variety of reasons (*Talley et al., 2011*). In that sense, the zoomed-in region displayed in Figure 2.3 might give us a good idea of what is happening in the mixed-layer regarding the BC meandering.

Using the salinity and temperature measured by the thermosalinograph along the ship route, we were able to obtain the distributions of these properties at approximately 10 m depth (Figure 2.3 panels **a** and **b**, respectively). We also looked at the chlorophyll-a concentration at the surface from the Moderate Resolution Imaging Spectroradiometer (MODIS) sensor aboard of the Aqua satellite (Figure 2.3 panel **c**). We opted to use a cloud free image by accessing the 8-day composite product available in the NASA's OceanColor Web (<http://oceancolor.gsfc.nasa.gov/>) from the cruise time period.

The analysis of the salinity, temperature and chlorophyll-a distributions between transects 25S and 26S indicates that the BC is meandering over the outer-shelf at transect 25S. The anticyclonic meander signature can be found in Figure 2.3 by following the offshore displacement from the 100 m isobath to the vicinities of the shelf break (200 m isobath) of the maximum velocity vectors, isotherm of 22.5°C , isohalines of 36.0 and 35.5, and chlorophyll-a concentration front as the BC flows southward. If we apply the same reasoning for transects 24S and 24.5S, or 24.5S and 25S we are lead to conclude that the BC crosses the transects 24.5S and 25S over the outer-shelf forming a large anticyclonic meander. Note that the chlorophyll-a distribution has a local maximum of concentration that resembles a cyclonic eddy signature at transect 24.5S. Since it does not have a clear signal in the temperature and salinity fields, we interpreted this feature as an eddy that pinched off from the BC and is interacting with the meandering current.

Additional indication of the existence of this large anticyclonic meander is given by Figure 2.4. One of the primary mechanisms that regulates the penetration of the SACW in the continental shelf between 24°S and 25°S is the BC meandering (e. g., *Matano et al., 2010; Cerdá and Castro, 2014*). In that sense, we studied the temperature fields using CTD stations over the continental shelf and shelf-break at each transect (Figure 2.4). The penetration of the SACW is shown by the 18°C and 15°C lines. Since the transect 24S is too close to Cape Frio, it is expected to observe temperatures lower than 20°C reaching regions close to the sea surface near the 100 m isobath due to the frequent wind forced upwelling system (e. g., *Signorini, 1978; Castro and de Miranda, 1998*). Therefore, comparing the temperature section at transect 26S to the fields at 24.5S and 25S, the 15°C isotherm reaches shallower regions under the meandering scenario.

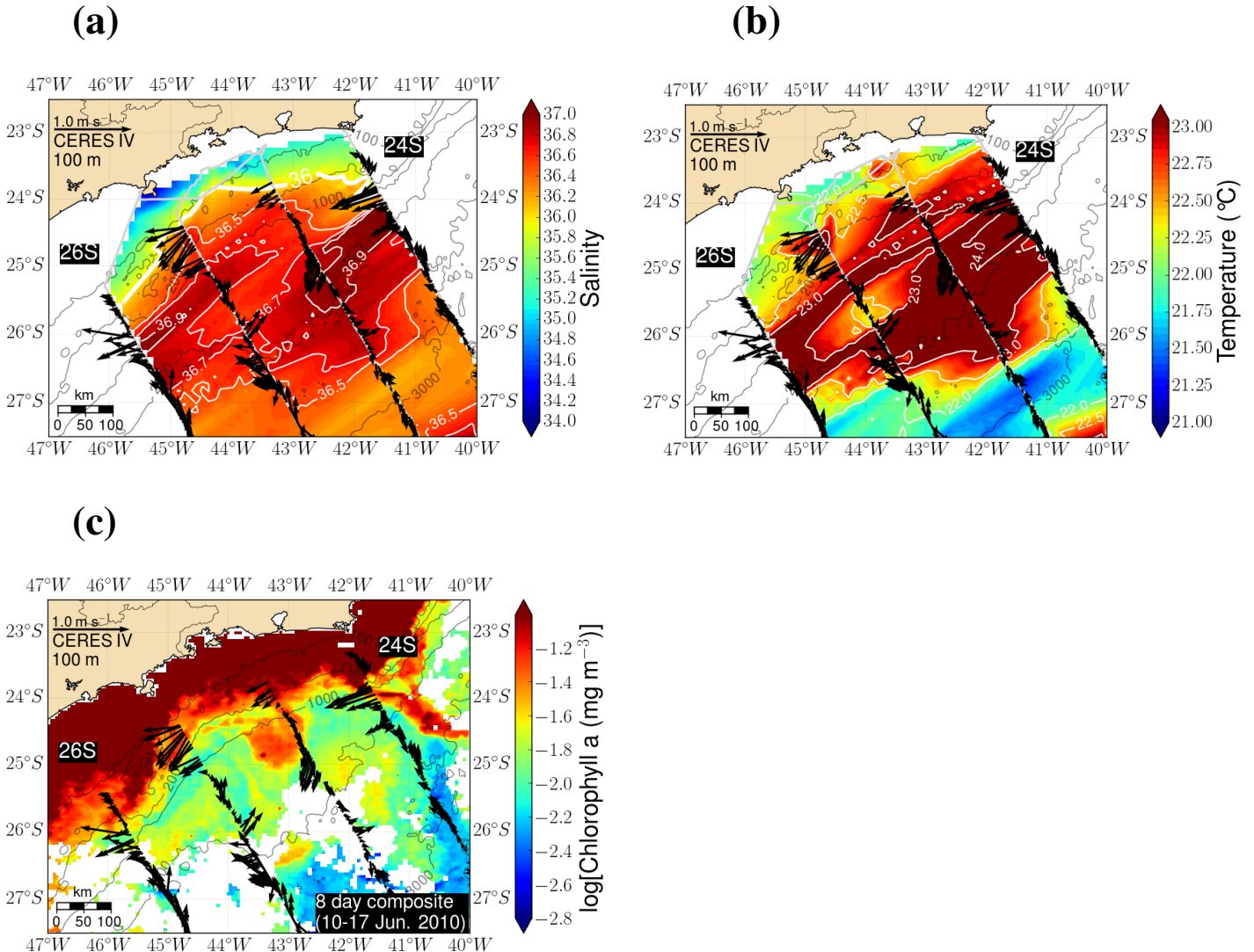


Figure 2.3: Velocity vectors obtained from VMADCP measurements at 100 m depth (black arrows), taken during the CÉRES IV cruise, superimposed on the distribution of (a) salinity at 10 m (thermosalinograph), (b) temperature at 10 m (thermosalinograph) and (c) chlorophyll-a concentration at the surface (satellite image). The contoured isobaths (gray lines) are 100, 200, 1000, 2300 and 3000 m.

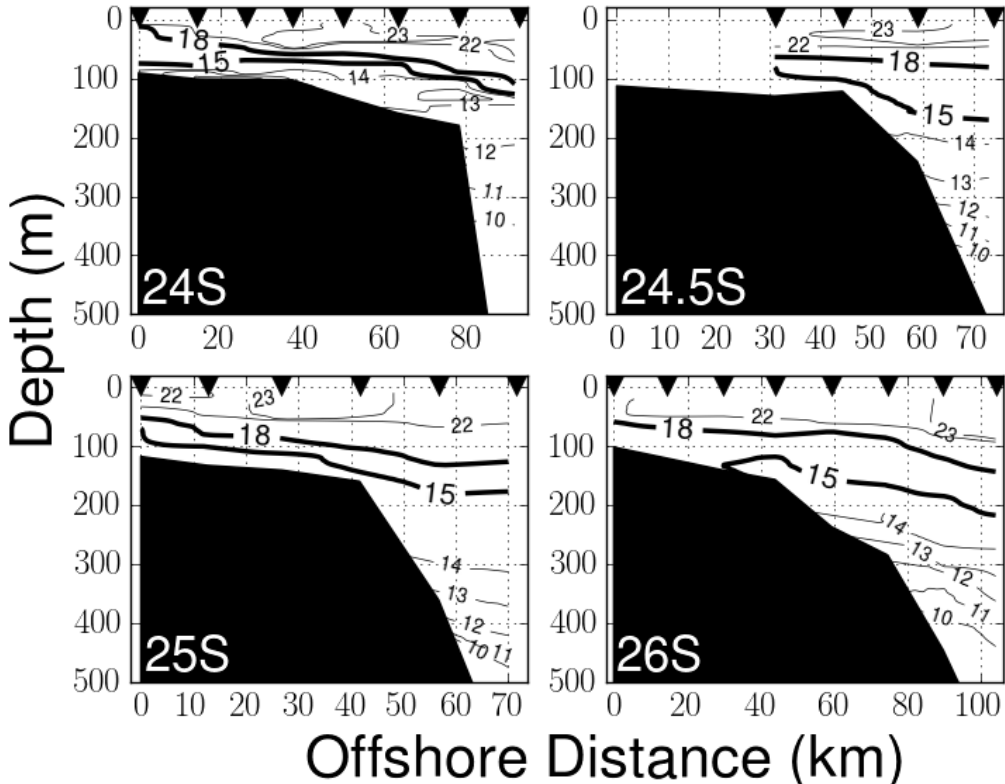


Figure 2.4: Temperature ($^{\circ}\text{C}$) sectional distributions over the continental shelf and shelf break vicinities measured during the CERES IV cruise. The black triangles represent the locations of the CTD stations.

Velocity transects and the BC downstream changes

Once identified the location of the BC system through the study area, we were able to better interpret its top-bottom velocity distribution and how it changes as the BC flows poleward. In that sense, we described the cross-sectional velocity component of each transect obtained from a composition of the LADCP and VMADCP data. Such composites were created for two reasons: to improve the horizontal resolution in the upper 300-400 m between the LADCP profiles; and complement the observations over the continental shelf if necessary. Similar procedures were carried out by other authors (e. g., *Schott et al.*, 2005) and are essential to better identify different features in the velocity distribution. It is important to mention that we do not present the composites for transects 24.5S and 28S due to the lack of LADCP profiles or no robust cross-sectional velocity component. In Figures 2.1 and 2.2 we can observe that the first condition is true for the CARBOM 24.5S transect and the second is true for the CERES IV 24.5S and CARBOM 28S transects.

We also associated the western boundary circulation with the vertical disposal of the water masses along the transects. The TS Diagram overlaid on the *Mémetry et al.* (2000) climatological water mass interfaces (Figure 2.5) show the presence of the water masses TW near surface, SACW at pycnocline depths, AAIW, UCDW and North Atlantic Deep Water (NADW), and Table 2.2 presents the mean depth of the respective interfaces. Note that the TW-SACW and SACW-AAIW interfaces are placed at

approximately 85.6 m and 602.8 m, respectively, which are close to the respective climatological pressure levels of 89 ± 6 dbar and 563 ± 10 dbar, presented by *Biló et al.* (2014) between 23°S and 26°S. Further deeper we found the AAIW-UCDW interface approximately at 1157.2 m and the UCDW-NADW interface at ~ 1383.4 m.

Table 2.2: Mean depths of water mass interfaces and their associated standard deviations calculated from the CERES IV and CARBOM set of 170 CTD profiles. The interfaces used are expressed in σ_0 and were proposed by *Mémery et al.* (2000). The last column represents the number of profiles where each interface was found.

Interface - σ_0 (kg m^{-3})	Mean (m)	Std (m)	Number of CTD profiles
TW-SACW - 25.60	85.6	34.7	169
SACW-AAIW - 26.90	602.8	66.2	107
AAIW-UCDW - 27.38	1157.2	53.5	89
UCDW-NADW - 27.53	1383.4	51	83

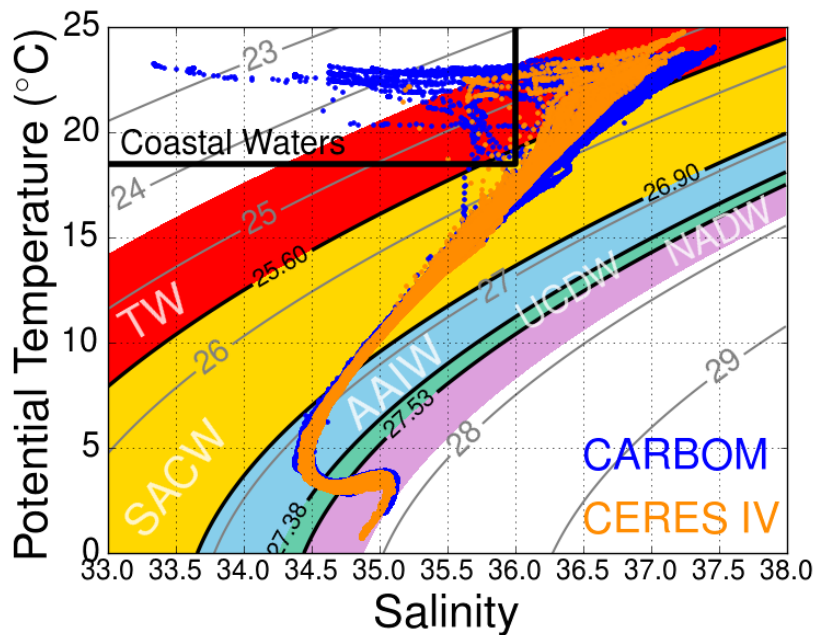


Figure 2.5: The TS Diagram for the CERES IV (orange dots) and CARBOM (blue dots) cruises. The color scheme indicates the observed water masses following the σ_0 interfaces described by *Mémery et al.* (2000) [TW-SACW = 25.60, SACW-AAIW = 26.90, AAIW-UCDW = 27.38, UCDW-NADW = 27.53].

In Figure 2.6, we present the cross-sectional velocity distribution at the transect 24S. During the CERES IV cruise (upper panel) the BC is depicted as the south-southwestward flow (negative velocities) in the upper 500 m (TW and SACW domain), with maximum surface velocities of $\sim -0.45 \text{ m s}^{-1}$ over, approximately, the 1300 m isobath. Note that offshore the 2010 m isobath there is an other near surface velocity maximum of -0.22 m s^{-1} . This second core is clearly depicted in Figure 2.2 at 100

m (panel **a**). Since the BC and IWBC are described in the literature as currents with velocity pattern decaying from their cores (e. g., *Evans and Signorini*, 1985; *Silveira et al.*, 2004; *Biló et al.*, 2014), we considered that the BC signal is confined between 180 m and 2010 m isobaths with a width of ~ 61 km. Considering the cited dimensions and boundaries for the BC, we estimated its cross-section volume transport to be ~ -4.20 Sv ($1 \text{ Sv} = 10^6 \text{ m}^3 \text{ s}^{-1}$).

Underneath the BC, the IWBC flows north-northeastward (positive velocities) with maximum velocities of approximately 0.14 m s^{-1} , a vertical extent of 1000 m (mostly in the AAIW and UCDW layers) and width of ~ 46 km, if we consider as horizontal boundaries the 800 m and 2000 m isobaths. Its volume transport was estimated to be approximately 1.81 Sv, which is almost half of the 3.6 ± 0.8 Sv estimated by *Silveira et al.* (2004) at $\sim 23^\circ\text{S}$ and the 4.11 ± 2.01 Sv at 26°S presented by *Biló et al.* (2014). These estimates were calculated from the velocity profiles measured by the Pegasus profiler³ and the LADCP, respectively. In that sense, we should draw attention to the southwestward flow offshore from the 2010 m isobath at intermediate depths (500-1500 m depth), which has a velocity core of maximum velocities around 0.12 m s^{-1} at the same depth (~ 800 m) of the IWBC's core. Its cross-section volume transport is approximately -2.34 Sv and if we add the 1.81 Sv from the IWBC to that, we have 4.15 Sv, which is a value much closer to the estimates from *Silveira et al.* (2004) and *Biló et al.* (2014), suggesting that part of the intermediate flow could be recirculating over the Santos Plateau during the CERES IV. *Legeais et al.* (2013) temporally averaged the float derived velocity data series in $1^\circ \times 1^\circ$ boxes and computed the eddy kinetic energy (EKE). The mean vectors indicate a southwestward flow offshore from the IWBC at Cape Frio. Moreover, the maximum EKE over the plateau also suggests the presence of such recirculation.

At waters deeper than 1500 m (NADW domain) there is negative velocity signal over the 2010 m to 2649 m isobaths and isolated from the intermediate velocity signal by the isotach of 0.05 m s^{-1} . *Biló et al.* (2014) speculated that a similar signal found at 26°S could be part of the DWBC. However due to the limited observations available more investigation is necessary to confirm this observation.

During the CARBOM cruise (Figure 2.6, lower panel) we observe a BC that vertically extends down to 700 m and horizontally extends from the 662 m to 2243 m isobaths (~ 52 km). Note that the BC velocity signal seems to be incomplete and part of the current is offshore to the 2243 m isobath. In fact, if we go back to the Figure 2.2 (panel **b**) we can verify that the BC actually extends offshore to the 2300 m isobath with a width of ~ 75 km. Its maximum velocities of -0.86 m s^{-1} are at the surface and over the 1535 m isobath.

Similarly to the CERES IV intermediate flow, the IWBC from the CARBOM cruise is right below the BC, however its maximum velocities are at 1200 m depth and reach 0.29 m s^{-1} . There are also small differences concerning the dimensions of the current, which has a vertical extent of approximately 900 m (750-1650 m) and a width of ~ 39 km (1124-2243 m isobaths). This more energetic state of BC system observed during the CARBOM cruise also is reflected in the cross-section volume transport of -9.21 Sv and 2.50 Sv for the BC and IWBC respectively. We should mention that a southwestward flow at depths higher than 1600 m, over the 1915 m and 2243 m isobaths, was also observed.

At transect 25S (Figure 2.7) we present good examples of the BC system meandering activity.

³The direct velocity measurements presented by *Silveira et al.* (2004) were first described by *Evans and Signorini* (1985).

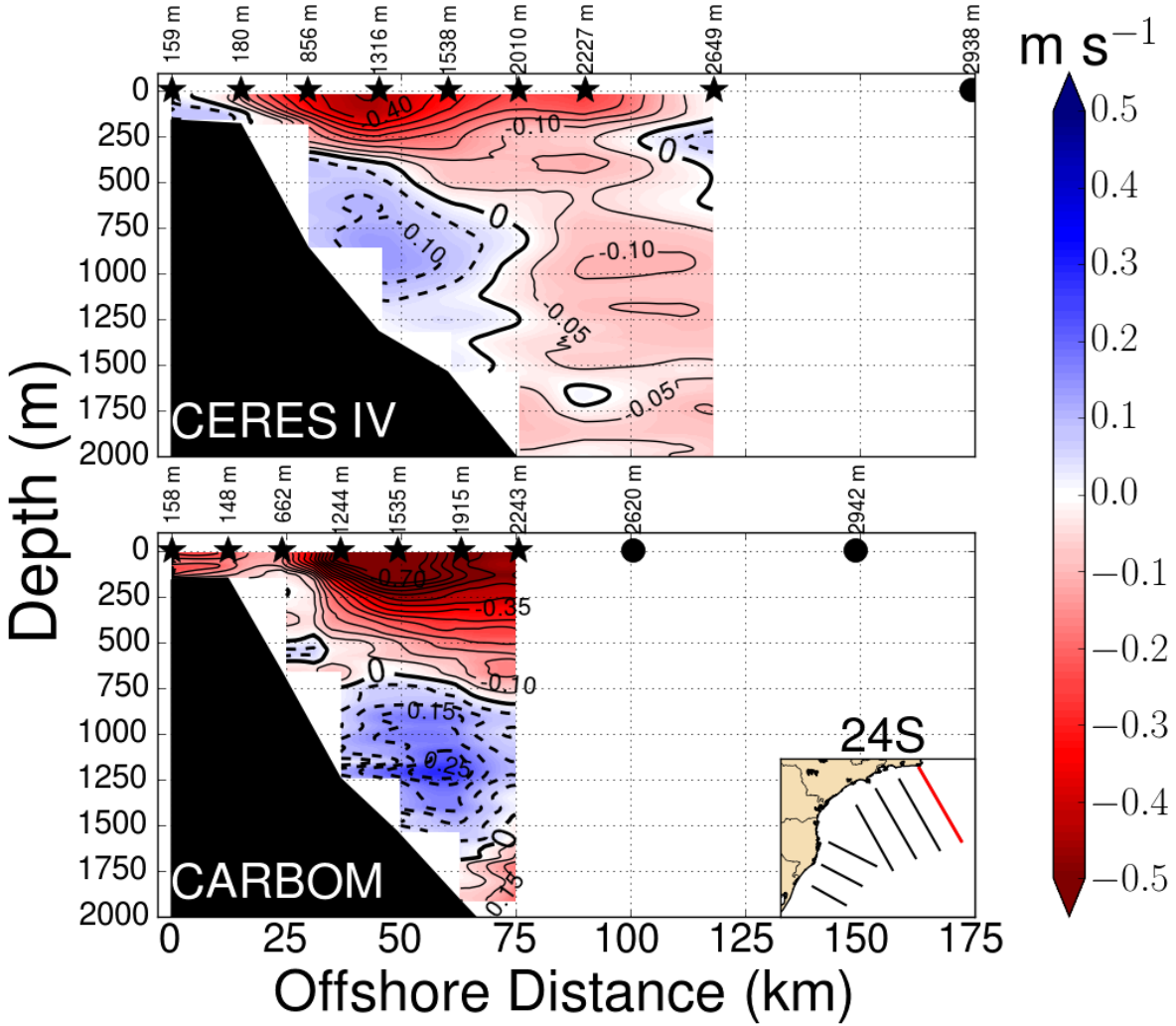


Figure 2.6: Cross-sectional velocity distribution at transect 24S from the CERES IV (upper panel) and the CARBOM cruises (lower panel). Negative velocities are south/southwestward. The stars indicate the locations of the CTD-LADCP profiles, and the circles represent the positions of the stations where only CTD profiles were taken. The numbers indicate the isobaths along the transect.

As mentioned before, the BC is meandering over the continental shelf during the CERES IV cruise (upper panel), so we extended the velocity analysis to part of the shelf (117 m isobath). Note that the southwestward flow supposedly related to the BC signal is limited to the upper 250 m of the water column between the 159 and 1856 m isobaths. As expected in this kind of scenario, the maximum velocities ($>0.30 \text{ m s}^{-1}$) are over the continental shelf, however probably due to an interaction with shelf currents and/or the modification of the velocity signal by different forcing factors such as winds, the BC does not present the parabolic-shape. The BC volume transport offshore to the shelf break (159-1856 m isobaths) was estimated in approximately -2.79 Sv , which differs in -1.41 Sv from what we estimated at 24S. Integrating the velocity over regions shallower than 159 m we obtained a transport of $\sim-1.55 \text{ Sv}$.

Between 250 m and 1250 m depth, we observe two distinguishable positive (north-northeastward) velocity cores. The core that flows over the 685 m to 1686 m isobaths characterizes the IWBC, with

maximum velocities at 960 m of approximately 0.18 m s^{-1} , vertical and horizontal extent of 1000 m and ~ 30 km respectively, and a volume transport around 1.86 Sv . Further offshore the other velocity core at the AAIW domain also has maximum velocities of $\sim 0.18 \text{ m s}^{-1}$, however it is placed right above the 750 m depth and has a cross-section transport of $\sim 3.18 \text{ Sv}$. Note that the IWBC transport estimative is only 0.05 Sv higher than the volume transport at 24S, which supports the idea that the flow close to the topographic boundary crosses the 25S and 24S transects while other portion recirculates offshore, over the Santos Plateau. Moreover, the south-southwestward flow at the NADW layer (depth $> 1383.40 \text{ m}$) is also present at transect 25S.

In contrast, the BC observed during the CARBOM cruise (Figure 2.7, lower panel) flows south-southwestward over the shelf break vicinities (140 m isobath) to the continental slope bottom ($\sim 2018 \text{ m}$ isobath) with a width of 100 km in the upper 500 m. With maximum surface velocities of approximately -0.80 m s^{-1} placed over the 333 m isobath, BC volume transport was estimated in -9.82 Sv . At intermediate depths (500-1750 m), it is possible to observe that the flow crosses the 25S transect equatorward, however no IWBC velocity core signal is noticeable due to the angle between the actual currents and the transect. In that sense most of the AAIW volume transport seems to occur along the transect, so we did not computed the cross-section transport component.

Figure 2.8 depicts the magnitude of the velocity measured during the CARBOM cruise at transect 25S. Note that if we combine it to the cross-sectional velocity distribution presented in Figure 2.7, we are able to identify the velocity core related to the IWBC and speculate about its dimensions. At depths between 500 m and 750 m, there is a velocity maximum of 0.25 m s^{-1} over the 1836 m isobath, which seems to be the IWBC velocity core. It is important to mention that there is no other significant velocity intensification closer to the continental slope topography and the velocity magnitude is in agreement with the IWBC maximum velocities found at transect 24S, which suggests that the IWBC is displaced offshore and closer to the surface than at 24S. The comparison between the positive velocities area in Figure 2.7 (lower panel) and the 0.10 m s^{-1} isotachs from Figure 2.8 suggests that the IWBC is flowing over the 605 m to 2018 m isotachs which corresponds to a width of approximately 60 km, and has a vertical extent of 1000 m. It is worth to mention that the velocity intensification at the most offshore LADCP profile (2204 isobath) and depths greater than 1500 m ($> 0.20 \text{ m s}^{-1}$) is placed where we expect to observe the flow that might be related with part of the DWBC.

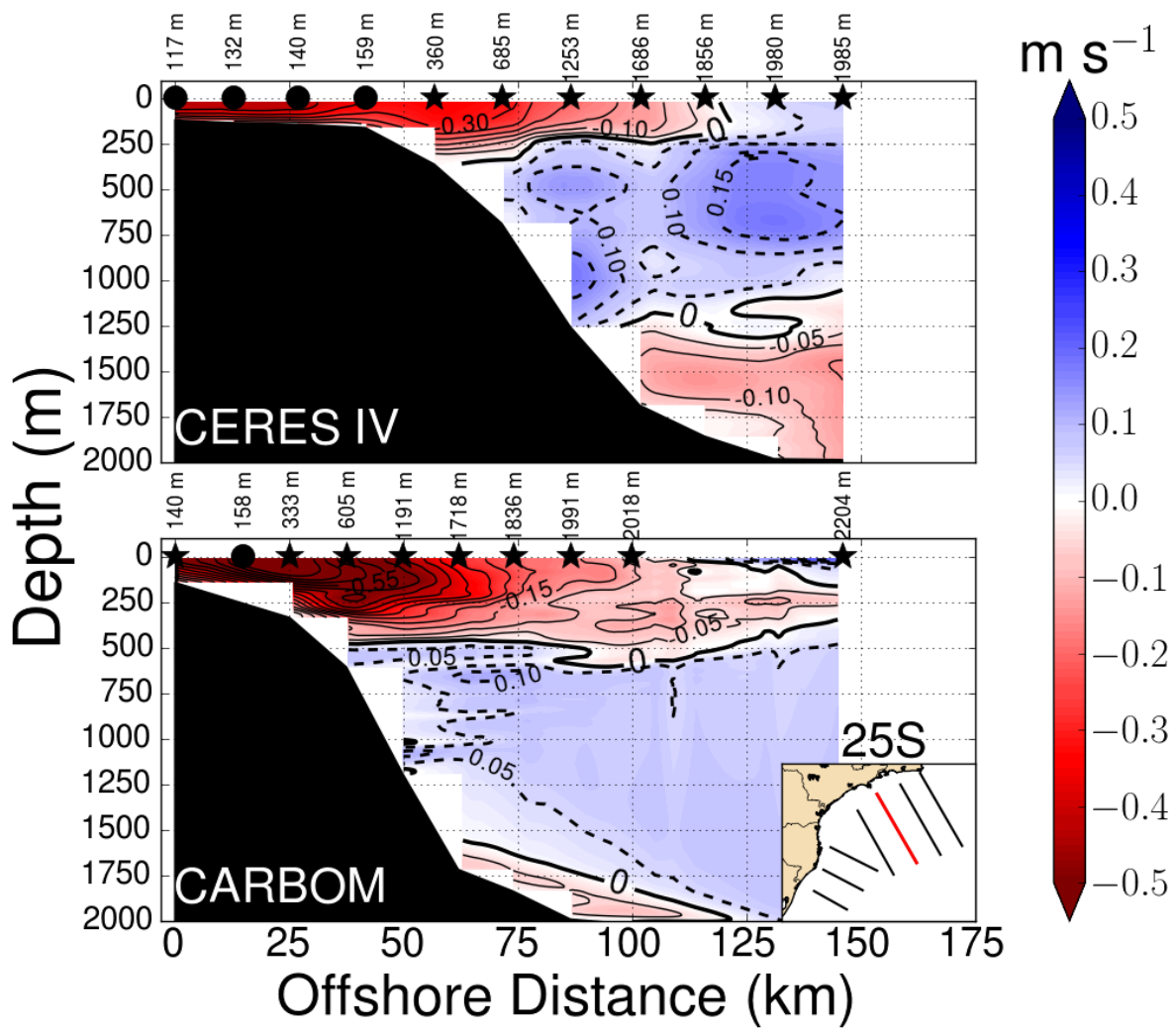


Figure 2.7: Similar to Figure 2.6 but for the transect 25S.

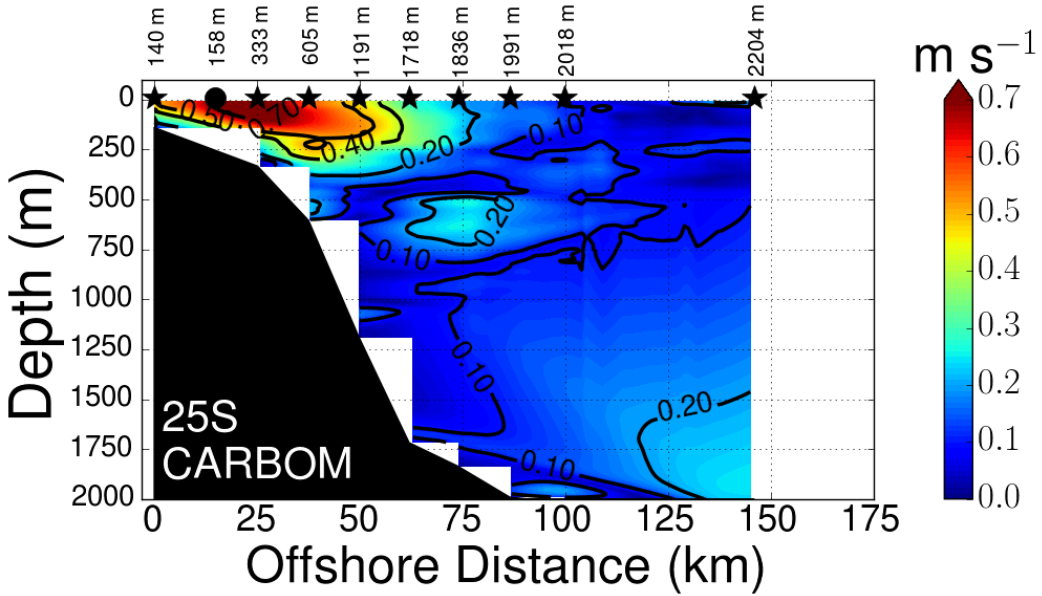


Figure 2.8: Velocity magnitude at transect 25S from the the CARBOM cruise. The stars indicate the locations of the CTD-LADCP profiles, and the circles represent the positions of the stations where only CTD profiles were taken. The numbers indicate the isobaths along the transect.

In Figure 2.9 we present the cross-sectional velocity distributions at transect 26S. The data obtained during the CERES IV cruise (upper panel) were described in detail by [Biló et al. \(2014\)](#). The BC is well defined in the upper 500 m and between the 284 m and 2156 m isobaths. The parabolic-shaped current is centered over the 635 m isobath, has maximum surface velocities of approximately -0.59 m s^{-1} , width of 85 km and consequently a volume transport of -5.75 Sv . At intermediate depths, the IWBC is depicted between the 635 m and 2156 m isobaths, and the depths of 500 m and 1800 m which indicate a current with a width of 60 km and a vertical extent of 1300 m. The IWBC is centered over the 1845 m isobath, its maximum velocities are approximately 0.22 m s^{-1} at the depth of 970 m and volume transport is $\sim 4.11 \text{ Sv}$. As mentioned earlier, [Biló et al. \(2014\)](#) argued that the negative velocity signal at the NADW domain could be part of the DWBC over the Santos Plateau.

The lower panel of Figure 2.9 depicts the BC system observed during the CARBOM cruise. Note that in the first 700 m of the water column the velocity signal inversion over the vicinities of the 1738 m isobath indicates the presence of a cyclonic eddy similar to the one reported by [Campos et al. \(1995\)](#) from geostrophic computations. Its coastal lobe is limited by the 235 m and 1738 m isobaths, which indicates a width of $\sim 50 \text{ km}$, has maximum velocities of approximately 0.38 m s^{-1} located over the 600 m isobath and at the 250 m depth level, has a volume transport of 4.49 Sv . The oceanic lobe has a width of 70 km (1738-2657 m isobaths), with maximum velocities of -0.58 m s^{-1} located over the 2120 m isobath and at the 50 m depth level, and its volume transport is approximately of -5.52 Sv . Therefore the BC net cross-sectional volume transport is $\sim -1.03 \text{ Sv}$.

The IWBC from the CARBOM cruise is depicted by the well defined positive velocity signal between 750 m and 1750 m depth, and over the 1196 m and 2114 m isobaths. This current has a vertical extent of 1000 m, width of $\sim 35 \text{ km}$, maximum velocities approximately 0.27 m s^{-1} place over the

1196 m isobath and the 1125 m depth level, and volume transport ~ 3.01 Sv. We should stress out that there is an important gap of data between 424 m and 1196 m isobaths, which might have led us to underestimate the IWBC dimensions and volume transport. These isobaths are approximately 24 km apart.

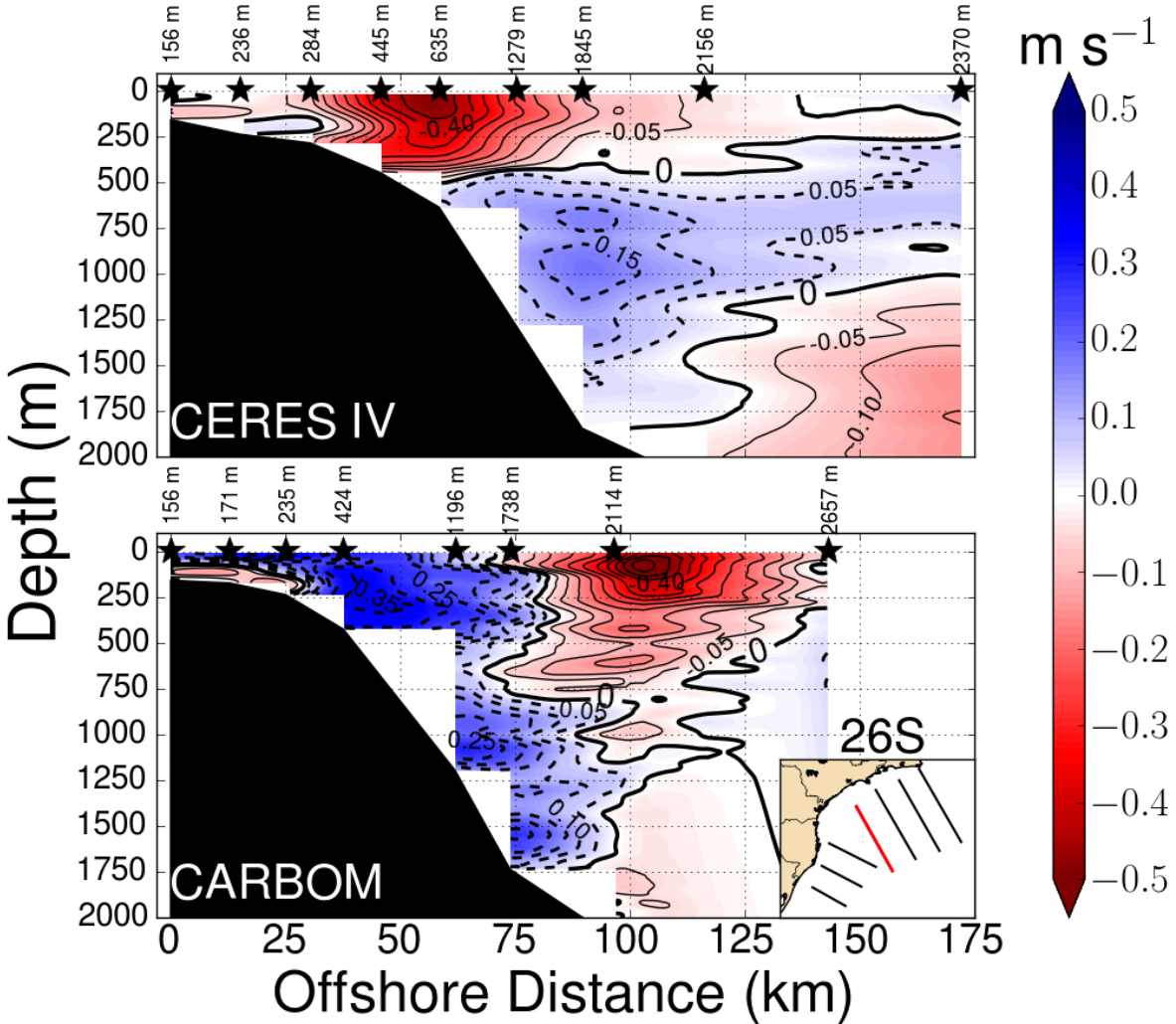


Figure 2.9: Similar to Figure 2.6 but for the transect 26S.

We conclude this section extending our analysis to the CARBOM transects to the south of the Santos Bifurcation ($\sim 27^\circ\text{S}$). In Figure 2.10 we present the cross-sectional velocity distribution at transect 29S. As observed in Figure 2.2, the whole water column over the continental slope seems to present the velocity signal of a cyclonic meander of the BC. Note that its oceanic lobe (over 1490-2046 m isobaths), or the primary axis of the BC, has two prominent velocity cores: the one associated with the BC in the upper 500 m and maximum velocities of -0.37 m s^{-1} ; and the intermediate flow (500-1500 m) associated with the southern branch of the Santos Bifurcation and maximum velocities of $\sim -0.32 \text{ m s}^{-1}$. Although we are not able to observe the entire poleward flow in the transect, we can estimate its horizontal dimension of approximately 70 km based on the velocity signals presented on Figure 2.10 and infer that the lobe is centered over the 1900 m isobath. Additionally, the maximum

velocities of the upper and intermediate cores are placed at 125 m and 900 m depth respectively.

The coastal lobe signal is well defined from the surface to 1000 m depth and between isobaths of 436 m and 1490 m (width \approx 55 km). Moreover, it has one velocity core with maximum velocities of 0.32 m s^{-1} at the depth of approximately 600 m and over the 931 m isobath. Unfortunately it is difficult to evaluate what is the exactly development stage of the meander from one velocity transect, unless the temporal evolution of the meander is well known, nonetheless the presence of only one significant velocity maximum suggests that the perturbation that originates the meander starts growing at intermediate depths. *Mano et al.* (2009) reported a similar behaviour during the the development of a cyclonic meander at 23°S from PE numerical modelling results.

We also computed the volume transport of each lobe by integrating the velocity over the area limited by the cited spacial boundaries in the previous paragraphs. The coastal lobe has a transport of approximately 4 Sv and the oceanic one -13.16 Sv, which indicates a BC system net volume transport of -9.16 Sv. Then, if we compare the -13.16 Sv with the -5.52 Sv, which is the BC oceanic lobe transport at the transect 26S, we can conclude that the Santos Bifurcation is responsible for an increase of approximately 7.64 Sv in the BC poleward transport during the CARBOM cruise. Note that the -7.64 Sv is higher than the IWBC transport of 3.01 Sv at transect 26S, which suggests that $\sim 30\%$ of the total amount of water ($7.64 \text{ Sv} + 3.01 \text{ Sv} = 10.65 \text{ Sv}$) that is splitted by the Santos Bifurcation flow north with the IWBC corroborating the *Legeais et al.* (2013) geostrophic estimates.

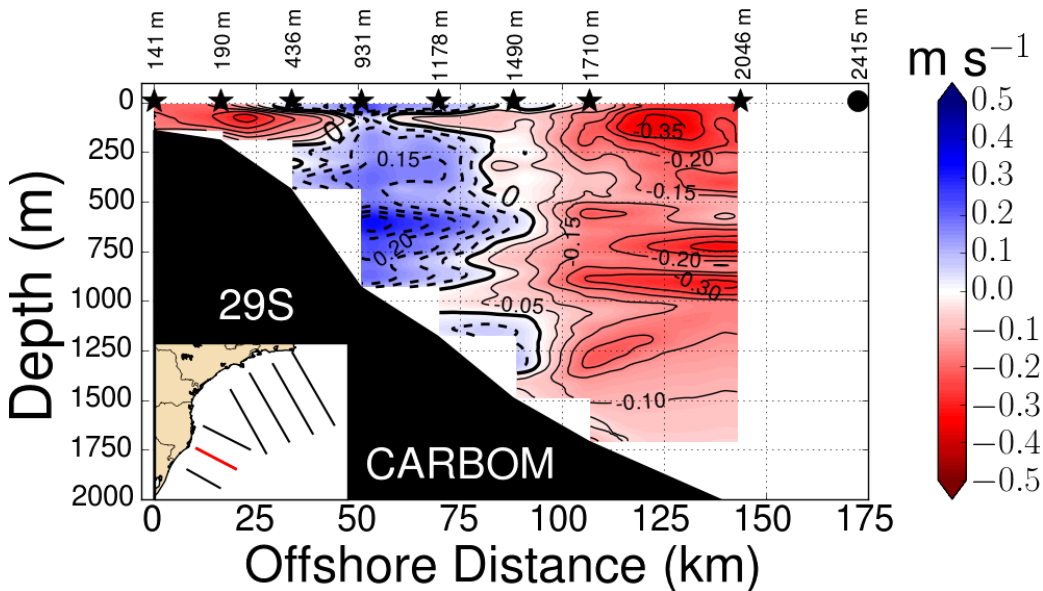


Figure 2.10: Cross-sectional velocity distribution at transect 29S from the CARBOM cruise. Negative velocities are south/southwestward. The stars indicate the locations of the CTD-LADCP profiles, and the circles represent the positions of the stations where only CTD profiles were taken. The numbers indicate the isobaths along the transect.

Finally, Figure 2.11 depicts the velocity distribution at transect 30S. Note that the BC and the intermediate flow are organized in a single velocity core extending down to 1000 m and width of ~ 100 km. The maximum velocities of approximately -0.52 m s^{-1} are placed over the 550 m isobath at ~ 90 m depth level. Additionally, the volume transport integrated over the area horizontally limited

by the isobaths 184 m and 1960 m, and the surface and 1300 m depth was estimated in approximately -11 Sv.

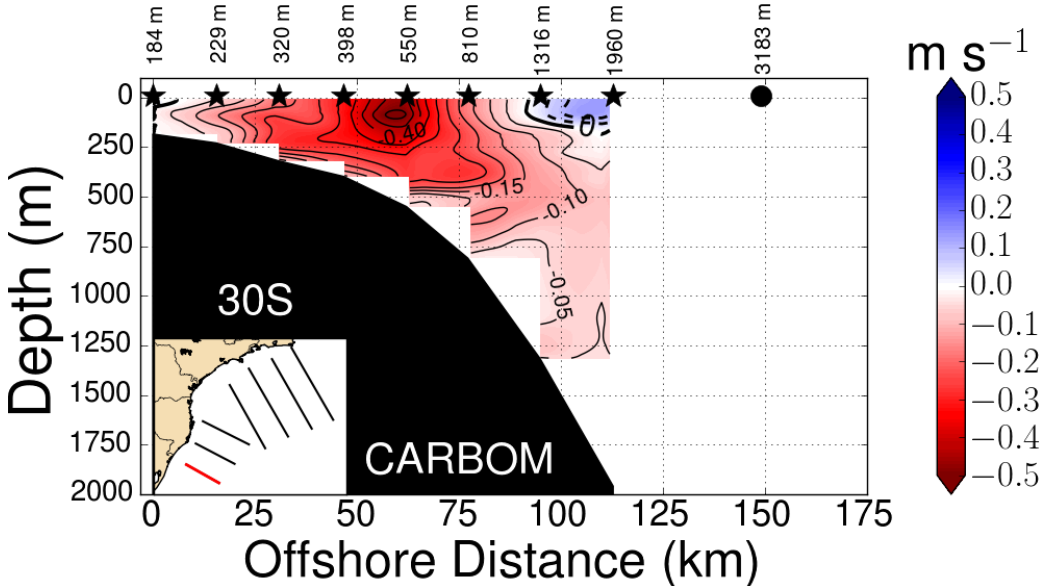


Figure 2.11: Similar to Figure 2.10 but for the transect 30S.

In order to summarize the downstream changes of the BC, we present the primary characteristics of the current in Table 2.3. The first noticeable characteristic is that the BC was more energetic to the north of the Santos Bifurcation during the CARBOM cruise, due to the larger dimensions and the higher velocities of the current. Secondly, the eddy characteristics to the north and to south of the Santos Bifurcation are clearly distinct. The transect 29S shows the intermediate flow of the AAIW and UCDW (500-1500 m) recirculating with the upper flow of the TW and SACW (0-500 m), which does not occur at transects 25S (CERES IV) and transect 26S (CARBOM). At the last two transects, the perturbations of the BC and the IWBC seems to behave more independently. Finally, the BC experiences an increase in the volume transport as it flows poleward, except at transect 30S, due to the reasons already discussed.

Table 2.3 also indicates that the BC transport increase between transects 24S and 26S is due by a different reason than the increase between transects 26S and 29S. As mentioned before the Santos Bifurcation is responsible for an increase of ~7.64 Sv to the BC between transects 26S and 29S, and therefore due to the BC vertical thickening. However, Table 2.3 shows no evident vertical thickening between transects 24S and 26S, instead a significant widening is observed as it flows poleward. *Rocha et al. (2014)* argued based on mooring records at 22.7°S and 25.5°S that the BC also thickens southward, although at a smaller rate than at the Santos Bifurcation area. However the authors did not consider the relative position of the mooring lines to the BC core and the topographic changes. *Rocha et al. (2014)* argued that the mooring at 25.5°S is closer to the BC core than the other, which suggests that even if the BC reaches the same depth at both locations their analysis would indicate a thicker current at 25.5°S due to its parabolic-shape. Moreover, to the north of the Santos Plateau area (23°S-28°S) the continental slope steepness is steeper, which means that the IWBC tends to flow right

underneath the BC in this area and displaced offshore to the south of 24°S (e. g., *Rocha et al.*, 2014; *Biló et al.*, 2014), since the IWBC is highly constrained by the slope topography (*Boebel et al.*, 1999; *Legeais et al.*, 2013).

Table 2.3: Primary characteristics of the BC cross-sectional velocity signal at each transect.

Transect	Width (km)	Thickness (m)	Maximum velocity (m s ⁻¹)	Transport (Sv)
CERES IV				
24S	61	500	-0.45	-4.20
25S*	-	250	-	-
26S	85	500	-0.59	-5.75
CARBOM				
24S	75	750	-0.86	-9.21
25S	100	500	-0.80	-9.82
26S**	120	700	0.38 -0.58	4.49 -5.52
29S**	125	1500	0.32 -0.37	4 -13.16
30S	100	1300	-0.52	-11

*Due to the BC meandering over the shelf we were not able to estimate its dimensions and total transport

**Presence of a cyclonic meander: width represents the diameter of the meander; and we present the maximum velocities and volume transport observed in each lobe.

2.3 Linear instability analysis

In order to relate the BC downstream changes described in the previous section with the properties of geophysical instabilities, and answer the guiding questions we performed numerical experiments. We opted for a linear instability sectional model that was already applied for similar purposes in other western boundary currents. The PE frontal instability model created by *Moore and Peltier* (1987) was adapted by *Xue and Mellor* (1993) to study the Gulf Stream instability in the South Atlantic Bight. *James et al.* (1999) employed the same model to investigate the dynamics of the Kuroshio Current in East China Sea. They reduced the parameter space and optimized the numerical code performance.

2.3.1 The Model

The model uses PE linearized around a background state. This background consists of a velocity field $V(x, z)$, its associated buoyancy field $B(x, z)$ (Equation 2.1) and a topography profile $h(x)$. The coordinate system is given by: x cross-stream, y downstream and z vertically upward from the sea surface.

$$B(x, z) = \frac{-g\bar{\rho}(x, z)}{\rho_0}, \quad (2.1)$$

where g is the acceleration due to gravity, $\bar{\rho}(x, z)$ is the background density field and ρ_0 is the reference density. The PE in terms of the background state are shown in Equations 2.2 to 2.6.

$$\left(\frac{\partial}{\partial t} + V \frac{\partial}{\partial y}\right) u - f v + \frac{1}{\rho_0} \frac{\partial p}{\partial x} = 0 \quad (2.2)$$

$$\left(\frac{\partial}{\partial t} + V \frac{\partial}{\partial y}\right) v + f u + u \frac{\partial V}{\partial x} + w \frac{\partial V}{\partial z} + \frac{1}{\rho_0} \frac{\partial p}{\partial y} = 0 \quad (2.3)$$

$$b - \frac{1}{\rho_0} \frac{\partial p}{\partial z} = 0 \quad (2.4)$$

$$\frac{\partial u}{\partial x} + \frac{\partial v}{\partial y} + \frac{\partial w}{\partial z} = 0 \quad (2.5)$$

$$\left(\frac{\partial}{\partial t} + V \frac{\partial}{\partial y}\right) b + u \frac{\partial B}{\partial x} + w \frac{\partial B}{\partial z} = 0, \quad (2.6)$$

where u , v , and w represent the x , y and z components of the perturbation velocity; p is the perturbation pressure; b is the perturbation buoyancy; t is time; and f the Coriolis parameter. Then the numerical solutions for the instability problem are obtained by using a rectangular domain with the boundary conditions presented by Equation 2.7 and the vertical stretched coordinate system defined in Equation 2.8.

$$\begin{cases} u = 0 & \text{at } x = 0 \\ p, u \text{ and } v \rightarrow 0 & \text{at } x \rightarrow \infty \\ w = 0 & \text{at } z = 0 \\ w = -u \frac{\partial h}{\partial x} & \text{at } z = -h(x) \end{cases} \quad (2.7)$$

$$\zeta = 1 + \frac{z}{h(x)}, \quad (2.8)$$

consequently we can redefine the velocity vertical component in the new coordinated system as

$$\omega = w - (\zeta - 1) u \frac{\partial h}{\partial x}. \quad (2.9)$$

The numerical model is built using the transport forms of u , v and b (Equation 2.10) and the dimensionless form following Equation 2.11.

$$(u^*, v^*, b^*) = (u h, v h, b h) \quad (2.10)$$

$$\begin{aligned} (x', y') &= \frac{(x, y)}{L_0}, \quad t' = t f, \quad h' = \frac{h}{H_0}, \quad (u', v') = \frac{(u^*, v^*)}{u_0 H_0}, \quad \omega' = \frac{L_0}{H_0} \frac{\omega}{u_0}, \\ p' &= \frac{p}{\rho_0 u_0 f L_0}, \quad b' = \frac{b^*}{u_0 f L_0}, \quad B' = \frac{B}{H_0 N_0^2}, \quad V' = \frac{V}{V_0}, \end{aligned} \quad (2.11)$$

where L_0 is horizontal length scale, H_0 is the maximum depth, u_0 is the typical perturbation velocity scale, N_0^2 is the maximum vertically averaged $\frac{\partial B}{\partial z}$ and V_0 is the maximum value of V . Replacing Equations 2.8-2.11 in 2.2-2.6 and dropping the primes for convenience,

$$\left(\frac{\partial}{\partial t} + RoV\frac{\partial}{\partial y}\right)u - v + h\frac{\partial p}{\partial x} - (\zeta - 1)\frac{\partial h}{\partial x}\frac{\partial p}{\partial \zeta} = 0 \quad (2.12)$$

$$\left(\frac{\partial}{\partial t} + RoV\frac{\partial}{\partial y}\right)v + u + Ro(u\frac{\partial V}{\partial x} + \omega\frac{\partial V}{\partial \zeta}) + h\frac{\partial p}{\partial y} = 0 \quad (2.13)$$

$$b - \frac{\partial p}{\partial \zeta} = 0 \quad (2.14)$$

$$\frac{\partial u}{\partial x} + \frac{\partial v}{\partial y} + \frac{\partial \omega}{\partial \zeta} = 0 \quad (2.15)$$

$$\left(\frac{\partial}{\partial t} + RoV\frac{\partial}{\partial y}\right)b + S(u\frac{\partial B}{\partial x} + \omega\frac{\partial B}{\partial \zeta}) = 0, \quad (2.16)$$

where $Ro = \frac{V_0}{L_0 f}$ is the Rossby number and $S = (\frac{N_0 H_0}{f L_0})^2$ is the Burger number. The studied perturbations are assumed to be oscillatory with a downstream propagation of the form

$$u = Re[\tilde{u}(x, \zeta)e^{i(\sigma t + \beta y)}] \quad (2.17)$$

$$v = Re[i\tilde{v}(x, \zeta)e^{i(\sigma t + \beta y)}] \quad (2.18)$$

$$\omega = Re[\tilde{\omega}(x, \zeta)e^{i(\sigma t + \beta y)}] \quad (2.19)$$

$$b = Re[i\tilde{b}(x, \zeta)e^{i(\sigma t + \beta y)}] \quad (2.20)$$

$$p = Re[i\tilde{p}(x, \zeta)e^{i(\sigma t + \beta y)}], \quad (2.21)$$

where β is the perturbation downstream wavenumber and $\sigma = \sigma_r + i\sigma_i$ (σ_r = perturbation frequency; $-\sigma_i$ = growth rate). In order to build the eigenvalue problem, the perturbation amplitudes ($\tilde{u}, \tilde{v}, \tilde{\omega}, \tilde{b}$ and \tilde{p}) were decomposed into a Fourier series using a spectral technique (Equations 2.22 to 2.30).

$$\tilde{u} = \sum_{\nu=0}^{\infty} \sum_{\lambda=0}^{\infty} u_{\lambda\nu} E_{\nu} \psi_{\lambda} \quad (2.22)$$

$$\tilde{v} = \sum_{\nu=0}^{\infty} \sum_{\lambda=0}^{\infty} v_{\lambda\nu} E_{\nu} \phi_{\lambda} \quad (2.23)$$

$$\tilde{\omega} = \sum_{\nu=0}^{\infty} \sum_{\lambda=0}^{\infty} \omega_{\lambda\nu} F_{\nu} \phi_{\lambda} \quad (2.24)$$

$$\tilde{b} = \sum_{\nu=0}^{\infty} \sum_{\lambda=0}^{\infty} b_{\lambda\nu} F_{\nu} \phi_{\lambda} \quad (2.25)$$

$$\tilde{p} = \sum_{\nu=0}^{\infty} \sum_{\lambda=0}^{\infty} p_{\lambda\nu} E_{\nu} \phi_{\lambda}. \quad (2.26)$$

$$E_{\nu} = \cos(\nu\pi\zeta) \quad (2.27)$$

$$F_{\mathcal{V}} = \sin(\mathcal{V}\pi\zeta) \quad (2.28)$$

$$\phi_\lambda = \cos\left(\frac{\lambda\pi x}{L}\right) \quad (2.29)$$

$$\psi_\lambda = \sin\left(\frac{\lambda\pi x}{L}\right), \quad (2.30)$$

where L is the domain width. The series is truncated ($\mathcal{V} = 0, 1, \dots, N$; $\lambda = 0, 1, \dots, N - \mathcal{V}$) to make the problem numerically solvable. When the truncation level (N) and β are specified, the model solves the problem for σ (eigenvalues) and for the truncated series coefficients (eigenvectors). The detailed implementation of the spectral model is given by [Xue and Mellor \(1993\)](#) and [James \(1996\)](#).

2.3.2 The background states parameterization

The first, and most important, step in preparing the model is to define the background, or basic state. The background state can be thought as a transect where the cross-sectional velocity distribution [$V(x, z)$] are “not perturbed”, or closest to a mean state. In that sense, we selected from our data set the velocity transects that resemble the probable mean state of the BC system reported in the literature. Unfortunately there is neither observational work that described the mean full velocity structure of the BC system, nor a data base which could allow us to estimate it. Hence, we based the choice of the transects on the position of the velocity core and maximum velocities. Other authors have dealt with the same issue in investigating the stability of other western boundary current systems. [Johns \(1988\)](#) used Pegasus velocity profiles and geostrophic calculations to obtain his profile. [James et al. \(1999\)](#) opted to use a geostrophic quasi-synoptic transect instead of a mean state inferred geostrophically from an inverted echosounder array, in order to keep the velocity lateral shear.

It is well known that the inshore boundary of the BC is well-marked by a surface thermal front ([Garfield, 1990](#); [Silveira et al., 2008](#); [Lorenzetti et al., 2009](#)). The sea surface temperature imagery analysis carried out by [Garfield \(1990\)](#) and [Silveira et al. \(2008\)](#) show that the mean BC thermal front is located around the 200 m isobath between 23°S and 30°S. Therefore we should look for the scenarios where the BC inshore boundary is placed in the vicinities of the shelf break. Moreover, considering such scenarios, historical and recent observations depict the BC with maximum velocities ranging from 0.3 to 0.7 m s⁻¹ (e. g., [Evans and Signorini, 1985](#); [Campos et al., 1995](#); [Silveira et al., 2001, 2004](#); [Oliveira et al., 2009](#); [Rocha et al., 2014](#)).

Since we intend to evaluate the Santos Bifurcation impact on the instability processes and, consequently, the role of the vertical shear, we should also take into account the intermediate flow, especially to the north of 27°S. The Lagrangian floats analysis carried out by [Boebel et al. \(1999\)](#) and expanded by [Legeais et al. \(2013\)](#) comprises the best assessment of the mean characteristics of the IWBC until now. In a mean term the IWBC’s width does not exceed 100 km, its core is placed approximately 20 km from the 800 m isobath at ~800-1000 m depth, and the maximum velocities can reach ~0.30 m s⁻¹.

We therefore concluded that the transects 24S and 26S from CERES IV cruise, and the transect 30S from the CARBOM cruise are the most adequate velocity distributions to be used in the instability

analysis. Moreover this set of transects clearly exemplified the BC downstream changes (see Table 2.3). From now on, these transects will be referred as transects 24S, 26S and 30S for simplicity, respectively.

For initializing the model, we defined analytical representations of the chosen cross-sectional velocity distributions and topography. We carried out this procedure for two reasons. First, the gradients of topography and velocity (horizontal and vertical) required to solve the stability problem can be found without finite difference errors. Secondly, we can easily change the background characteristics by altering the functions parameters, in order to perform sensitivity experiments.

The set of equations which describes the parametric model is directly based on the models proposed by *Luther and Bane* (1985), *James et al.* (1999) and *Schmidt et al.* (2007) (Equations 2.31 to 2.34). The model is function of the distance from the inner continental shelf x and the depth z . All the unspecified parameters were determined via non-linear least square fitting in which the root-mean-square (RMS) difference between the analytical velocity field $V(x, z)$, the topographic profile $h(x)$, and the observations was minimized. We used Equation 2.31 to represent the different topography profiles in each numerical experiment. Moreover, two distinct parametric models were used to represent the velocity field to the north and to the south of the Santos Bifurcation. To the north of the bifurcation (24S and 26S), we defined the BC system (Equation 2.32) as the sum of the BC and IWBC signals ($V(x, z) = V_{bc} + V_{iwb}$).

$$h(x) = H_s + \frac{1}{2}(H_d - H_s)[1 + \tanh(\frac{x - X_m}{\alpha})] \quad (2.31)$$

$$\left\{ \begin{array}{l} V_{bc}(x, z) = V_{c0} \exp(-[\frac{z}{Z_s}]^2) \exp(-[\frac{x - (X_{c0}\beta_p)}{L}]^2) \\ \qquad \qquad \qquad \left\{ \begin{array}{l} L = L_c, \text{ se } x \leq X_{c0} \\ L = L_o, \text{ se } x > X_{c0} \end{array} \right. \\ \\ V_{iwb}(x, z) = V_{ci0} \exp(-[\frac{z - (Z_{ci0}\gamma_i)}{h_i}]^2) \exp(-[\frac{x - (X_{ci0}\beta_{pi})}{L_i}]^2) \\ \qquad \qquad \qquad \left\{ \begin{array}{l} h_i = h_{is}, \text{ se } z \leq Z_{ci0} \\ h_i = h_{ib}, \text{ se } z > Z_{ci0} \\ L_i = L_{ic}, \text{ se } x \leq X_{ci0} \\ L_i = L_{io}, \text{ se } x > X_{ci0} \end{array} \right. \end{array} \right. , \quad (2.32)$$

where $\beta_p(z)$, $\beta_{pi}(z)$, $\gamma_i(x)$ are defined by Equation 2.33.

$$\left\{ \begin{array}{l} \beta_p(z) = 1 - \frac{z}{Z_s A} \\ \beta_{pi}(z) = 1 - \frac{z}{Z_{is} A_i} \\ \gamma_i(x) = 1 - \frac{x}{X_{is} B_i} \end{array} \right. . \quad (2.33)$$

The velocity pattern to the south of the Santos Bifurcations (30S) was defined by the sum of three exponentials functions [$V(x, z) = V_u + G_1 + G_2$] given by Equation 2.34. After the least square fitting with the observations, the background buoyancy fields [$B(x, z)$] were obtained by numerically integrating the thermal wind relation from the offshore boundary to the coastal boundary of the domain.

The most offshore CTD-LADCP hydrographic profile, in each transect, was used to calculate the $B(x, z)$ profile as boundary condition for the integration.

$$\begin{cases} V_u(x, z) = V_{c0} \exp\left(\frac{-z^2}{Z_s^2}\right) \exp\left(-\left[\frac{x - (X_{c0}\beta_p)}{\ell}\right]^2\right) \\ G_1(x, z) = G_{10} \exp\left(-\left[\frac{z - G_{1Z}}{G_{1Zs}}\right]^2\right) \exp\left(-\left[\frac{x - G_{1X}}{G_{1L}}\right]^2\right) \\ G_2(x, z) = G_{20} \exp\left(-\left[\frac{z - G_{2Z}}{G_{2Zs}}\right]^2\right) \exp\left(-\left[\frac{x - G_{2X}}{G_{2L}}\right]^2\right) \end{cases} \quad (2.34)$$

We should mention that the model domain is larger than the real transect. It is desirable for the horizontal density gradient ($\frac{\partial \bar{\rho}(x, z)}{\partial x}$) and $V(x, z)$ to decay to zero at the lateral boundaries, therefore we set the domain width to be large enough to ensure the fronts isolation from these boundaries. In addition, we wanted to keep the continental shelf and slope proportional to the real features. The grids were built with 103 horizontal points and 200 vertical levels.

Topography parameterization

In panel **a** of the Figure 2.12, the topography parameterization of the transect 24S is depicted. Observe that the analytical function for $h(x)$ reproduce well the steepness of the continental slope, however the depths near the shelf break are over-estimated. The chosen exponential form of the model (Equation 2.31) does not allow us to perfectly fit the shelf-break and slope steepness at the same time. Moreover, it is important to mention that the BC system is centred around the ~ 1300 m isobath, which corresponds to the middle of the slope, and just the BC's coastal lobe edge is near the shelf break (Figure 2.6, upper panel). In that sense, based on [Xue and Mellor \(1993\)](#) and [James et al. \(1999\)](#) findings with the same model, we should expect the disturbances to be more influenced by the slope steepness. Nevertheless we are aware that the shelf break depth has an impact on the stability properties of the BC. [James et al. \(1999\)](#) results regarding their shallower shelf experiment (K_{SD50}) suggest that a shallower shelf break may increase the "stiffness" (resistance to meandering), which would favour the development of shorter-period oscillations.

In contrast, the higher difference between observations and the model for transect 26S is located at the most offshore station (Figure 2.12, panel **b**). This station is located more than 100 km far from the BC and IWBC cores (Figure 2.6, upper panel), thus it will not represent a problem. Further south, the function proposed for the topographic profile in transect 30S (2.12, panel **c**) reproduced well all the observed characteristics. Additionally, we compared the models with the 1 arc-minute global relief model of Earth's surface (ETOPO 1), National Oceanic and Atmospheric Administration (NOAA). This data set integrates land topography and ocean bathymetry and it is built from numerous global and regional data sets ([Amante and Eakins, 2009](#)). Note that the models have limitations, nevertheless they reproduce well the topographic features at each transect.

Velocity parameterization

We considered a suitable model for the background state, the analytical functions which produced good a representation of the observed velocity distribution, cross-sectional volume transport, vertical

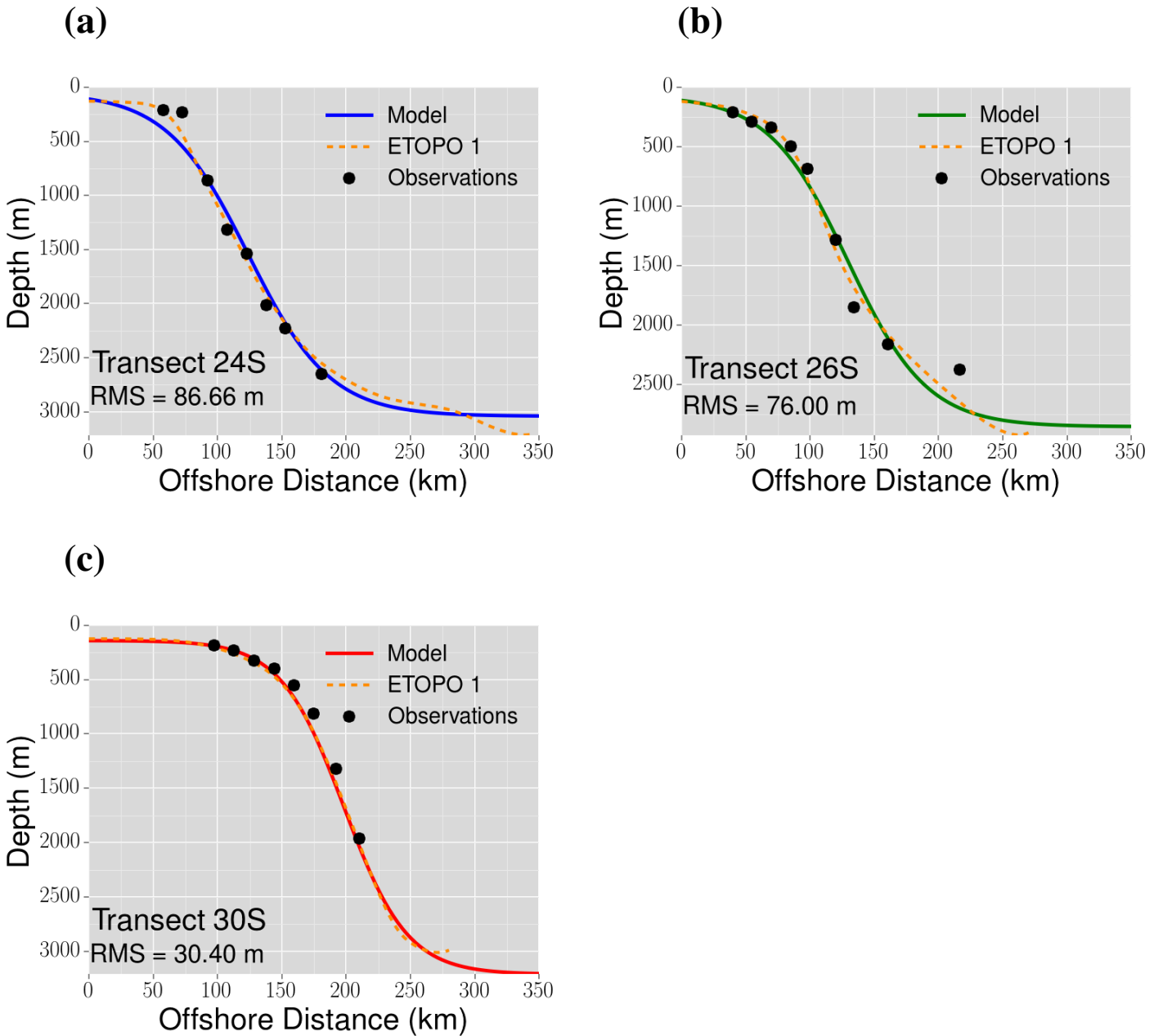


Figure 2.12: Parameterization of the topographic profiles (solid line) at transects **(a)** 24S, **(b)** 26S and **(c)** 30S. The local depth at each CTD-LADCP stations (dots) and the smoothed topographic profile from ETEPO 1 [orange dashed line] ([Amante and Eakiins, 2009](#)) are also presented.

and horizontal velocity shears. To make this assessment we discussed the results presented in Figures 2.13-2.16. Figure 2.13 presents the observed cross-sectional velocity distributions (upper panels) and the respective models $V(x, z)$ (lower panels); Figure 2.14 depicts the absolute velocity difference between the observations and the parametric models; and Figures 2.15 and 2.16 show comparisons of the resulting vertical and horizontal velocity shears of the BC and IWBC respectively.

At transect 24S (Figure 2.13, panels **a**), the model was able to reproduce the dimensions, position and shape of BC system velocity cores (e. g., Section 2.2.2). The BC flows to the southwest in the upper 400-500 m with maximum surface velocities of approximately -0.45 m s^{-1} and a width of $\sim 70 \text{ km}$. At intermediate depths, the IWBC is depicted flowing northeastward with maximum velocities of approximately 0.13 m s^{-1} , a vertical extent of 1000 m and width of $\sim 50 \text{ km}$. Consequently, the model also performed well in estimate the volume transport, since it generated a BC transporting -3.74

Sv and an IWBC with 1.72 Sv, which differ \sim 10% from the -4.20 Sv and 1.81 Sv estimated from the observations for the BC and the IWBC respectively.

With the intent to visualize where the limitations of the proposed model are, we calculated the velocity at the observations locations and subtracted it from the observed velocities (Figure 2.14). The absolute velocity difference distribution at transect 24S (panel **a**) shows that the largest differences ($0.1\text{--}0.22 \text{ m s}^{-1}$) are located at the surface, but off the BC system area. In general, within the BC system domain, the differences are less than 0.05 m s^{-1} . Note that there are smaller regions in the area of interest, where the absolute differences are larger than 0.05 m s^{-1} , however these values are not enough to mischaracterize the general velocity pattern.

Additionally we evaluated the vertical ($\frac{\partial V}{\partial z}$) and horizontal ($\frac{\partial V}{\partial x}$) velocity shears by comparing the velocity profiles at the BC and IWBC cores (Figures 2.15 and 2.16). Because the velocity signal measured with the LADCP and VMADCP corresponds to the total water velocity, the velocity fields are noisy and its associated shear might be difficult to interpret. In that sense we linearly interpolated the observations, in both directions, and smoothed the resulting velocity distributions. This procedure allowed us to obtain smoothed velocity shear (horizontal and vertical) profiles associated with the BC system velocity signal, “without” smaller scale motions interference. It is important to mention that the smoothing process did not change the maximum (and minimum) velocities and kept the transports of volume.

Near Cape Frio (24S), the $\frac{\partial V}{\partial z}$ and $\frac{\partial V}{\partial x}$ are presented by panels **a** in Figures 2.15 and 2.16 respectively. Note that the $\frac{\partial V}{\partial x}$ was well reproduced by the model in the BC system domain, especially close to the coastal boundary ($x \leq 110 \text{ km}$). However it is seen, from the $\frac{\partial V}{\partial z}$ profile that the model did not perfectly reproduce the velocity vertical structure. Although the current vertical dimensions, maximum velocity and value of the maximum $\frac{\partial V}{\partial z}$ are in agreement with the observations, the velocity vertical profile shape is slightly different. In the model, the velocity decays exponentially from the surface [$\exp(-\frac{z}{Z_s})$ in Equation 2.32], however the observed profile shows that the maximum velocities extends down to $\sim 100 \text{ m}$ (low variation). In this case the maximum $\frac{\partial V}{\partial z}$ is located between 200 and 350 m.

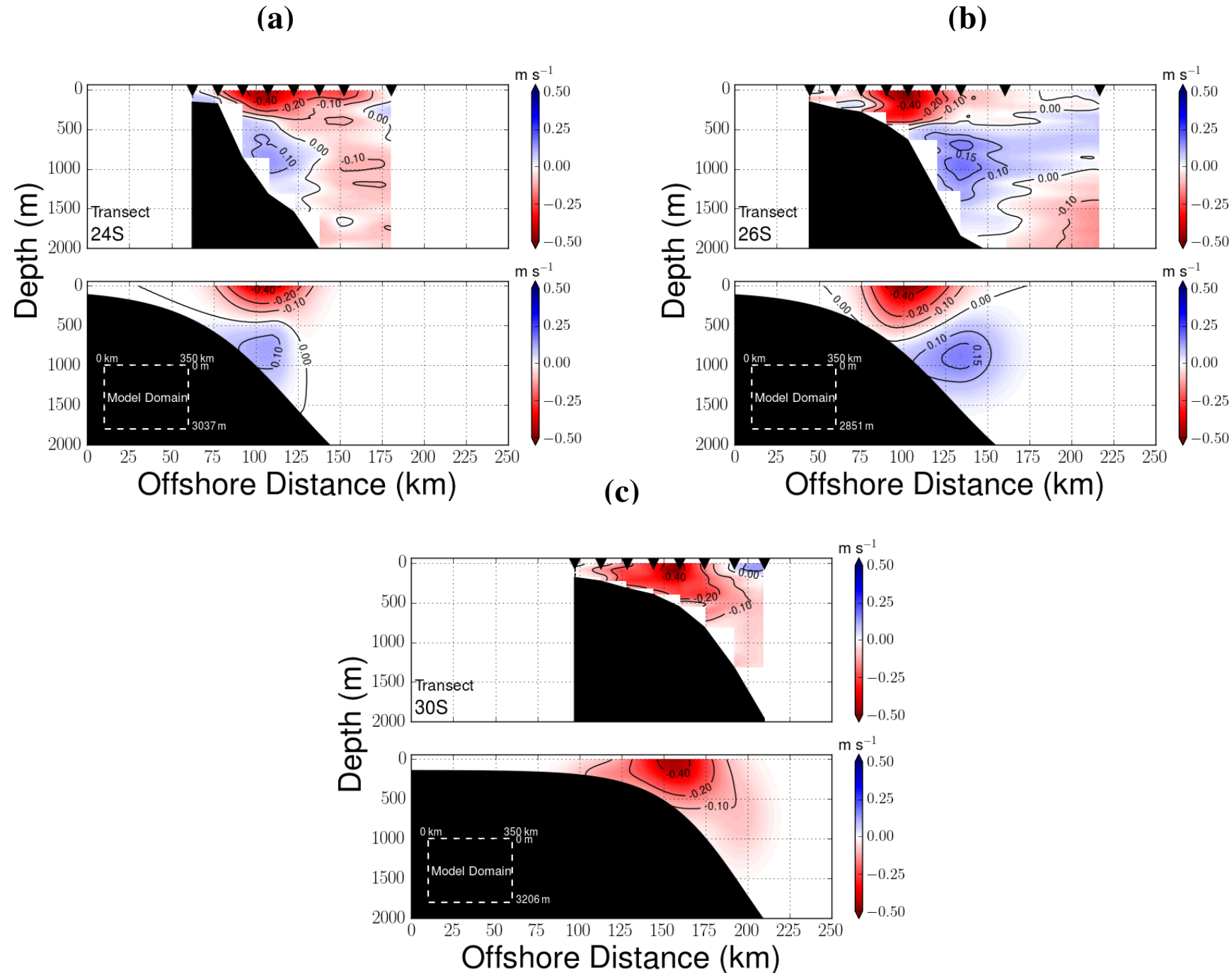


Figure 2.13: The observed cross-sectional velocity distributions (upper panels) and the respective parametrized velocity field (lower panels) at transect (a) 24S, (b) 26S and (c) 30S. Negative velocities are south-southwestward, and the triangles indicate the locations of the CTD-LADCP profiles. The numbers presented with the model domain represent its physical boundaries.

The same reasoning was applied in the analysis of the proposed models for the transects further south. At transect 26S (Figure 2.13, panels **b**), the model representation of $V(x, z)$ has the general characteristics of the observed field. The parametrized parabolic-shaped BC has a vertical extent of ~ 570 m, maximum velocities of -0.50 m s^{-1} , a width of the order ~ 100 km and a transport of approximately -5.93 Sv . These values are in a good agreement with values presented in Table 2.3. At intermediate depths, the parametrized (observed) IWBC is depicted flowing northeastward with a maximum velocity of approximately 0.20 m s^{-1} (0.22 m s^{-1}), a vertical extent of $1,700$ m ($1,800$ m) and a volume transport $\sim 4.51 \text{ Sv}$ (4.11 Sv). As pointed out by [Biló et al. \(2014\)](#), the large distance between the most offshore stations (56 km), does not allow us to precise the IWBC's horizontal dimension, however its signal is well defined between $x \sim 100$ and 160 km. In that sense the model has an adequate velocity horizontal decay coefficients.

In terms of absolute velocity differences between the observations and the model (Figure 2.14, panel **b**), the largest values ($\geq 0.10 \text{ m s}^{-1}$) are restricted to the deep southwestward flow area, which is off the BC system domain (Figure 2.13, upper panel **b**). The velocity shear profiles (Figures 2.15 and 2.16, panels **b**), present a similar limitation of the model at 24S. Because the velocity decays exponentially from the surface, the model was not able to reproduce the $\frac{\partial V}{\partial z}$ peak at approximately 420 m of depth.

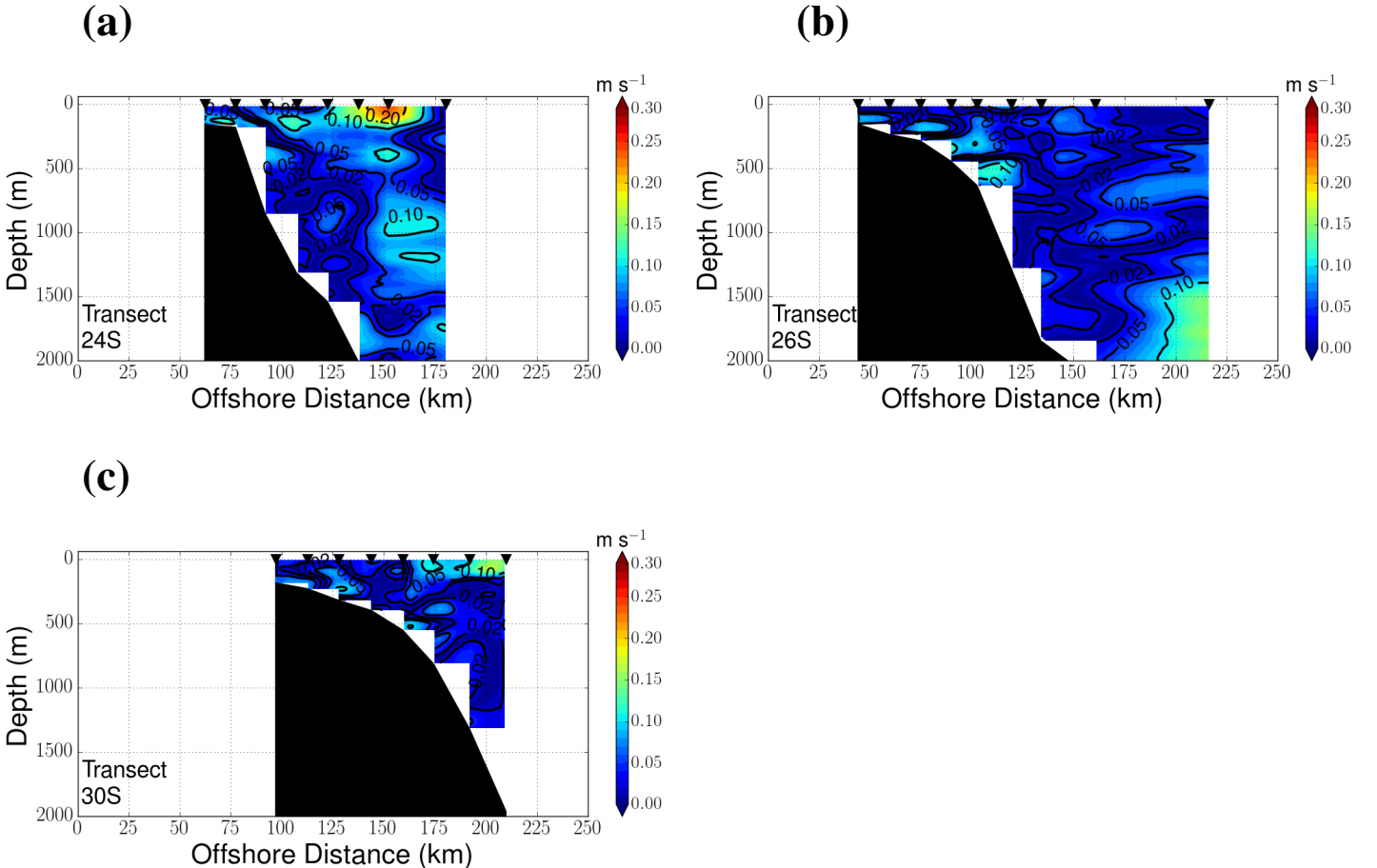


Figure 2.14: Absolute velocity difference distributions between the observed and the parametric model at transect (a) 24S, (b) 26S and (c) 30S. The black triangles indicate the locations of the CTD-LADCP profiles.

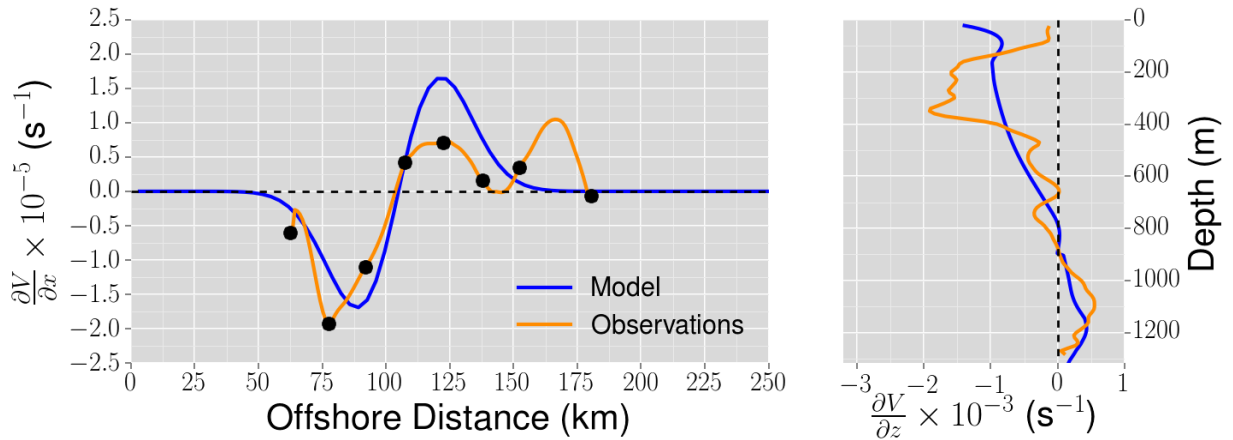
In contrast to the transects 24S and 26S, there is no northward flow at intermediate depths in the velocity measurements at transect 30S, which required us to change the parametric model in

order to better represent $V(x, z)$ (Equation 2.34). This model also had a good performance and well represented the position, dimensions, maximum velocities and volume transport of the BC.

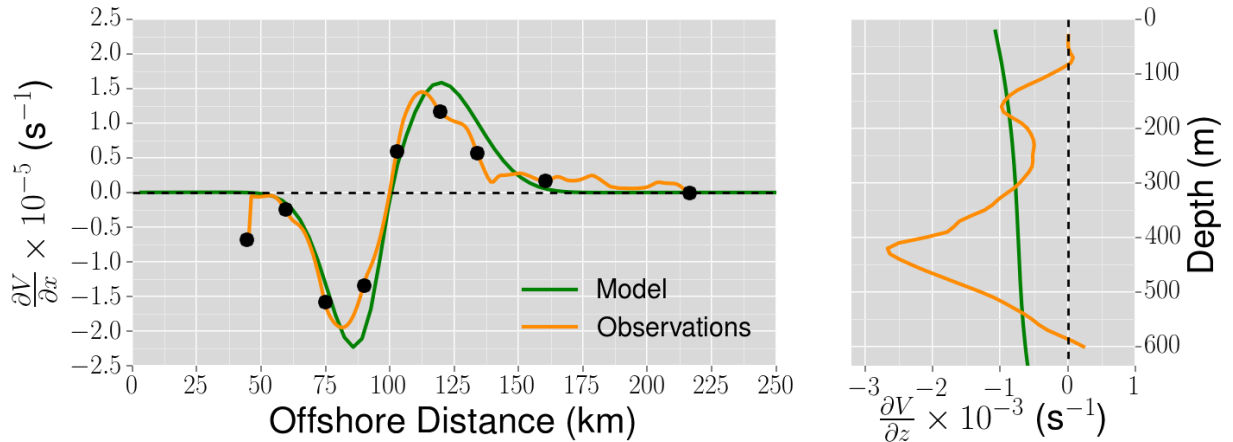
The BC is depicted extending down to 1000 m depth and is, at least, 100 km wide (Figure 2.13, panels **c**). The parametrized (observed) maximum velocities reach 0.45 m s^{-1} (0.45 m s^{-1}) and volume transport is approximately 10.67 Sv ($\sim 11 \text{ Sv}$). Likewise the other transects, high errors ($\sim 0.10 \text{ m s}^{-1}$) are located off the BC area (Figure 2.14, panel **c**). Again the primary limitation of the model is related to the $\frac{\partial V}{\partial z}$ (Figure 2.15, panel **c**). In fact, the model fails in reproducing the $\frac{\partial V}{\partial z}$ signal inversion at $\sim 100 \text{ m}$ due to the maximum observed velocity do not be located at the surface ($\sim 90 \text{ m}$), and its peak at $z \geq 450 \text{ m}$.

Despite the limitations of using analytic functions to describe the cross-sectional velocity distributions, we successfully build parametric models that yielded suitable representations of the general characteristics of the velocity observations. We must keep in mind that the BC system models were compared with direct velocity measurements, which comprises signals of movements at different spatial and temporal scales. In that sense, we should be aware that details will be missed and not expect perfect velocity representations.

(a)



(b)



(c)

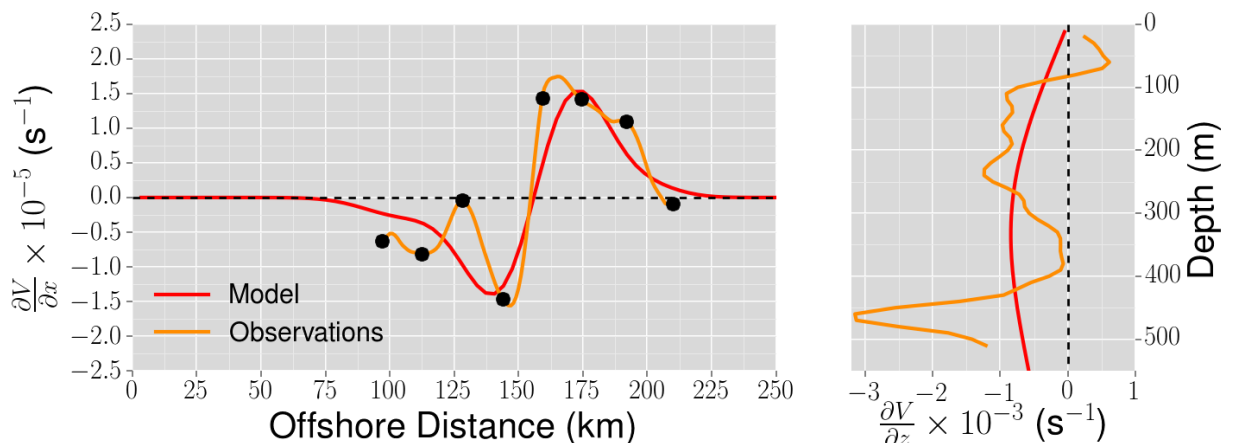
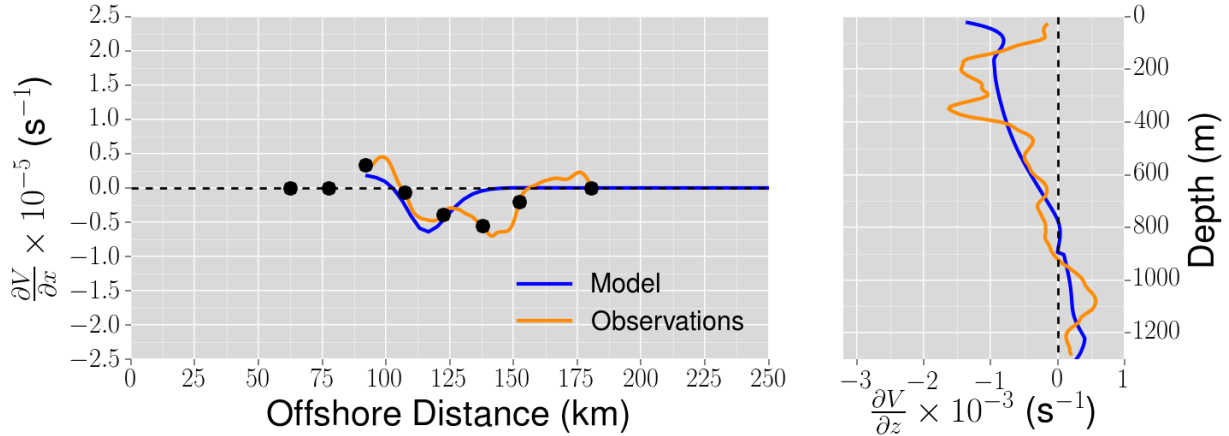


Figure 2.15: Profiles of the BC horizontal ($\frac{\partial V}{\partial x}$, left panels) and vertical ($\frac{\partial V}{\partial z}$, right panels) velocity shears at transect (a) 24S, (b) 26S and (c) 30S. The presented profiles are located at the BC velocity core. The black dots indicate the locations of the CTD-LADCP profiles.

(a)



(b)

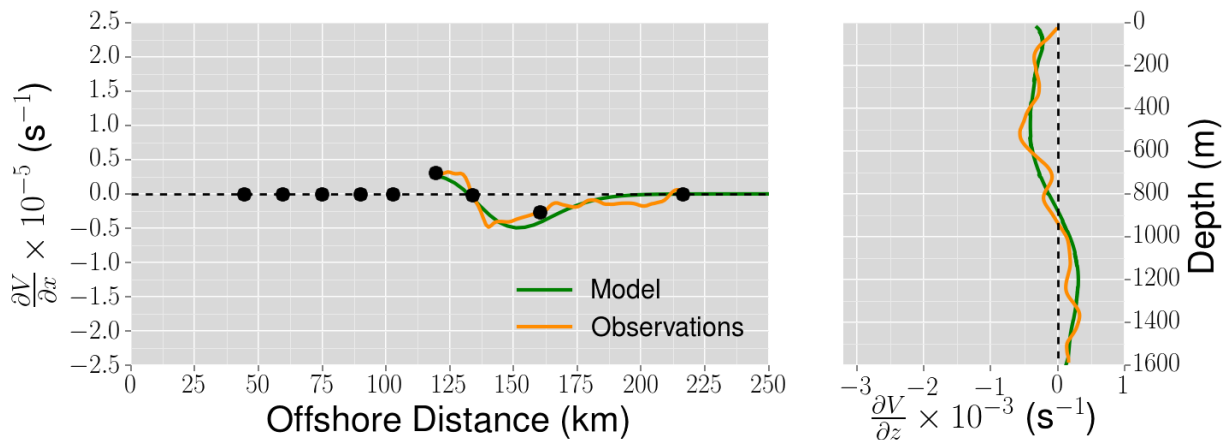


Figure 2.16: Profiles of the IWBC horizontal ($\frac{\partial V}{\partial x}$, left panels) and vertical ($\frac{\partial V}{\partial z}$, right panels) velocity shears at transect (a) 24S and (b) 26S. The presented profiles are located at the IWBC velocity core. The black dots indicate the locations of the CTD-LADCP profiles.

2.3.3 Necessary conditions for instability and idealized experiments

In Section 2.1, we pointed out that different studies showed the BC is indeed baroclinically and barotropically unstable along its path through the Santos Basin (23°S - 28°S), however there is no study that evaluated the effects of the mixed-instabilities in this region until now. Although, its expected both kinds of instabilities occur simultaneously due to the presence of horizontal and vertical velocity shears we tried to evaluate if our background states satisfy the necessary conditions for these instabilities to develop. To accomplish that, we discuss the conditions based on the cross-sectional distributions of the potential vorticity following [Chen \(1989\)](#) and [James \(1996\)](#). These authors computed the cross-sectional distribution of the potential vorticity for the Kuroshio Current.

The classic Ertel's theorem states, for a inviscid fluid, the total potential vorticity is expressed by

$$Q = -\frac{(f \vec{k} + \nabla \times \vec{V})}{\rho} \cdot \nabla \lambda, \quad (2.35)$$

where $\vec{f} \cdot \vec{k}$ is the planetary vorticity, $\nabla \times \vec{V}$ is the relative vorticity and $\lambda(p, \rho)$ is a scalar quantity that is conserved for each fluid element (i.e., $\frac{d\lambda}{dt} = 0$) (e. g., [Pedlosky, 1987](#)). Taking λ to be buoyancy, we can rewrite Q (Equation 2.35) as the sum of the basic potential vorticity (q) and the eddy potential vorticity (q'). The first is associated with the background states and the second with the perturbations. The expression for q is given by Equation 2.36.

$$q = \frac{\rho_0}{gB} [(f_0 + \frac{\partial V}{\partial x}) \frac{\partial B}{\partial z} - \frac{\partial B}{\partial x} \frac{\partial V}{\partial z}]. \quad (2.36)$$

[Pedlosky \(1964\)](#) showed that, in general, a necessary condition for mixed-instabilities occur is that $V \frac{\partial q}{\partial x}$ must be positive somewhere in the domain. In fact this condition is satisfied in the three background states built. Figure 2.17 clearly show the regions where $V \frac{\partial q}{\partial x} > 0$ in blueish colors.

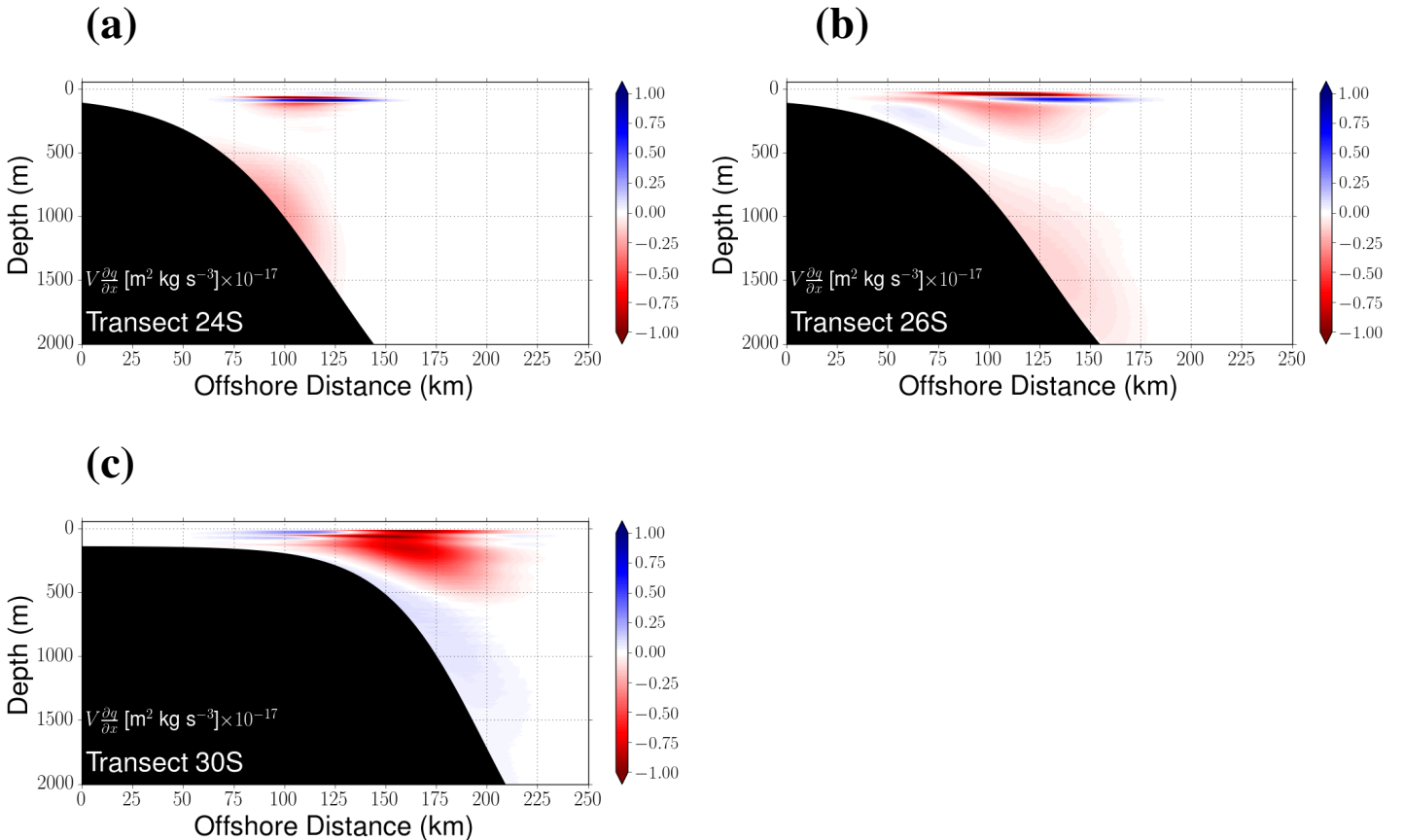


Figure 2.17: Product of the velocity V and the cross-sectional gradient of the basic potential vorticity ($\frac{\partial q}{\partial x}$) in the background state at transect (a) 24S, (b) 26S and (c) 30S.

Since our background states are expected to be unstable for both kinds of instabilities, and we wanted to evaluate what are the instability driving mechanisms and the effects of topography, we set six idealized experiments in order to better answer our guiding questions. Besides the experiments using the parametric models proposed for transects 24S, 26S and 30S we proposed three experiments without topography, or no slope steepness (24S_{nt}, 26S_{nt}, 30S_{nt}), and three experiments without topography and reduced horizontal velocity shear (24S_{bc}, 26S_{bc}, 30S_{bc}).

The set of experiments without topography (index _{nt}) were built with the intent to quantify the stabilizing, or destabilizing, effect of the topography in the mixed-instabilities. These experiments were built by altering the constants H_s and H_d from Equation 2.31. We set all experiments domain

with a constant depth of 1000 m mainly for two reasons. The first reason is that transects 24S and 26S have the BC system centred approximately over the 1000 m isobath. Secondly, we were able to keep a good vertical resolution of 200 vertical levels without distorting the velocity and increasing the computational time.

It is important to mention that keeping the original functions for $V(x, z)$ extrapolations of velocity and buoyancy fields under the original topography were done. However, our results show that no unreal new frontal regions were created and the perturbations were concentrated around the original systems (see Appendices A and B). Although in experiment 30S_{nt} the current is centred over \sim 600 m isobath, almost the entire BC was kept intact.

The experiments without topography and reduced horizontal velocity shear (index bc) were performed to reduce as much as possible the perturbations growth due to barotropic instability (e. g., [Pedlosky, 1987](#)). As mentioned before, it is desirable for $\frac{\partial \bar{\rho}(x, z)}{\partial x}$ and $V(x, z)$ to decay to zero at the lateral boundaries, therefore we were not able to simply eliminate the horizontal structure of the background velocity field. We bypassed this problem by increasing the currents horizontal length scale L_0 (i.e., width) and consequently reducing the horizontal velocity shear. In order to reduce the boundary effects we also increased the models domain in order to keep the original distance of the frontal regions from the lateral boundaries.

In the theoretical study of [Killworth \(1980\)](#), the author shows that for fluids with vertical and horizontal shears, under the QG theory, the type of instability is defined by two basic parameters; the ratio of L_0 to the first internal deformation radius $R_{d1}(\lambda_{kw})$, and the fractional depth of variation of the stratification (δ_{kw}). Likewise other western boundary currents (Gulf Stream and Kuroshio), the BC has a L_0 two to four times larger than the internal deformation radius between 23°S and 30°S and a $\delta_{kw} \ll 1$. At these limits, the author argues that one type of instability is easily isolated by changing one of the parameters because the mixed-instability just occurs in a small number of combinations of λ_{kw} and δ_{kw} . In other words, if we increase λ_{kw} the system will just allow baroclinic instability. In that sense, we altered some parameters of the parametric models to generate current systems with widths twice the size of the originals without altering the vertical velocity shears.

2.3.4 Model Performance

Before describing the stability properties of each experiment it is important to mention that we first tested the model performance. [James et al. \(1999\)](#) pointed out that two important aspects of the model should be tested before performing the numerical experiments. The first aspect is the model convergence to a solution, the second is the presence of an inconsistency in the buoyancy boundary conditions that could give rise to spurious growth rates, even in the absence of any forcing.

The model requires a truncation level N in order to make the instability problem numerically solvable. A fundamental problem of such spectral models is to determine N so that the truncated solution converges to the real one. [Xue and Mellor \(1993\)](#) showed that the model solutions converge for increasing N and the convergence tends to be faster at larger wavelengths perturbations. So the appropriate choice of N depends on the instability being studied ([James et al., 1999](#)). Based on the previous knowledge about the instability processes of the BC, we decided to test the model convergence for perturbations with wavelength between 10 km and 1000 km (10 km, 100 km, 200

km, 500 km, 1000 km) using the background states from the experiments 24S, 26S and 30S.

The model is set to give us the eigenvectors $u_{\lambda\nu}$, $v_{\lambda\nu}$ and $b_{\lambda\nu}$, and the eigenvalues σ . If the growth rates $-\sigma_i$, phase speeds c ($c = \frac{-\sigma_r}{\beta}$) and perturbations amplitudes [$\tilde{u}(x, \zeta)$, $\tilde{v}(x, \zeta)$ and $\tilde{b}(x, \zeta)$] change less than 5% between consecutive N , the model is assumed to have converged. For the fields of the perturbations amplitudes the 5% criteria refers to the RMS difference. The tested N varied from 20 to 46, resulting in the model convergence for $N = 38$ for all wavelengths and backgrounds tested. Based on this result we decided to set our model with $N = 40$ for all the experiments performed in this work.

The second aspect is intrinsically related to the topography and resolution of the model. Using a much more complicated topography profile, [James et al. \(1999\)](#) performed a motionless experiment (no kinetic and potential energy sources) to see if spurious growth rates are generated. They obtained small growth rates compared to the realistic experiments. So we did the same test for transects 24S, 26S and 30S. All the resulting growth rates are smaller than 10^{-3} day $^{-1}$, therefore they are at least one order of magnitude smaller than those obtained in the realistic experiments (see Section 2.3.5).

2.3.5 Stability properties and energy pathway

For each experiment, the instability modes were calculated for a range of wavelengths spanning 10–1000 km, then we analysed the stability properties of the most unstable mode (fastest growth rate). Additionally we discussed the relative importance of baroclinic and barotropic instabilities by comparing three important energy conversion terms: mean kinetic energy (MKE) to EKE, or Reynolds stress (RS); mean potential energy (MPE) to eddy potential energy (EPE), or horizontal heat flux (HHF); EPE to EKE, or vertical heat flux (VHF). These terms were calculated following [Xue and Mellor \(1993\)](#) and are presented in Equations 2.37–2.39.

$$RS = -\frac{Ro}{h}(\bar{uv}\frac{\partial V}{\partial x} + \bar{vw}\frac{\partial V}{\partial \zeta}) \quad (2.37)$$

$$HHF = [(\zeta - 1)\frac{\partial h}{\partial x}\frac{1}{h} - \frac{\partial B}{\partial x}(\frac{\partial B}{\partial \zeta})^{-1}]\bar{ub} \quad (2.38)$$

$$VHF = \bar{\omega b} + (\zeta - 1)\frac{1}{h}\frac{\partial h}{\partial x}\bar{ub}, \quad (2.39)$$

where the overbars represent the averaging over a wavelength in the y -direction. These terms represent the sources and sinks of eddy energies.

Basically, the baroclinic and barotropic instabilities respectively drain MPE and MKE from the basic state and transfer it to the perturbations or eddy field (e. g., [Pedlosky, 1987](#)). Therefore, we can relate the rates HHF and VHF to the baroclinic instability, and RS to the barotropic instability process. Moreover, it is important to mention that not all the energy released from the mean flow, through instability processes, is used to feed the growth of the perturbations in the same region. In [Chen et al. \(2014\)](#)'s study, the authors quantified how much MPE and MKE released from the mean large-scale circulation, at different regions of the globe, locally contribute to the perturbations growth (local instability). Using their approach and our perturbation fields, we refined the energy pathway by comparing the eddy energies change rates (HHF and RS) with the mean energies change rates (Equations 2.40 and 2.41).

$$\int_A [(\zeta - 1) \frac{\partial h}{\partial x} \frac{1}{h} - \frac{\partial B}{\partial x} (\frac{\partial B}{\partial \zeta})^{-1}] \overline{ub} \approx - \int_A -\frac{\partial \overline{ub}}{\partial x} B (\frac{\partial B}{\partial \zeta})^{-1} \quad (2.40)$$

Local baroclinic instability

$$\int_A -\frac{Ro}{h} (\overline{uv} \frac{\partial V}{\partial x} + \overline{v\omega} \frac{\partial V}{\partial \zeta}) \approx - \int_A -\frac{Ro}{h} (V \frac{\partial \overline{uv}}{\partial x} + V \frac{\partial \overline{v\omega}}{\partial \zeta}), \quad (2.41)$$

Local barotropic instability

where A is the transect area.

Due to the large number of experiments, we separated the discussion of the instability properties in four parts. In the first part, we compare the model results from the “realistic” experiments (24S, 26S and 30S). In the other parts we discuss the relative importance of the different processes in the linear instability problem at each transect by comparing the “realistic” experiment with the idealized ones ($_{nt}$ and $_{bc}$ indexes).

Experiments 24S, 26S and 30S

As expected, the BC system is indeed unstable at all the three transects locations. In Figure 2.18 we present the growth rates (panel **a**) and phase speeds (right panel textbfb) as functions of wavelength of the most unstable mode. In the experiment 24S the most unstable wave (140 km) has a growth rate of 0.12 day^{-1} , corresponding to an e-folding time scale (eT) of about 8 days. In the experiment 26S, the BC system presents a most unstable wave (120 km) with growth rate of 0.19 day^{-1} (eT~5 days). Further downstream, experiment 30S, the growth rates are significantly smaller than in the experiments 24S and 26S. The most unstable wave (130 km) has growth rate of 0.06 day^{-1} which corresponds to a eT of approximately 17 days.

The phase speeds of these perturbations are -0.19 , -0.24 and -0.26 m s^{-1} , for experiment 24S, 26S and 30S respectively. Therefore, the steering levels [depths at which phase speed = $V(x, z)$] are all within the BC domain. The steering levels, considering the vertical velocity profiles that cross the BC core, are approximately 207, 302 and 339 m in experiments 24S, 26S and 30S respectively.

Two important aspects of the curves presented in Figure 2.18 must be highlighted. The first aspect is the fact that the BC system becomes more unstable as it flows southwestward to the north of the Santos Bifurcation ($\sim 27^\circ\text{S}$). In contrast, as the current crosses the bifurcation the current becomes more stable. This behaviour was also observed in the baroclinic instability analysis carried out by *Rocha et al.* (2014), however their findings are directly related to the fact that the highest vertical velocity shear is located at $\sim 25^\circ\text{S}$ and the smallest at $\sim 28^\circ\text{S}$. In the present study the vertical velocity shear is higher in the experiment 24S (Figure 2.15), so we associated this fact with the barotropic instability process.

The second aspect is that the BC to the south of the Santos Bifurcation is unstable for a fewer number of perturbations than the system to the north of the bifurcation. This was also observed by *Rocha et al.* (2014) and *Fernandes et al.* (2009). The latter work numerical simulations showed that the 430 km-long unstable waves has their amplitude decreased as the BC flows to the south of 25°S , therefore the BC became stable for 430 km-long waves. The background state of the transect 30S

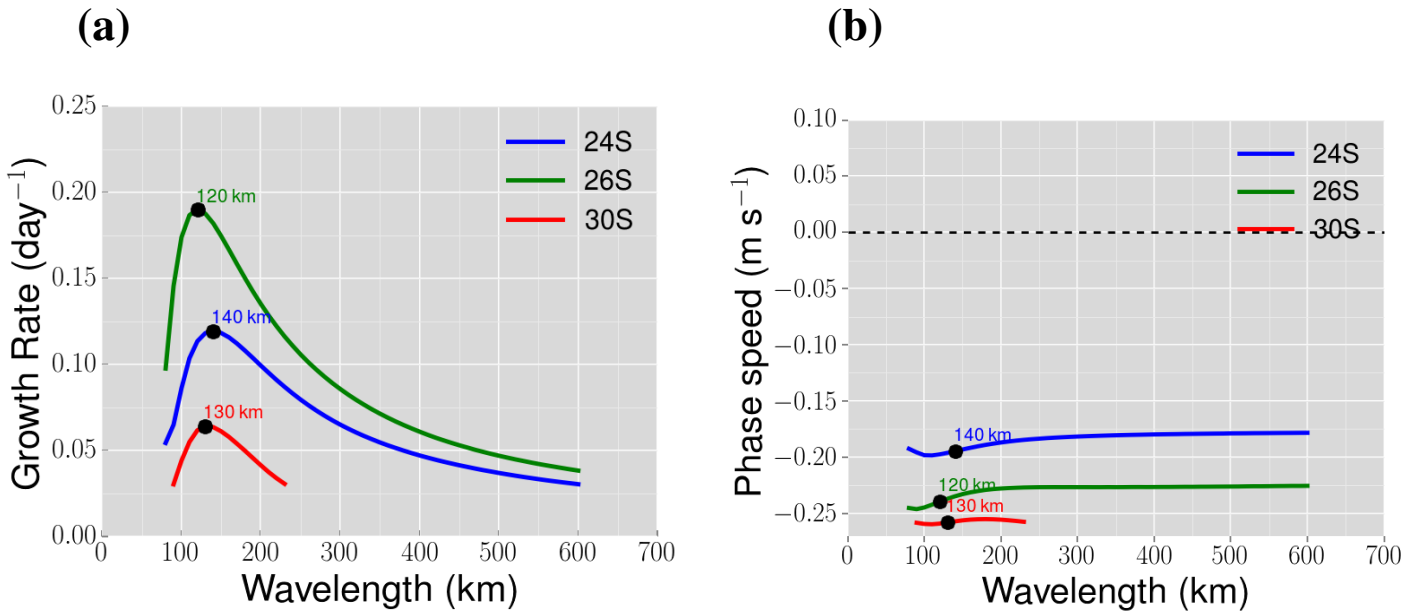


Figure 2.18: (a) Growth rates and (b) phase speeds of the most unstable mode from the experiments 24S, 26S and 30S. The black dots indicate the wavelength of the most unstable wave of each curve.

is unstable for perturbations with wavelengths between 90 and 230 km. *Rocha et al. (2014)* also called attention to the possibility the baroclinic vorticity waves to the south of the bifurcation be shorter than in the northern part of the study region, however we did not find clear evidence of similar characteristic in our experiments.

Figures 2.19, 2.20 and 2.21 present the amplitudes of the most unstable perturbations and the resulting energy conversion terms from each experiment. Note that the amplitudes and energy conversion terms are dimensionalized. In order to estimate how much energy from the background state is transferred to eddy motions, we had to assume a horizontal velocity perturbation scale. We considered $u_0 = 0.1 \text{ m s}^{-1}$, following *Rocha et al. (2014)*.

A noticeable characteristic of all “realistic” experiments is the confinement of the perturbations in the upper 400 m of water column around the BC core, which is consistent with the fact that the BC presents a more vigorous mesoscale activity than the IWBC (e.g., *Silveira et al., 2008; Rocha et al., 2014; Biló et al., 2014*), moreover this also explain the southward phase speeds. *James et al. (1999)* associated the changes of phase speeds of the most unstable waves in the Kuroshio Current with the background velocity. They argued that, because the phase speeds changed, in percentile, a similar amount than the background velocity in different experiments, the perturbation advection by the mean current is the primary reason for the observed changes. Using the results of the experiment 24S as reference, the wavelength of the most unstable waves changed ~8% (16%) and the mean velocity, in the area where the perturbations are concentrated, changed ~30% (40%) when compared with the same parameters from experiment 26S (30S). Since the correspondent phase speed is 26% (36%) higher than the phase speed obtained in experiment 24S, the perturbation advection seems to be the primary reason for the differences in the phase propagation.

From b panels in Figures 2.19-2.21, it is clear that the current system is unstable for baroclinic and barotropic instabilities ($\text{HHF}>0$, $\text{RS}>0$), as expected from the potential vorticity analysis. Moreover, the baroclinic instability drains, in general, more energy from the background state than the barotropic

instability (HHF>RS). In order to quantify the relative importance of each type of instability we integrated the energy conversion terms over the transect area. To better illustrate the energy pathways involved in the proposed mixed-instability problem, we also built diagrams containing the integrated values of HHF, VHF and RS, and their efficiency in draining energy from the background state (Figure 2.22). These energy diagrams are simplified versions of the energy pathways described by *Chen et al.* (2014) for different regions of the global ocean.

The integration of the energy terms from experiment 24S (Figure 2.22, panel **a**) show that the energy drained from the background state through barotropic instability (0.14 kW m^{-1}) is approximately 14% of the energy drained through baroclinic instability (1.03 kW m^{-1}). Moreover, the VHF accounts for 57% (0.59 kW m^{-1}) of the HHF. Note that the instability processes in experiment 24S are predominantly local, since approximately 70% of the MKE are transformed in EKE and HHF corresponds to only an increase of $\sim 27\%$ of the MPE released energy from a non-local source.

Although the energy diagram of experiment 26S (Figure 2.22, panel **b**) presents similar values for HHF (0.98 kW m^{-1}) and VHF (0.58 kW m^{-1}) to the terms from experiment 24S, the RS (0.38 kW m^{-1}) term is ~ 2.6 times bigger. This implies that the most unstable wave is theoretically more efficient in draining energy from the background state through barotropic instability. However this difference is due the non-locality of the barotropic instability process. Nevertheless more energy are transformed in EKE due to barotropic instability at 26°S . This result is consistent with the drifter analysis of *Oliveira et al.* (2009). The authors found that the RS at the surface is higher at $\sim 26^\circ\text{S}$ than at 24°S and 30°S .

To the south of the bifurcation (experiment 30S) the BC becomes larger and thicker, which means the vertical and horizontal velocity shears decrease as it flows poleward (e.g., *Müller et al.*, 1998). As consequence the BC becomes more stable and less energy is drained from the background state and transferred to the eddy field (Figure 2.22, panel **c**). The energy terms HHF, VHF and RS are 0.60, 0.43 and 0.07 kW m^{-1} , respectively and they are significantly smaller than those obtained from the other “realistic” experiments. Another interesting characteristic is that the barotropic instability accounts for only $\sim 11\%$ of the energy transferred through baroclinic instability. Most of the energy, $\sim 90\%$ (64%) drained from the MPE (MKE) are used to support local growth.

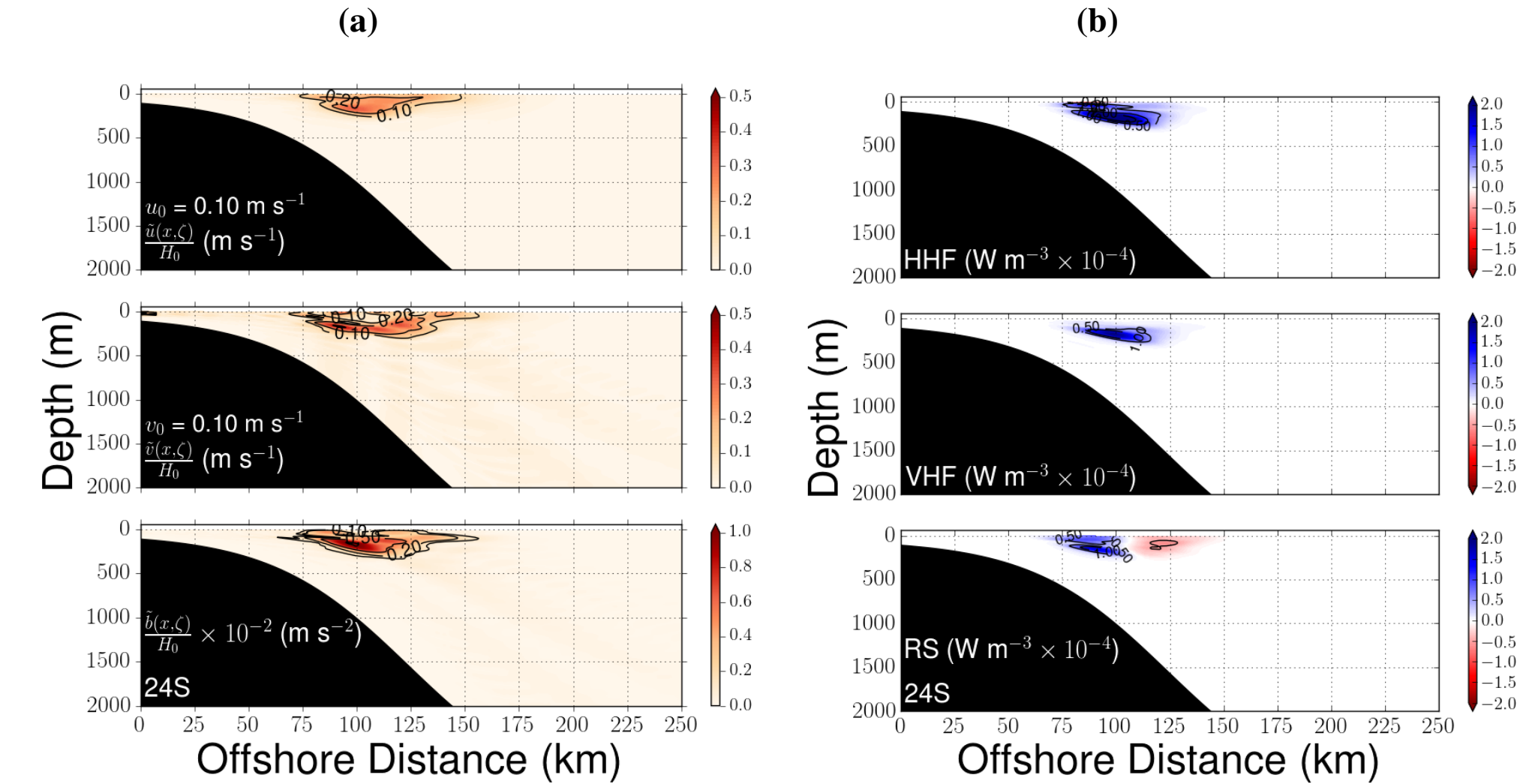


Figure 2.19: **(a)** Amplitudes of the perturbations fields ($\frac{\tilde{u}(x,\zeta)}{H_0}$, $\frac{\tilde{v}(x,\zeta)}{H_0}$ and $\frac{\tilde{b}(x,\zeta)}{H_0}$) and **(b)** energy conversion terms HHF, VHF and RS from experiment 24S.

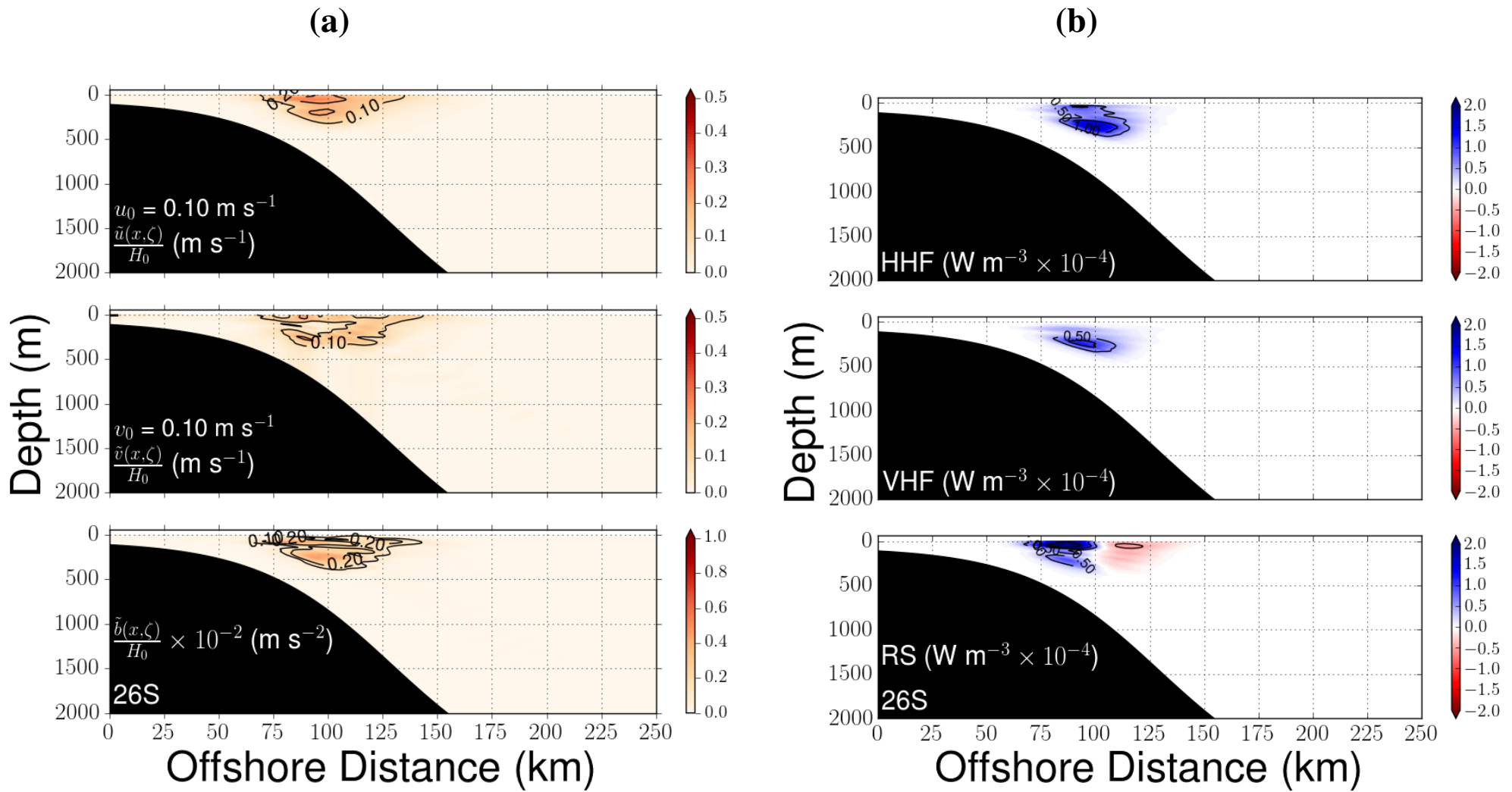


Figure 2.20: **(a)** Amplitudes of the perturbations fields ($\frac{\tilde{u}(x,\zeta)}{H_0}$, $\frac{\tilde{v}(x,\zeta)}{H_0}$ and $\frac{\tilde{b}(x,\zeta)}{H_0}$) and **(b)** energy conversion terms HHF, VHF and RS from experiment 26S.

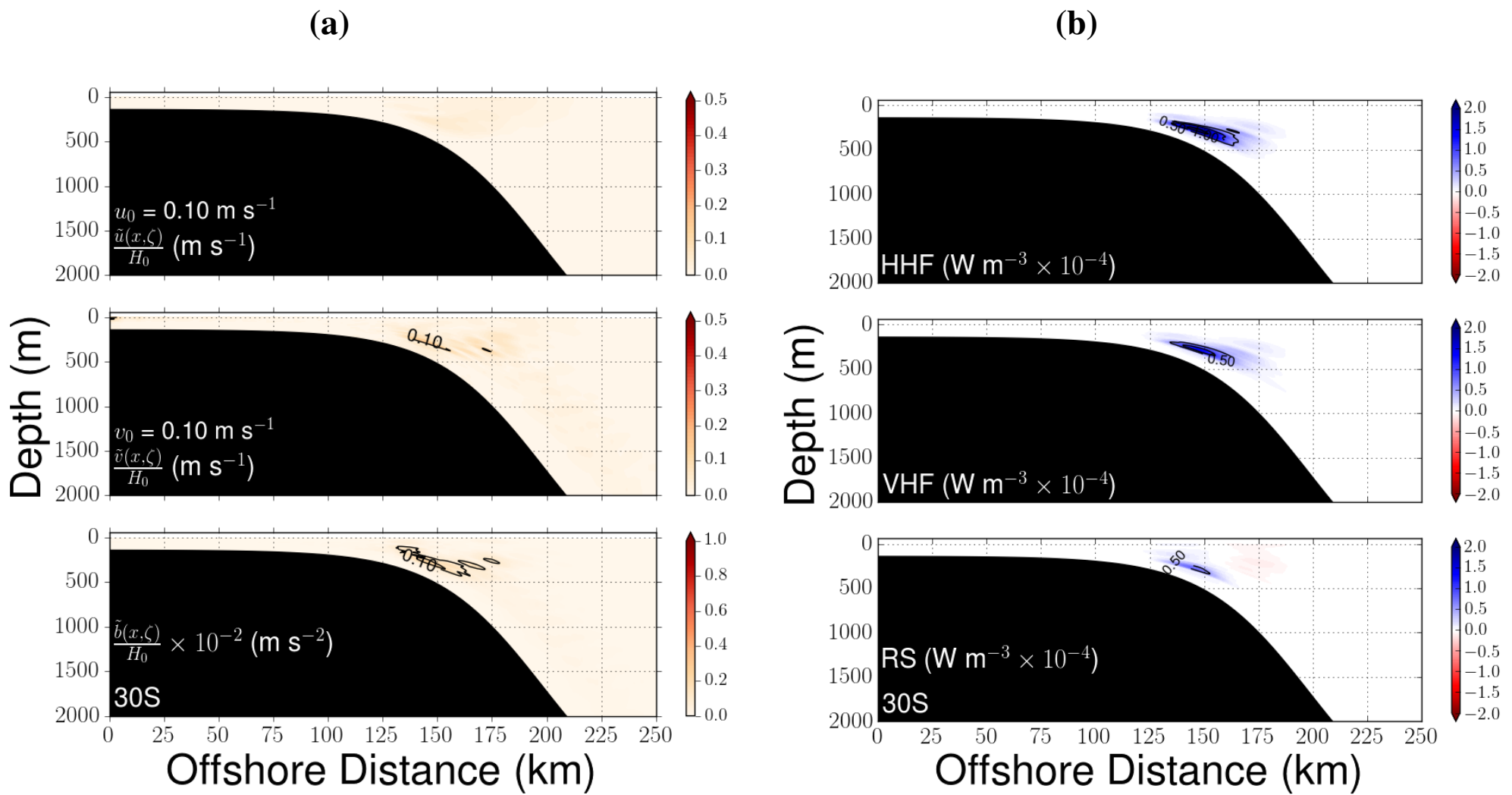


Figure 2.21: **(a)** Amplitudes of the perturbations fields ($\frac{\tilde{u}(x,\zeta)}{H_0}$, $\frac{\tilde{v}(x,\zeta)}{H_0}$ and $\frac{\tilde{b}(x,\zeta)}{H_0}$) and **(b)** energy conversion terms HHF, VHF and RS from experiment 30S.

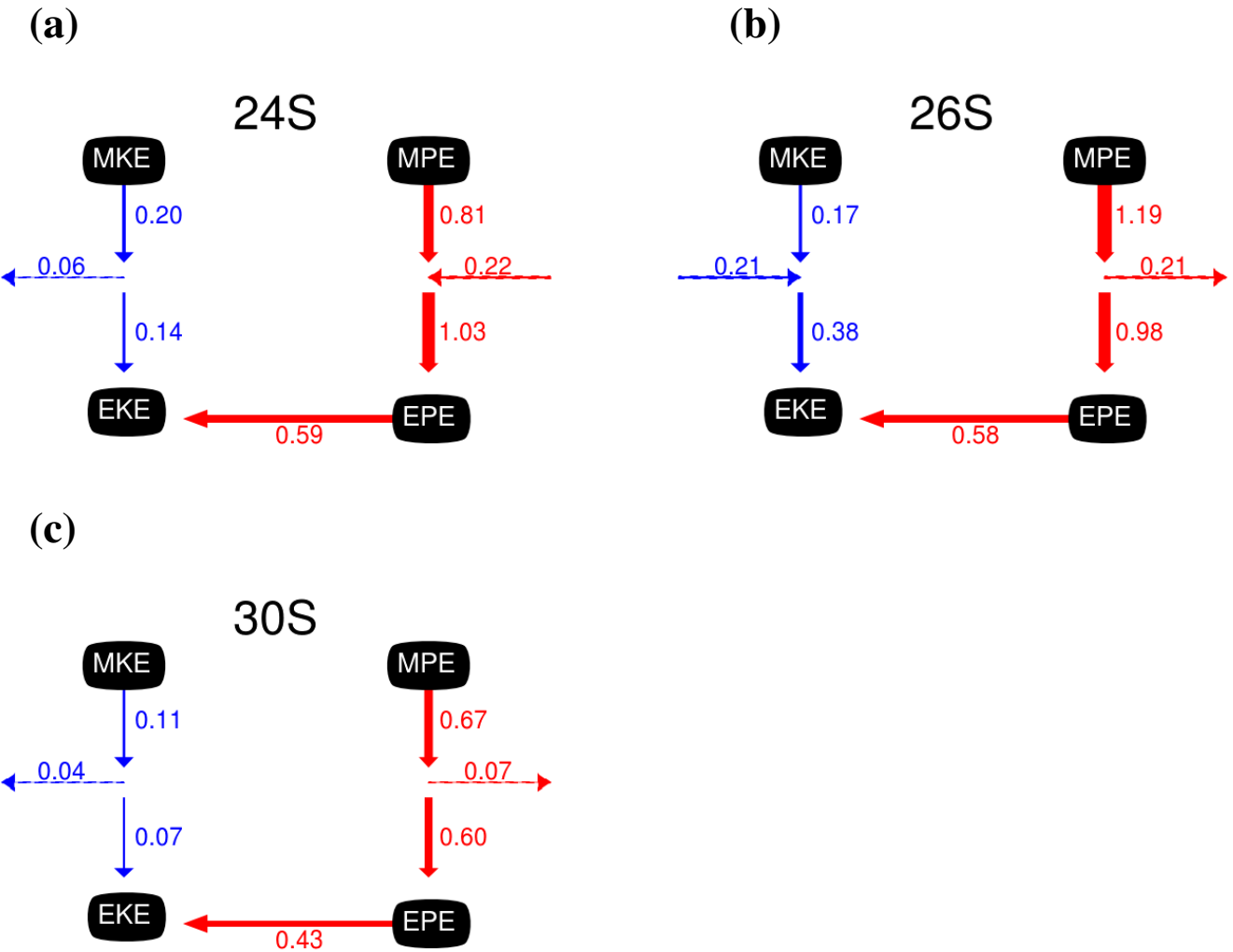


Figure 2.22: Energy flux diagrams in 10^3 W m^{-1} (kW m^{-1}) from experiment (a) 24S, (b) 26S and (c) 30S. The red arrows with solid tail represent the baroclinic energy conversions terms and the blue arrows with solid tail the barotropic energy conversion terms. The arrows with dashed tail indicate how much energy are related with non-local instability processes.

Idealized experiments $24S_{nt}$ and $24S_{bc}$

After discussing the differences between the “realistic” experiments we tried to isolate the topographic and barotropic instability effects by using the idealized experiments and comparing it to the “realistic” ones. The upper panels of Figure 2.23 present the growth rates and the phase speeds of the experiments 24S, $24S_{nt}$ and $24S_{bc}$. At a first glance, a significant impact of the topography and the horizontal velocity shear on the stability properties can be inferred from the different dispersion curves.

The flat topography ($24S_{nt}$) was responsible for an increase of 25% in the maximum growth rate (0.15 day^{-1} , or $eT \sim 6 \text{ days}$). In opposition to that, when the width of the currents are doubled ($24S_{bc}$) the system becomes more stable and the 190 km-long waves are the most unstable ones with maximum growth rates of 0.06 day^{-1} ($eT \sim 16 \text{ days}$). In both idealized experiments the phase speeds are positive and very small ($\sim 0.05 \text{ m s}^{-1}$), which correspond steering levels located close to the BC-IWBC interface ($\sim 500 \text{ m}$). Therefore, the idealized background configurations with significant decreased stiffness favoured longer period oscillations ($T = 8.53, 20.83$ and 44.98 days for 24S, $24S_{nt}$ and $24S_{bc}$ respectively), which corroborate [James et al. \(1999\)](#) results for the Kuroshio behaviour.

In Section 2.1 we mentioned that in the literature the most unstable waves that emerge from baroclinic instability analysis and using QG theory, are 200-400 km-long, quasi-stationary (small northward phase propagation) and growth rates of 0.03-0.06 day⁻¹ at ~23°S ([Silveira et al., 2008](#); [Rocha et al., 2014](#)). In that sense our stability analysis indicates that quasi-stationary waves might be generated by the usage of constant topography or very low topography steepness. [Silveira et al. \(2008\)](#) and [Rocha et al. \(2014\)](#) indeed scaled the topography steepness by $Ro = 0.10$, which allowed the longer period perturbations, of ~88.73 and ~51.31 days respectively, that extend to deeper regions of the domain to be the most unstable ones. Nevertheless [Garfield \(1990\)](#) reported few events when such waves were observed at Cape Frio relative to shorter faster growing propagating, which suggests that a different conformation of the BC system may favour the growth of these oscillations. It is worth to mention that the transect 24S is placed at the vicinities of the Santos Plateau, therefore the topographic steepness between the 2000 and 3000 m isobaths is very smooth and may provide the adequate conditions for the quasi-standing meander growth happen when the BC is displaced offshore.

Similarly to the “realistic” experiments, we integrated the energy conversion terms over the transect area. The experiment 24S_{nt} yielded a HHF of approximately 0.74 kW m⁻¹, VHF~0.03 kW m⁻¹ and RS of approximately 0.37 kW m⁻¹. These values suggest that, in the absence of topography, the barotropic instability becomes more important for the instability process (50%) when compared with the case with topography (14%).

Interestingly the same energetic analysis of experiment 24S_{bc} revealed that we were able to reduce significantly the effects of the horizontal velocity shear and “isolate” the most baroclinic unstable waves. The integration yielded a HHF of 0.29 kW m⁻¹, VHF~0.01 kW m⁻¹ and RS of 0.01 kW m⁻¹. As expected this most stable scenario has perturbations with a low efficiency in draining energy from the background state and the barotropic instability corresponds to a small fraction (~3%) of the instability process.

Idealized experiments 26S_{nt} and 26S_{bc}

The idealized experiments at transect 26S provided interesting insights about the instabilities in the region. In agreement with the idealized experiments 24S_{nt} and 24S_{bc}, when the topography is set to be constant (26_{nt}) the most unstable wave (130 km) presents a growth rate (0.21 day⁻¹, or eT~5 days) approximately 11% higher than in the “realistic” experiment (26S). Moreover, the reduced horizontal velocity shear (26_{bc}) yielded longer unstable waves (max. of 300 km) with growth rates (0.04 day⁻¹, or eT of 25 days) significantly smaller than in the other experiments (Figure 2.23, middle panel **a**).

Note that the phase velocities (-0.24 and -0.19 m s⁻¹) did not change much (Figure 2.23, middle panel **b**) and the steering levels remained around 300 m. As expected the no topography scenario decreased the stiffness and favoured longer period waves to develop with 5.78, 6.27 and 18.27 days for experiments 26S, 26S_{nt} and 26S_{bc} respectively. The latter value is consistent with period of approximately 16.92 days found by [Rocha et al. \(2014\)](#) at 25.5°S. Additionally, if we compare the results from the experiments 26S and 26S_{nt} we can conclude that no large differences were found, which might be related to the fact that the BC be placed over a smoother topography than at 24S, and the IWBC be offshore displaced due to the topographic profile.

The integration of energy conversion terms from experiment 26S_{nt} (26S_{bc}) show a HHF approxi-

mately 0.55 kW m^{-1} (0.91 kW m^{-1}), VHF $\sim 0.02 \text{ kW m}^{-1}$ (0.04 kW m^{-1}) and a RS of 0.44 kW m^{-1} (0.02 kW m^{-1}). In that sense a similar scenario of experiments $24S_{nt}$ and $24S_{bc}$ is observed for experiments $26S_{nt}$ and $26S_{bc}$. Again in the experiment nt the barotropic instability becomes more important for the instability process (80%) and was considerably reduced in the experiment $26S_{bc}$ ($\frac{\text{RS}}{\text{HHF}} = 0.02$).

Idealized experiments $30S_{nt}$ and $30S_{bc}$

Finally, the idealized experiments $30S_{nt}$ and $30S_{bc}$ presented the most unstable waves with growth rates of 0.10 day^{-1} ($eT = 10 \text{ days}$) and 0.02 day^{-1} ($eT = 50 \text{ days}$), respectively. Again we were able to observe the stabilizing effect of the topography and the decreasing of the growth rates when the horizontal velocity shear is reduced. The phase speeds of the most unstable waves are -0.23 m s^{-1} , so the steering level increased in approximately 20 m (Figure 2.23, lower panels).

Although the effects on growth rates of topography and horizontal velocity shear seem to be similar to the north and south of the Santos Bifurcation, the instabilities contributions change radically from the idealized experiments to the north of the bifurcation. The term HHF from $30S_{nt}$ (0.33 kW m^{-1}) decreased in 50%, however in experiment $30S_{bc}$ HHF increased significantly and reached 1.91 kW m^{-1} , due to the BC's large horizontal dimensions. Again, in contrast to the experiments $24S_{nt}$ and $26S_{nt}$, the RS term from $30S_{nt}$ decreased (0.01 kW m^{-1}) and is approximately only 3% of the HHF. This relative loss of importance was reported by [Xue and Mellor \(1993\)](#) when experiments, of the Gulf Stream at the South Atlantic Bight, with topography and flat bottom were compared. The VHF terms are 0.01 and 0.09 kW m^{-1} in experiments $30S_{nt}$ and $30S_{bc}$, respectively.

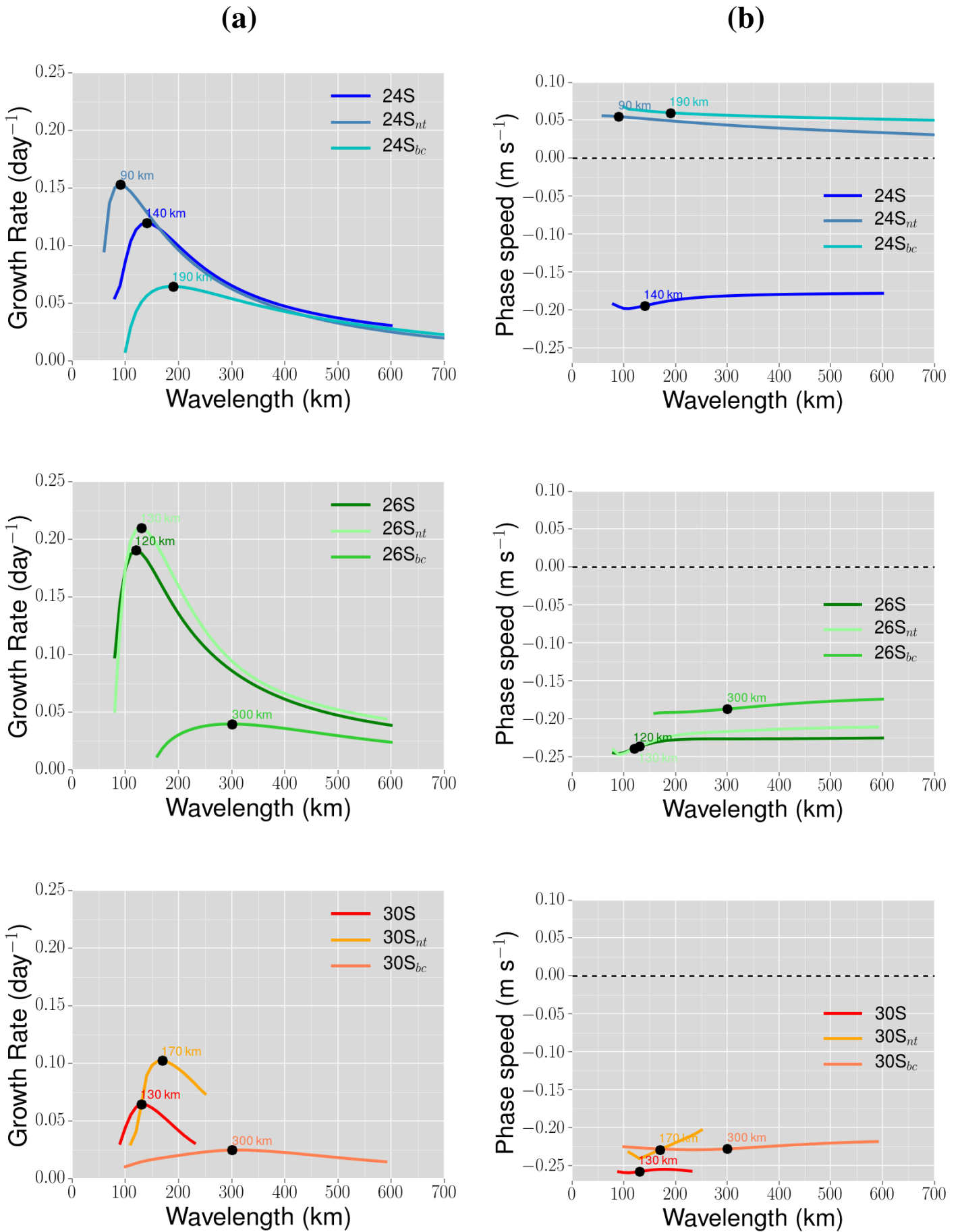


Figure 2.23: (a) Growth rates and (b) phase speeds of the most unstable mode from the numerical experiments at transect 24S (upper panels), 26S (middle panels) and 30S (lower panels). The black dots indicate the wavelength of the most unstable wave of each curve.

2.4 Summary and conclusions

Here we studied the BC meandering activity between 24°S and 30°S from the observational and numerical perspectives. The mixed-instability properties and its relation with the downstream changes of the BC system were addressed based on the description of a set of quasi-synoptic transects and the application of a PE frontal instability model, linearized around a background state chosen based on direct velocity observations.

The quasi-synoptic velocity observations revealed that the BC is ~400-500 m deep, although can reach deeper regions depending on its energetic state, to the north of the Santos Bifurcation (~27°S) and extends down to 1000 m to the south of it. We estimated that the BC receives at least 7 Sv at intermediate depths from the Santos Bifurcation, which drastically alters the velocity patterns and eddies characteristics as it flows poleward.

The background states correspond to analytical functions (parametric models) that describe the observed cross-sectional velocity distribution of the BC system at different latitudes. In that sense, we proposed two different set of analytic functions that described satisfactorily the general aspects of the BC system to the north and south of the Santos Bifurcation. It is important to mention that this work is not the first study to do so. *Schmidt et al. (2007)* were the first authors to propose a sectional parametric model for the BC system, however their model is restricted to the BC between 20°S and 24°S. We generalized their model and proposed functions that can easily be adapted to represent the BC at different latitudes. We then performed different numerical experiments in order to answer the following guiding questions. Table 2.4 summarizes the main results from the numerical experiments. As we stated in Section 2.1, we aimed to answer three questions that guided this work. The questions and our answers are:

(1) What are the differences between the instabilities to the north and to the south of the Santos Bifurcation ? Our experiments 24S, 26S and 30S show that the BC system is more unstable ($0.10 < -\sigma_i < 0.20 \text{ day}^{-1}$) and the instability waves propagate phase downstream with slightly smaller velocities ($c < 0.26 \text{ m s}^{-1}$) north of the Santos Bifurcation (23°S-27°S). This is consistent with the satellite imagery from *Garfield (1990)* and the numerical simulations from *Campos et al. (2000)* and *Fernandes et al. (2009)*. Moreover, the barotropic instability seems to be more efficient in draining energy from the background state at 23°S-27°S, corroborating *Oliveira et al. (2009)* results.

These changes in the stability properties and energetics of the perturbations are also in agreement with the meanders characteristics observed in the quasi-synoptic data set. Since the BC meandering activity is more independent from the IWBC than the upper 500 m flow is from the intermediate one at 28°S-30°S, the meanders can grow faster and project themselves over the continental shelf to the north of the bifurcation.

(2) What are the instability driving mechanisms ? In the scope of the temporal linear instability theory, our results corroborate the baroclinic instability analysis from *Silveira et al. (2008)* and *Rocha et al. (2014)*. These authors showed that the eigenstructures of the most unstable mode resembles the eigenstructures of the primary variability modes from currentmeter mooring lines, indicating that the baroclinic instability is the main cause of the mesoscale activity in the region. We found that the baroclinic instability is the primary mechanism for the transference of mean-to-eddy energy (HHF>RS, Table 2.4).

Despite that, the growth rates from experiments 24S, 26S and 30S are at least twice the magnitude of those found by *Silveira et al.* (2008) and *Rocha et al.* (2014). The answer seems to rely on the horizontal velocity shear (barotropic instability). From a first inspection of Table 2.4 we can conclude that higher growth rates are related to higher ratios $\frac{RS}{HHF}$. When the baroclinic instability was “isolated” the wavelengths and growth rates became more comparable to their findings. Therefore our numerical experiments suggests that barotropic instability has a significant impact on the instability process in the study region.

(3) What are the effects of topography changes ? From the experiments performed in this work, it is not clear the real impact of the topography differences in the instability process. Nevertheless our experiments without topography provided us interesting insights about the presence of it in the analysis. In general the topography profiles have a stabilizing effect, however the BC current instability have different response to the absence of topography to the north and to the south of the bifurcation. The ratio $\frac{RS}{HHF}$ increased when the topography is flat to the north of the bifurcation (experiments 24S_{nt} and 26S_{nt}). In addition we must stress that the BC flows over the continental slope with a high steepness, therefore the usage of QG models is very limited and it may be not adequate for the region.

Other observable topographic effect relies on the difference in the results from experiments 24S_{nt} and 26S_{nt} when compared to the experiments 24S and 26S respectively. The flat bottom experiment 26_{nt} does not comprise drastically changes as the 24S_{nt}, which suggests that the gentler continental slope at 26°S constrains less the BC meandering.

Table 2.4: Stability properties and energy conversion terms HHF, VHF, RS integrated over the transect area of the different numerical experiments. The boldfaced numbers indicate the properties of the “realistic” experiments.

Properties	24S	24S _{nt}	24S _{bc}	26S	26S _{nt}	26S _{bc}	30S	30S _{nt}	30S _{bc}
Wavelength (km)	140	90	190	120	130	300	130	170	300
Growth rate (day ⁻¹)	0.12	0.15	0.06	0.19	0.21	0.04	0.06	0.10	0.02
Phase speed (m s ⁻¹)	-0.19	0.05	0.05	-0.24	-0.24	-0.19	-0.26	-0.23	-0.23
Period (days)	8.53	20.83	44.98	5.78	6.27	18.27	8.78	8.55	15.10
HHF (kW m ⁻¹)	1.03	0.74	0.29	0.98	0.55	0.91	0.60	0.33	1.91
$\frac{RS}{HHF}$	0.14	0.50	0.03	0.39	0.80	0.02	0.11	0.03	0.005
$\frac{VHF}{HHF}$	0.57	0.04	0.03	0.59	0.04	0.04	0.72	0.03	0.05

This study combined observations with numerical modelling to expand our knowledge about the BC meandering characteristics and dynamics between 23°S and 30°S. We truly believe that our analysis provided important information about the BC system downstream changes and its relations with the eddy formation processes by evaluating the linear instability characteristics and energetics. Although PE models outputs may be difficult to interpret, we were able to perform different experiments in order to isolate the dynamics of each process and get useful insights about it.

Additional investigation has to be done towards the understanding of the processes involved in the BC eddy motion. Particularly to this study, the lack of information on the BC dynamics did not allowed us to quantitative evaluate if the linear instability reasonably predicts the real features present in the BC meandering activity. Another open question is how much our transects are close to the mean

scenario of the BC system. Unfortunately, the available observations are few and sparse in space and time. We are also aware that the full instability problem cannot be accounted for by linear models and predictions of eddy development and propagation should be investigated from observations and more complex models (e. g., *Ni*, 1996; *Flierl*, 1999; *Oliveira et al.*, 2009; *Chen et al.*, 2014).

Chapter 3

The Brazil Current cyclonic meandering at 27°S-31°S: water mass composition, vertical structure, surface signature and formation frequency

Abstract

At the vicinities of the Cape Santa Marta (28°S), Brazil Current (BC) cyclonic meanders have been reported through sea surface temperature (SST) satellite images as recurrent features. Because these eddies were little explored in the literature, basic characteristics as their full velocity structure and recurrence were unknown. Here we use a range of observations to provide an overview of such features as well as the relations between its velocity patterns, the water properties (temperature, salinity, nutrients), chlorophyll-a distribution and the BC variability. Top-bottom quasi-synoptic velocity measurements depicted cyclonic meanders over the continental slope with diameters larger than 100 km and vertically extending to approximately 1500 m depth. Moreover, the observed eddies seems to trap and recirculate a small portion (~1.5 to 4 Sv) of the BC main flow (-13.16 to -17.89 Sv), which is consisted of TW, SACW, AAIW and UCDW. Additionally, we presented observational evidence that the meanders actively influence the transport of nutrients rich shelf waters to the open ocean enhancing the primary productivity at the photic zone over the continental slope. Satellite imagery show that these cyclones occur 5-6 times per year and are generally associated with wave-like perturbations on the flow with mean wavelength of ~219 km. Finally, Empirical Orthogonal Functions (EOF) analysis were computed from the World Ocean Circulation Experiment (WOCE) array of mooring lines (*Hogg et al., 1999*) and showed that more than half of the along-isobath velocity variance on the continental slope is explained by the BC mesoscale activity.

Keywords: Brazil Current variability, Cape Santa Marta, mesoscale activity, shelf-open ocean exchanges.

3.1 Introduction

The Brazil Current (BC) experiences strong mesoscale activity from its genesis site ($\sim 15^{\circ}\text{S}$) to the Brazil-Malvinas confluence ($\sim 39^{\circ}\text{S}$) over the continental shelf break and slope (Signorini, 1978; Leg-eckis and Gordon, 1982; Garfield, 1990; Campos et al., 1995; Oliveira et al., 2009; Soutelino et al., 2013). At the vicinities of the Cape Santa Marta (28°S), BC cyclonic meanders and eddies with approximately 100 km of diameter have been reported through sea surface temperature (SST) satellite images as recurrent features related to vorticity waves which propagate phase downstream (e. g., Garfield, 1990; Campos et al., 1996). Because these eddies were little explored in the literature, basic characteristics, such as the recurrence of such features remains unknown.

Geostrophic computations (Zemba, 1991), Lagrangian float trajectories (Boebel et al., 1999) and currentmeters mooring lines (Müller et al., 1998) show that the BC vertically thickens as it crosses the latitudes of $\sim 27^{\circ}\text{S}$. The thickening is related to the incorporation of the Antarctic Intermediate Water (AAIW) flow between 500 m and 1500 m of depth, over the continental slope to the BC poleward flow, known as the southern branch of the Santos Bifurcation. The Müller et al. (1998) and Rocha et al. (2014) moored currentmeters statistical analysis showed that the velocity standard deviations of the intermediate flow are comparable to the north and south of this feature. However, it is almost half of the standard deviations in the upper 500 m, which suggests less variability deeper than 500 m. It is not clear yet how dynamically coupled the intermediate flow is with the BC above it and how would the velocity pattern at such depths be during a BC cyclonic meander event.

Here we describe some basic characteristics of the cyclonic meanders near 28°S and provide observational evidence of its role in shelf-slope mass exchanges. We do that by describing the top-bottom velocity patterns of the BC during two distinct cyclonic meanders events and associating it with the water masses; surface temperature, salinity, nutrients (silicate, ammonium, nitrate, phosphate) and chlorophyll-a distributions. To accomplish this task, we used two quasi-synoptic data sets, an array of four moorings and satellite imagery (Figure 3.1).

The first quasi-synoptic data set is comprised by three transects of oceanographic stations obtained in November of 2013 (11/18 - 11/23). The data are part of the INCT-CARBOM experiment, which aims to study carbon fluxes in the Brazilian continental margin. During the CARBOM cruise, vertical profiling by Conductivity, Temperature and Depth (CTD), lowered Acoustic Doppler Current Profiler (LADCP), vessel-mounted Acoustic Doppler Current Profiler (VMADCP) as well as Niskin bottle water samples were taken. The second quasi-synoptic data set consists of 12 CTD-LADCP stations and VMADCP profiles obtained in November of 2003 (11/07 - 11/11) during the MR03-K04 Leg 4 cruise (hereafter MR03) from the World Ocean Circulation Experiment (WOCE). The mooring lines used in this work are the ACM12/333, ACM12/334, ACM12/335 and ACM3/906 also from the WOCE (Müller et al., 1998; Hogg et al., 1999). They are equipped with conventional rotary currentmeters and ADCPs.

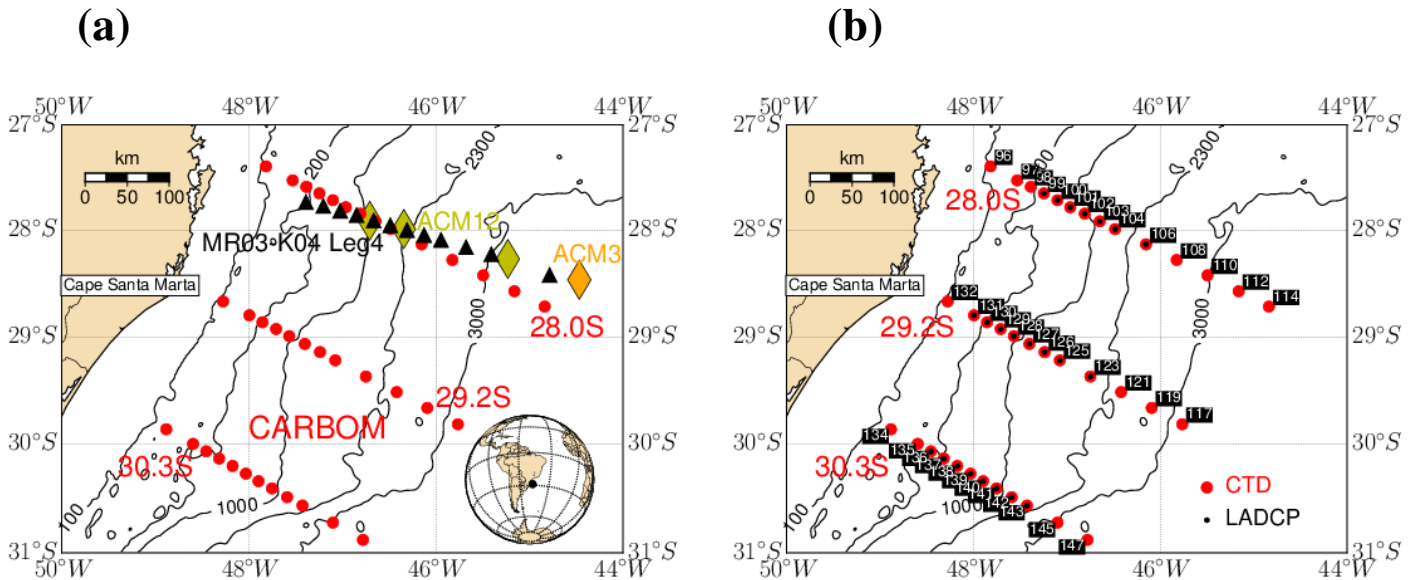


Figure 3.1: (a) The data set explored in this study. The circles (triangles) represent the locations of the CTD-LADCP stations of the CARBOM (MR03-K04 Leg 4) cruise and the diamonds the positions of the mooring lines.(b) CARBOM stations and its respective identification numbers. The large red numbers are the transects identification and corresponds to the respective mean latitudes.

3.2 The meanders vertical and horizontal structures

3.2.1 Velocity patterns and water masses

To shed light on the velocity structure of the cyclonic meanders at the vicinities of the Cape Santa Marta (28°S) we shall look at the top-bottom velocity observations from the CARBOM and MR03 cruises. During the both surveys, velocity profiles at each station were obtained using a downward-looking 300 kHz LADCP from RD Instruments. The data processing were carried out by following the procedures described by [Fischer and Visbeck \(1993\)](#) and [Visbeck \(2002\)](#). Additionally, 75 kHz VMADCP measurements taken on the ship's route were processed using the processing software Common Ocean Data Access System (CODAS) from the Currents Group of the University of Hawaii.

Figure 3.2 depicts the cross-sectional velocity component and the water masses vertical distributions at the transects that crosses the cyclonic meanders (MR03 and 29.2S). The TS Diagram overlaid on the [Mémery et al. \(2000\)](#) climatological water masses interfaces (panel a) show the presence of the Tropical Water (TW), South Atlantic Central Water (SACW), Antarctic Intermediate Water (AAIW), Upper Circumpolar Deep Water (UCDW) and North Atlantic Deep Water (NADW). Note that the CARBOM cruise presents waters with salinities (S) lower than 36 at temperatures (T) higher than 20°C . Studying the summer and winter water masses characteristics of the southwestern Atlantic shelf (28°S - 40°S), [Piola et al. \(2000\)](#) showed that shelf waters with $33.5 < S < 36.0$ ($T > 14^{\circ}\text{C}$) at $\sim 27\text{-}31^{\circ}\text{S}$ result from the mixing between TW and the continental runoff, also known as the Subtropical Shelf Water (STS).

The panels b and c present the velocity distributions and the respective sectional distributions of the cited water masses. The velocity panels consist of composites of the LADCP and VMADCP measurements. Such procedure were carried out following [Schott et al. \(2005\)](#) to improve the horizontal

resolution in the upper 500 m of the water column. Note that we present two different scenarios of the cyclonic meander during the MR03 and CARBOM cruises. The lower (higher) velocities of the meander coastal (oceanic) lobe, or positive (negative) velocity signal over the upper (lower) continental slope, from the MR03 suggest that data captured different stages of development of the meander phenomenon.

The panel **b** from Figure 3.2 depicts the meander coastal lobe with velocities lower than 0.10 m s^{-1} over the upper slope. The northeastward velocity signal is horizontally limited by the stations 624 and 627, indicating a horizontal and vertical extent of approximately 55 km and 1250 m, respectively. The total amount of water that is crossing the transect in the coastal lobe is approximately 1.50 Sv ($1 \text{ Sv} = 10^6 \text{ m}^3 \text{ s}^{-1}$). Further offshore, the whole water column (surface-2500 m) between stations 628 and 632 (110-202 km) flows southwestward. Note that this oceanic lobe has two distinguishable velocity cores with maximum velocities of -0.60 m s^{-1} and -0.25 m s^{-1} at the surface (station 630) and at 1250 m depth (station 631) respectively.

By combining the velocity pattern to the sectional distribution of the water masses defined by the *Mémery et al. (2000)* climatological interfaces (Figure 3.2), and the *Preu et al. (2013)*'s definition of UCDW and NADW based on neutral density (γ) and S for the Argentine Basin: UCDW is placed where $27.75 < \gamma < 27.90$, and NADW is placed where $27.90 < \gamma < 28.10$ and $S \geq 34.8 \text{ PSU}$; we were able to associate the flow sense of each water mass. The oceanic lobes observed during both surveys transports TW and SACW in the upper 500 m, AAIW at $\sim 500\text{-}1200 \text{ m}$, UCDW at approximately 1200-1500 m and NADW near the bottom at depths greater than 1500 m.

Excluding the NADW of the volume transport computation, the MR03 oceanic lobe transports approximately -17.89 Sv , which is comparable to the -22.8 Sv estimated by *Zemba (1991)* at 31°S from geostrophy. In that sense, the BC system has a net cross-sectional volume transport of $\sim -16.89 \text{ Sv}$. If we incorporate the NADW flow to the volume transport it becomes approximately -27 Sv , which is 2.3 Sv greater than the -24.7 Sv from *Zemba (1991)* estimate.

Although the water mass circulation pattern during the CARBOM cruise is similar to the pattern observed during the MR03 cruise, the meanders have significant differences. The coastal lobe presented in panel **c** from Figure 3.2 shows a well defined velocity signal from the surface to 1000 m depth between stations 129 and 126 (width $\approx 55 \text{ km}$). Moreover, it has one velocity core with maximum velocities of 0.32 m s^{-1} at the depth of approximately 600 m. Similarly to the MR03 cruise, the oceanic lobe (stations 126 and 123) has two prominent velocity cores: one with maximum subsurface velocities of approximately -0.37 m s^{-1} ; and other at intermediate depths with maximum velocities of $\sim -0.32 \text{ m s}^{-1}$.

We also computed the volume transport of each lobe by excluding the NADW flow. The coastal lobe has a transport of approximately 4 Sv and the oceanic one -13.16 Sv , which suggests that $\sim -9.16 \text{ Sv}$ should be crossing the 29.2°S transect poleward. Observe that the BC was partially sampled only during the CARBOM cruise, nevertheless we obtained comparable transport for the BC to the values obtained from the MR03 data.

In an attempt to expand our description of the cyclonic meanders, we used the VMADCP and LADCP measurements from the all three CARBOM transects to map the horizontal structure of this feature. In that sense we objectively mapped the stream functions (Ψ) at different depths following *Gille (2003)*. The mapping procedure uses Gaussian covariance functions that satisfy geostrophic continuity and

incorporates error estimates on the data to produce a mapping error (*Bretherton et al., 1976*). Based on the transects spacing and the VMADCP and LADCP errors we used an isotropic decorrelation scale of 1.2° (~ 130 km) and a data fractional error (e) of 0.1.

Figure 3.3 presents the streamlines at 30 m (near surface level), at 700 m and the respective normalized error maps ($e_{max} = 0.22$). Both maps show that the transect 29.02S does not crosses the center of the eddy structure, which seems to be located south (center of maximum Ψ). The mapped cyclonic meander exceeds 100 km of diameter likewise we estimated in the sectional velocity distribution. Moreover, we speculate that the offshore northward flow seen at 30 m depth might be part of the BC recirculation cell (*Vianna and Menezes, 2011*).

Note that we omitted the presence of a layer of low salinity (STSW) in the first ~ 50 -70 m in the Figure 3.2 (panel **c**) description. The STSW plume extends to more than 150 km from the 100 m isobath and can be tracked by the 36 isohaline. In that sense, we linearly interpolated the salinity at different depths to compare it with the near surface stream lines maps. The S=36 line at 30 m (Figure 3.3, panel **a**) reasonably follows the internal edge of the oceanic lobe, corroborating the Ψ mapping and indicating that the low salinity distribution is associated with the meander.

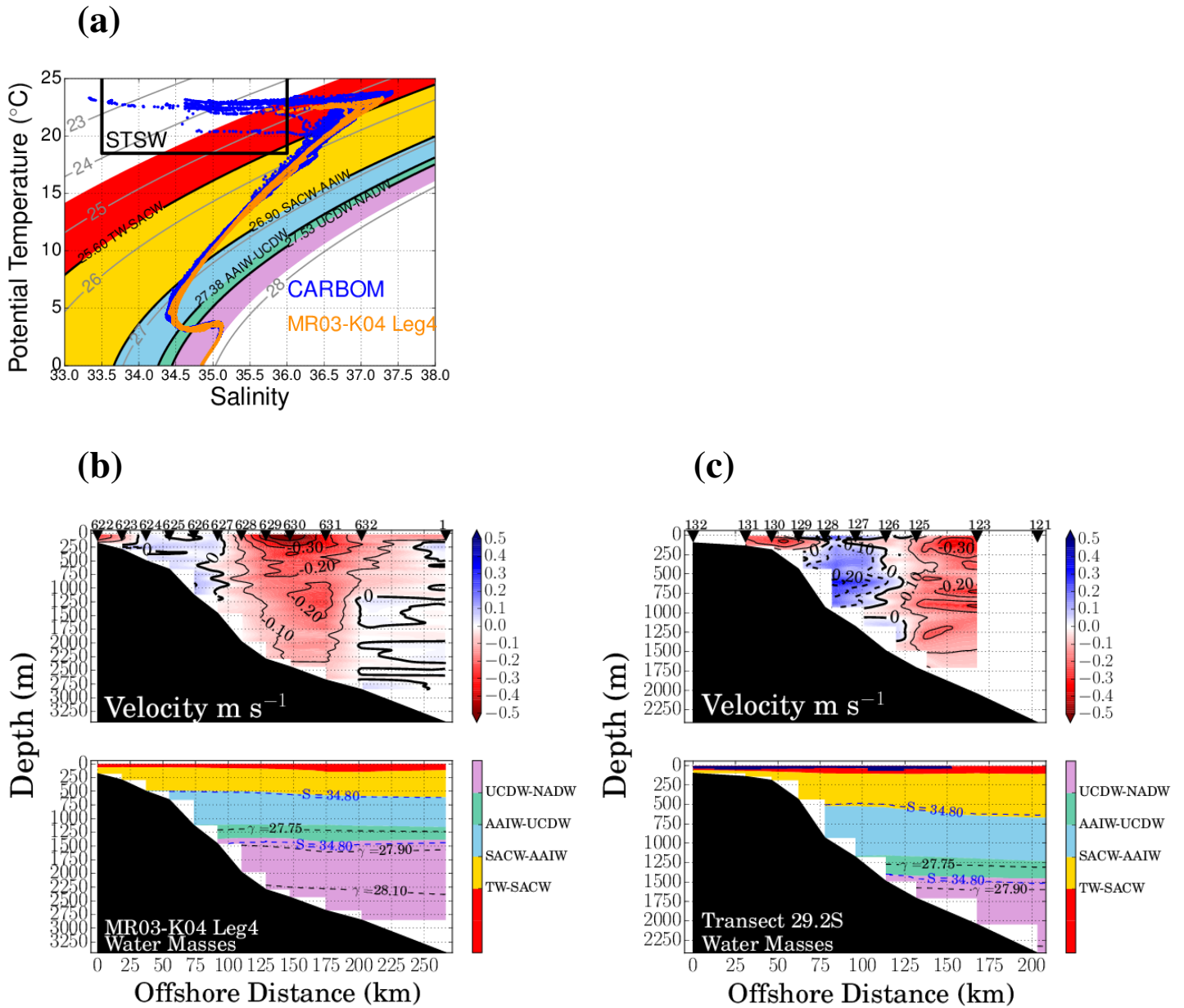


Figure 3.2: (a) Scattered TS Diagram overlaid on the *Mémetry et al.* (2000) climatological water masses interfaces. Sectional velocity and water masses distributions observed during the (b) MR03 and (c) CARBOM cruises. The black triangles indicate the positions of the CTD and LADCP stations. The 34.8 salinity (S) and 27.75, 27.90 and 38.10 neutral density (γ) lines were also plotted. The water masses color scheme were masked for the regions where the STSW was found with a dark blue mask.

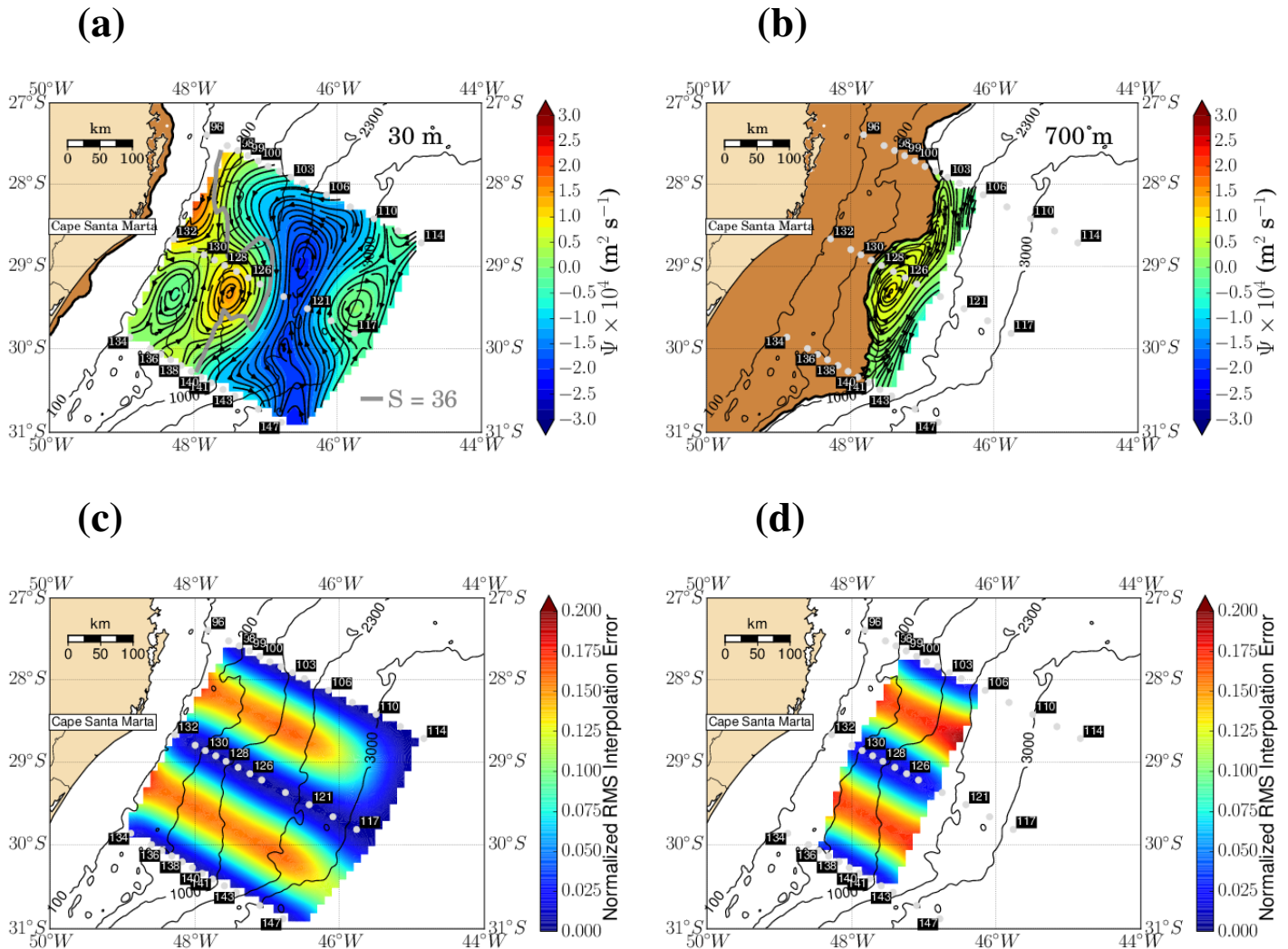


Figure 3.3: The mapped stream function (Ψ) at (a) 30 m and (b) 700 m depth. The respective mapping errors are presented in panels (c) VMADCP and (d) LADCP. The thick grey line indicate the 36 salinity line at 30 m.

3.2.2 Evidences of shelf-slope mass exchanges and water trapping

Matano et al. (2014) performed a series of numerical simulations that showed the vicinities of 28°S as a spot of shelf-open ocean mass exchange. Based on their results, the authors argued that the exportation of the shelf waters to the open ocean are strongly associated with the BC mesoscale activity. In fact the data from CARBOM cruise, described in the previous section, indicate that we captured such interaction between the BC and shelf waters with STSW entrained in the vortical feature. As that being the case we should try to better describe this phenomena and evaluate its possible impacts in the oceanic water properties.

The cyclonic meander signature is well depicted by the salinity distributions in Figure 3.4. The low salinity tongue crosses the shelf break and reaches the 2000 m isobath, which corresponds to distances higher than 150 km away from the 100 m isobath. As expected, once the the water is trapped in the center of a cyclonic eddy (low pressure center) the surface waters tend to be pushed downward in the water column due to the surface convergence (*Cushman-Roisin and Beckers, 1994*). Note that stations 126 and 127 are the only locations where the STSW penetrate at depths of ~70 m (panels c and d).

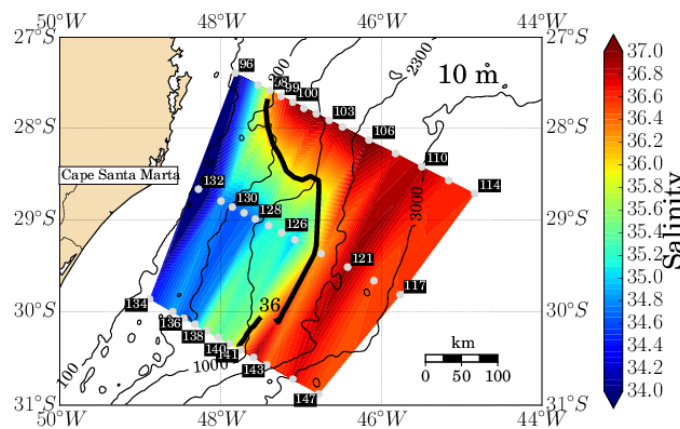
We mentioned in Section 3.1 that the BC cyclones near Cape Santa Marta were originally reported from SST satellite imagery. However we think surface temperature may not be always a good tracer for detecting the cyclones due to the lack of thermal contrast between shelf and BC waters. By re-examining the TS Diagram (Figure 3.2, panel **a**) and the TS profiles (3.4, panel **d**) we observe that the temperature variations near surface are very small compared to S variations in all CTD stations ($\leq 1.5^{\circ}\text{C}$).

Another important shelf-slope mass exchange aspect to be verified is the wind influence. Its well known that the wind is the primary forcing agent of the circulation in the southern portion of the Brazilian continental shelf (23°S - 34°S). Additionally the northeasterly winds play an important role in the exportation of surface water to the open ocean and in the shelf-break upwelling system (*Campos et al., 2000; Castelao et al., 2004; Palma et al., 2004, 2008; Matano et al., 2010*). Thus, we carried out a simple assessment of the Ekman transport based on 9 days of sea surface winds (11/13/2013-11/21/2013). The wind data are from the daily NCDC/NOAA Blended Seawinds L4 product available in <http://www.ncdc.noaa.gov>, that combines different satellite measurements to resolve multi-temporal and spatial scales phenomenon.

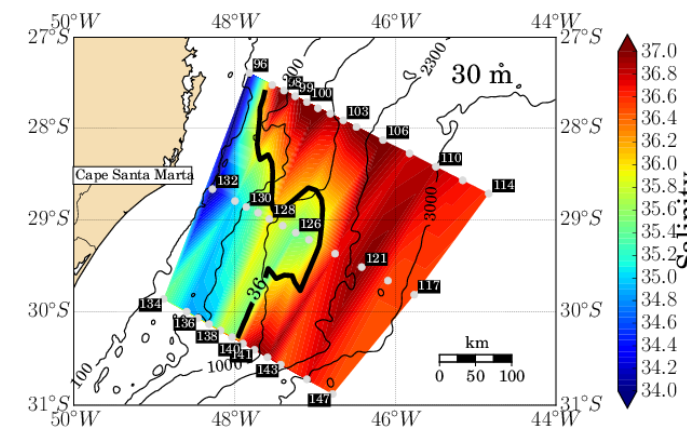
Figure 3.5 shows the sea surface winds vectors and magnitude from 5 days before the start of the CARBOM cruise to the end of the transect that crossed the meander. In the time period 11/13 to 11/17 there are two shifts in the winds directions, probably associated with cold fronts that are common in this region. From 11/18 (cruise start) to 11/20 the northeasterly winds became persistent and considerably intense ($\geq 10 \text{ m s}^{-1}$). The approximately 72 h of such winds are enough to impose an important offshore Ekman transport at the surface, since the inertial period (T_i) is around 25.5 h.

In that sense, we believe that the STSW distribution observed during the CARBOM cruise resulted from a combination of the winds action and the presence of the cyclonic meander. The clear meander signature in the salinity data also suggests that once the water is captured by the meander, it remains trapped and the water particles become locked in the BC path (e. g., *Matano et al., 2014*).

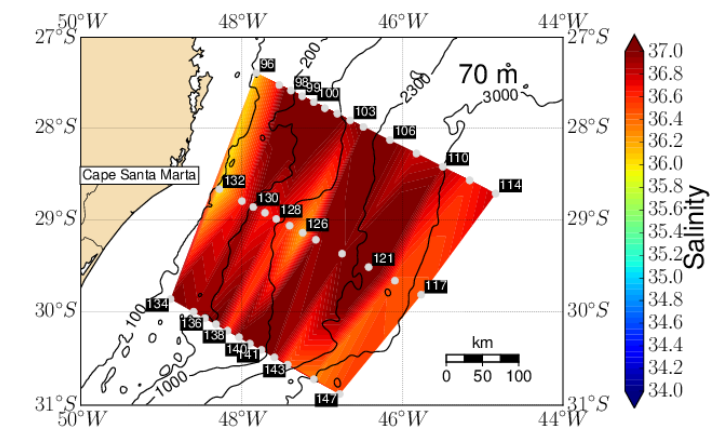
(a)



(b)



(c)



(d)

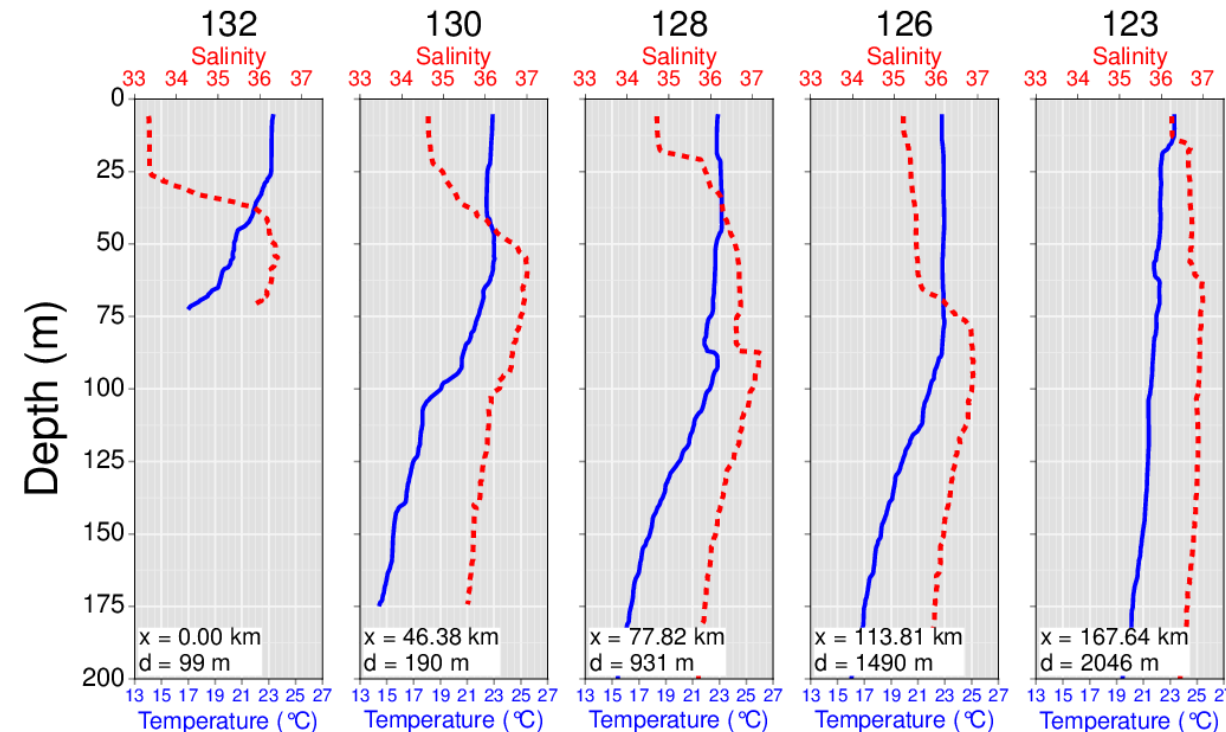


Figure 3.4: Horizontal salinity distributions at (a) 10 m, (b) 30 m and (c) 70 m depth. Panel (d) presents the temperature and salinity profiles from transect 29.02S where the STSW is present. The numbers x and d represent the distance from the 100 m isobath and local depth respectively.

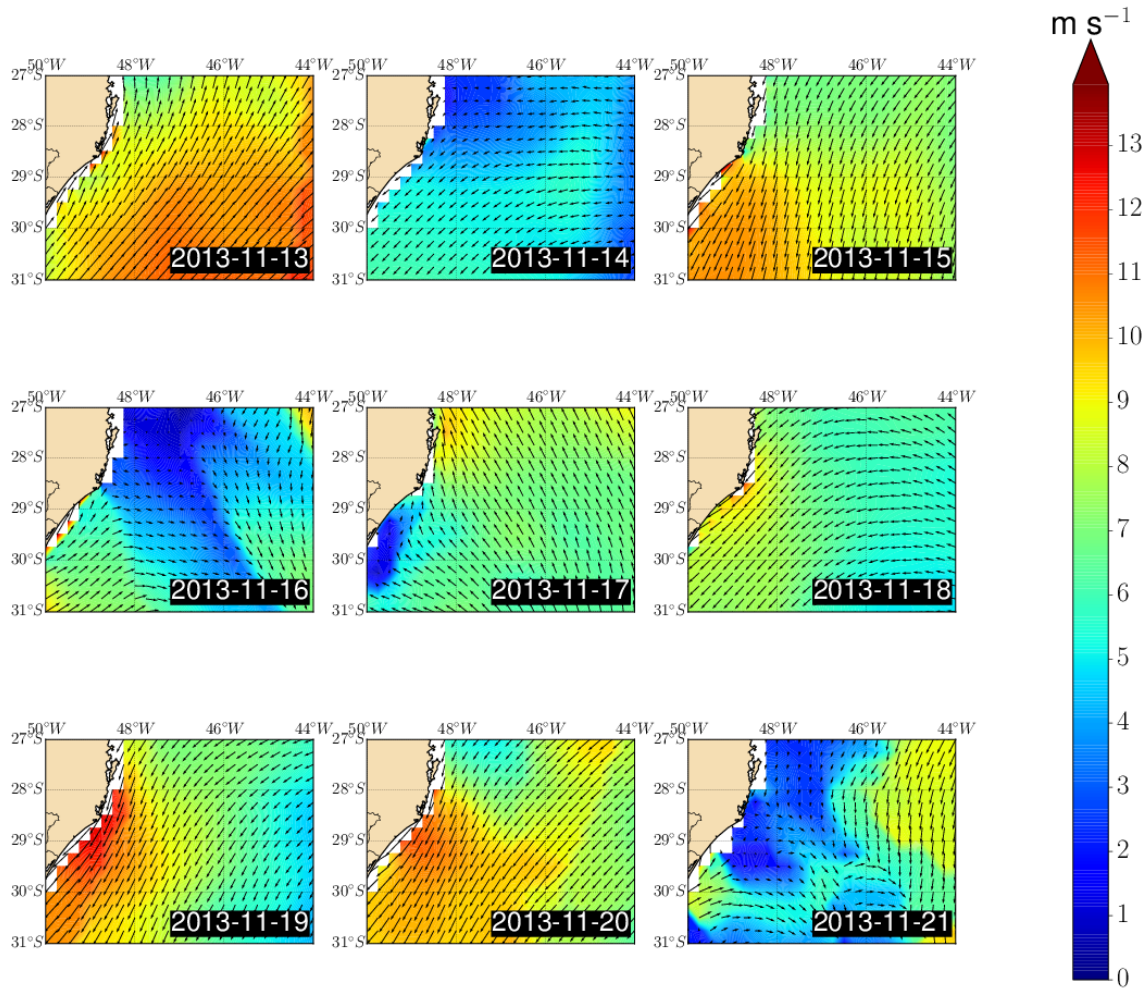
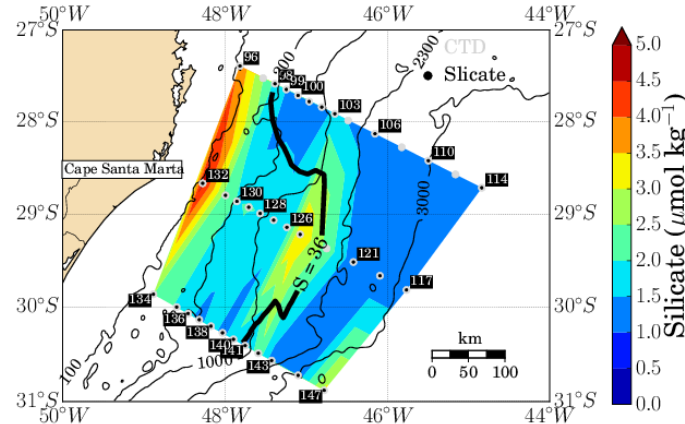


Figure 3.5: Daily sea surface winds distributions for the period between 11/13/2013 and 11/21/2013. The wind data are from the daily NCDC/NOAA Blended Seawinds L4 product.

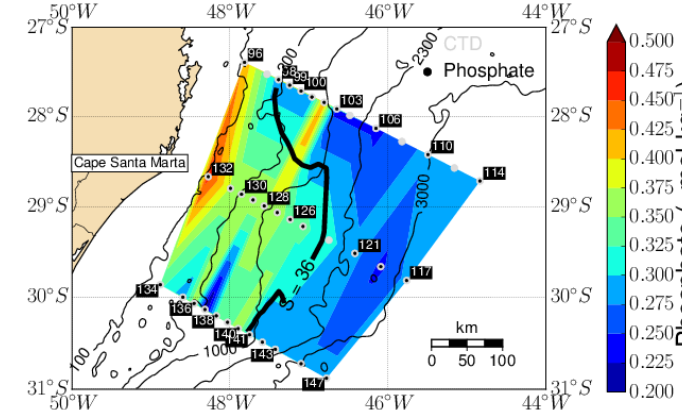
To conclude this section, we shall see which are some consequences of the STSW offshore transport in some nutrients distributions and primary productivity. Unfortunately the available data set did not allow us to study it in a quantitative manner, nevertheless our snapshots provided evidences regarding these impacts. Figure 3.6 presents the concentrations of silicate, phosphate, nitrate, ammonium and chlorophyll-a at 5 m depth for the CARBOM cruise. The concentrations were obtained from water samples collected and analysed following the procedures described by *Grasshoff et al. (1983)* and presented values are in agreement with the values expected for STSW and TW waters presented by *Braga et al. (2008)* and *Piola et al. (2008)*.

Comparing the nutrients distributions with the 36 isohaline, the meander signature is clear in all maps of Figure 3.6 with exception in the nitrate distribution (panel c). Note that the shelf waters richer in nutrients are trapped close to the eddy center (stations 125 and 126) and the coastal lobe, while the oligotrophic oceanic waters follow the BC main axis offshore to the S=36 line. Another interesting characteristic is that the maximum concentration of all nutrients are not located at the same regions as the maximum of primary productivity associated with the higher concentration of chlorophyll-a (stations 128, 129 and 130). This might suggest that the shelf waters are trapped long enough to have its nutrients content depleted by the organisms in higher productive regions of the meander.

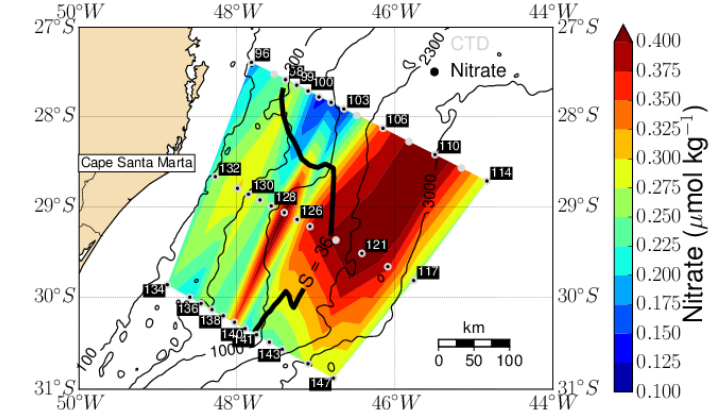
(a)



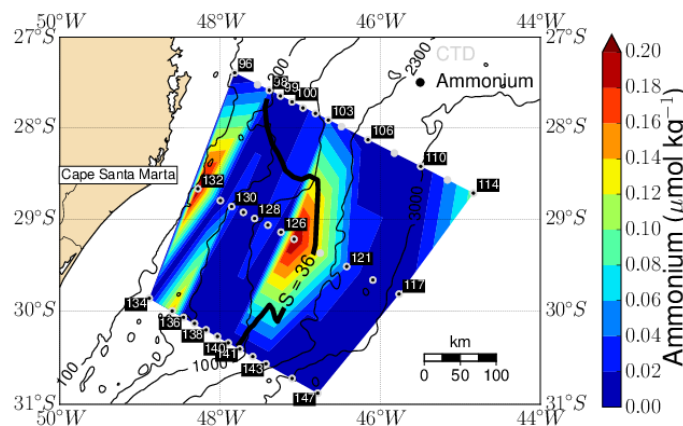
(b)



(c)



(d)



(e)

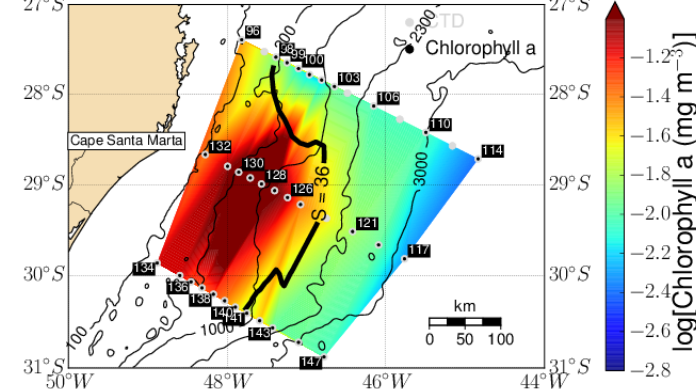


Figure 3.6: Distribution at 5 m depth of the concentration of (a) silicate, (b) phosphate, (c) nitrate, (d) ammonium and (e) chlorophyll-a. The thick black line indicate the salinity of 36 at 5 m depth. The dots indicate where CTD profiles and water samples were taken.

3.3 The Brazil Current variability and cyclones recurrence

In the previous sections we showed the BC cyclonic meanders water mass patterns, physical dimensions and its possible role in the shelf-slope mass exchanges. However two important questions remain open: (1) How often the cyclonic eddies occur at the vicinities of Cape Santa Marta? and (2) How much do these features account for the BC variability?

We saw from the literature and our analysis that the meanders not only present a signature in the SST but also in the chlorophyll-a distribution. Thus, to answer the first question we analysed 12 years (June/2002 - June/2014) of L4 satellite imagery from two different products, the daily Multi-scale Ultra-high Resolution (MUR) SST Analysis (<http://podaac-opendap.jpl.nasa.gov/>) and the 8-day composite Moderate Resolution Imaging Spectroradiometer (MODIS) sensor aboard of the Aqua satellite (<http://oceancolor.gsfc.nasa.gov/>). As expected, distinguishable cyclonic eddy events were found in both sets of images between 27.5°S and 30°S. However only 16 independent events (~1.3 events year⁻¹) were observed in the SST images while 66 events (~5.5 events year⁻¹) were registered in the sea surface chlorophyll-a imagery (see example in Figure 3.7).

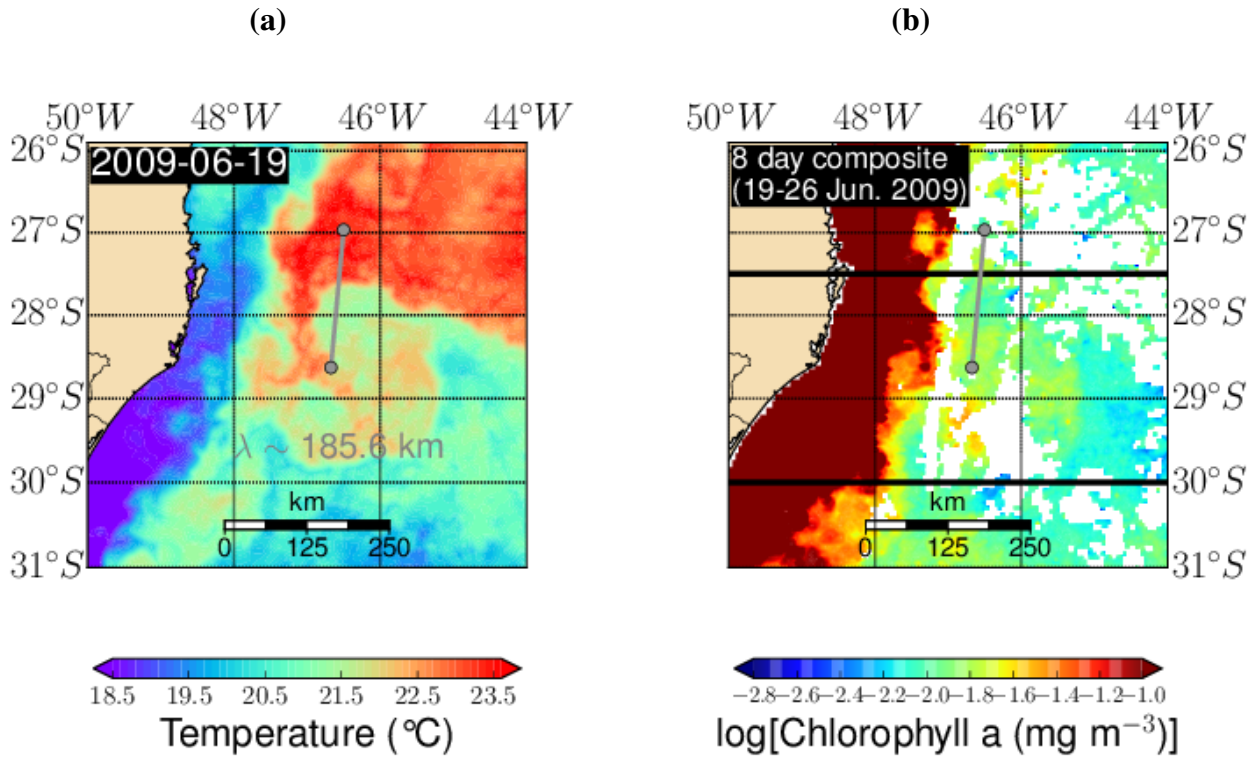


Figure 3.7: Same cyclonic meander event captured by the (a) daily SST and (b) 8-day composite sea surface chlorophyll-a satellite L4 images from MUR and MODIS respectively. The grey line and dots demarcate two consecutive peaks of the supposed vorticity wave shown by the thermal and chlorophyll-a fronts.

The 50 events discrepancy has two reasons. The low thermal contrast between shelf and open ocean waters in some of the events, and the frequent large cloud covering of the region. Since we are dealing with an objectively mapped daily SST product, when the cloud coverage of the sky is large, the SST distributions become fuzzy and therefore the fronts can not be observed. Nevertheless, the 16 events found simultaneously in the both products presented wave like fronts with a mean wavelength

of 219 km and standard deviation of 46 km. In Figure 3.7 we present one of the 16 events and its respective temperature and chlorophyll-a fronts. It's important to mention that no clear signal of eddies that detached from BC were observed.

Question (2) was addressed using the WOCE mooring lines array. These currentmeters time series were extensively explored in the literature and had its velocity signal already discussed (e. g., Müller *et al.*, 1998; Hogg *et al.*, 1999; Rocha *et al.*, 2013, 2014). In that sense we reproduced Sato (2014) by computing the Empirical Orthogonal Functions (EOF) of the time series velocity array to characterize the subinertial variability of the BC (Figure 3.8). To compute only the BC subinertial oscillations, each currentmeter time series was low-pass filtered using a Lanczos squared filter with a 40 h cut-off (e. g., Emery and Thomson, 2001). We also rotated the velocity vectors in 30° clockwise to obtain the velocity component normal to the mooring array axis, which represents the component approximately parallel to the 200 and 1000 m isobaths. Rocha *et al.* (2014) showed that this is the BC preferential flow direction in the region. Moreover the EOF were computed only for the common time period to all velocity records (01/05/1991 - 11/25/1992).

The mean cross-sectional velocity values (Figure 3.8, panel **a**) show part of the BC signal in the upper 1000 m over the continental slope. The positive velocity signals in the upper 500 m and at depths greater than 3000 m are related to the BC recirculation cell and the Antarctic Bottom Water flow respectively (Müller *et al.*, 1998; Hogg *et al.*, 1999).

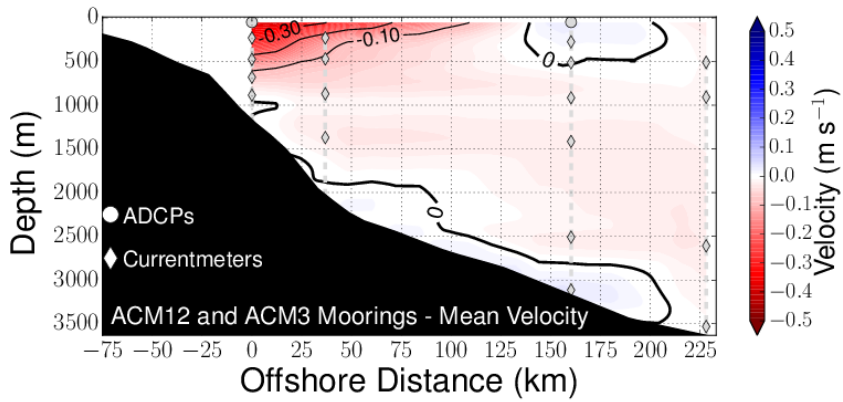
A Monte Carlo simulation indicate that only the first two EOF modes are statistically significant at the 95% level (Preisendorfer, 1988). The first EOF (Figure 3.8, panel **b**), which explains 54% of the variance, clearly represents the mesoscale oscillations of the BC. The spatial structure of this mode has the highest values in the BC domain. Additionally, the energy spectrum show that the time series of the first mode is dominated by oscillations with periods of approximately 26 days. Therefore the mesoscale oscillations, such as the BC meanders, explains approximately half of the variability over the continental slope near the Cape Santa Marta. The second EOF explains approximately 30% of the variance and seems to be related to the BC recirculation cell (Figure 3.8, panel **c**). Its spatial structure is essentially confined in the upper 500 m of the water column and is centred on the recirculation area. The second mode time series is dominated by large scale oscillations with periods of ~103 days, i. e., the main variability mode of the BC recirculation is seasonal.

3.4 Summary and conclusions

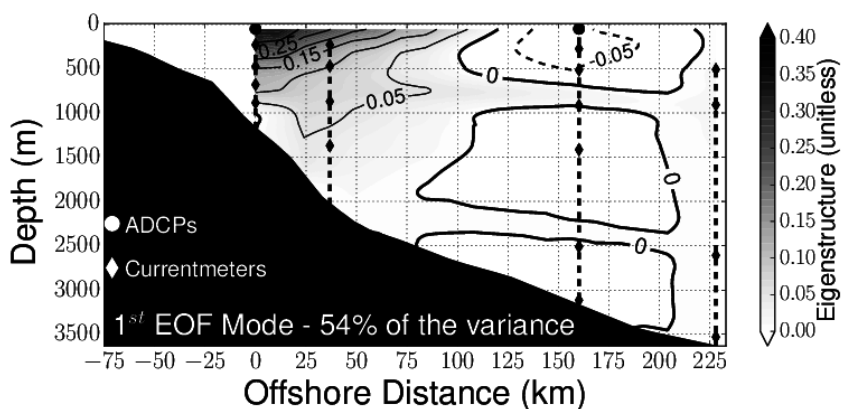
We described the basic characteristic of the BC cyclonic meanders near Cape Santa Marta (28°S). A wide range of observations were used to provide a rich overview of the meanders and the relations between its velocity patterns and water masses circulation; surface temperature, salinity, nutrients and chlorophyll-a distributions; and the BC current variability.

The top-bottom quasi-synoptic velocity measurements depicted cyclonic meanders over the continental slope with diameters larger than 100 km. Moreover the eddies presented velocity signal extending to approximately 1500 m depth, which highlights the dynamical coupling of the upper 500 m flow with the intermediate one (500-1500 m). The observed BC eddies seems to trap and recirculate a small portion (~1.5 to 4 Sv) of the BC main flow (-13.16 to -17.89 Sv), which is consisted of TW, SACW, AAIW and UCDW. Additionally, we presented observational evidence of the influence of the

(a)



(b)



(c)

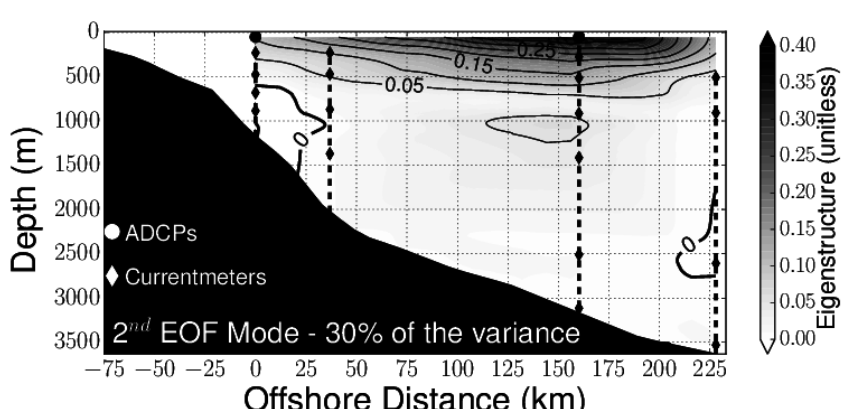


Figure 3.8: Summary of the EOF analysis of the mooring lines array from the WOCE Experiment for the time period 01/05/1991 - 11/25/1992 (Hogg et al., 1999). (a) Mean cross-sectional velocity array; (b) the first statistical mode eigenstructure and energy spectrum; and (c) the second statistical mode eigenstructure and energy spectrum. The gray dashed lines represent the mooring lines.

cyclonic meanders in the shelf-open ocean exchanges. The salinity horizontal distributions combined with the nutrients concentrations led us to conclude that the BC meanders actively influence the STSW

transport to the open ocean (e. g., *Matano et al.*, 2014), enhancing the primary productivity at the photic zone over the continental slope.

From satellite imagery, the cyclonic meandering of the BC is generally associated with a wave-like perturbation on the flow with mean wavelength of ~219 km, corroborating the *Garfield* (1990) findings. Moreover, the sea surface chlorophyll-a imagery analysis was more efficient than the SST analysis in determining the meander recurrence. We estimated that independent cyclonic features may occur 5 to 6 times per year off Cape Santa Marta. Finally, our EOF analysis computed from an array of mooring lines equipped with currentmeters show that approximately half of the variance on the continental slope is explained by the BC mesoscale activity. Therefore almost 55% of the BC subinertial variability is related to its meandering in this region.

We should stress out, however, that this study was not able to quantitatively address some important points related to the cross-shelf exchanges and its biological impacts due to the limitation of the observations. Future observational programs and modelling efforts should seek quantify the relative importance of the wind forcing and smaller scale processes (e. g., submesoscale) compared to the mesoscale.

Chapter 4

Final remarks

In this work we investigated the characteristics of the BC and its meanders at 23°S-31°S, and how linear instability properties of this current system change north and south of the Santos Bifurcation in the presence of vertical and horizontal velocity shears. Combining high-quality observations with a numerical model we confirmed thesis hypotheses.

Using observational and numerical perspectives, we addressed in Chapter 2 the mixed-instability phenomenon and its relation with the downstream changes of the BC system. Quasi-synoptic velocity observations revealed that to the north of the Santos Bifurcation ($\sim 27^{\circ}\text{S}$) the BC is $\sim 400\text{-}500$ m deep, although can reach deeper regions depending on its energetic state. Its important to stress out that the volume transport increases southward at 23°S-27°S though, and seems to be related to its width and velocity getting larger downstream. To the south of the bifurcation the BC extends down to 1000 m. We estimated that the BC receives at least 7 Sv at intermediate depths from the Santos Bifurcation, which drastically alters its velocity patterns and eddies characteristics.

Based on our numerical experiments with a PE linear instability model, we concluded that the BC system is more unstable ($0.10 < -\sigma_i < 0.20 \text{ day}^{-1}$) and the instability waves propagate phase downstream with slightly weaker velocities ($c < 0.26 \text{ m s}^{-1}$) at 23°S-27°S. Additionally we were able to quantify the relative importance of the barotropic and baroclinic instabilities by comparing the mean to eddy energy conversion terms. We found that the baroclinic instability is the primary mechanism ($>60\%$) for the perturbations growth along the BC path. However the barotropic instability had a significant impact on the linear instability properties being more important in draining energy from the mean currents to the north of the bifurcation.

Finally were not able to address the real impact of the topography differences in the instability process and therefore further investigation is required. Nevertheless our experiments showed that the topography has a stabilizing effect. In contrast to the system at 30°S, the relative importance of the barotropic instability increased in the absence of topography to the north of 28°S. In addition, the BC flows over a high steepness continental slope, therefore the use of QG models is limited in not allowing a first order topographic effect.

In Chapter 3, we focused in the description of the basic characteristic of the BC cyclonic meanders near Cape Santa Marta (28°S) using a wide range of observations. From two different quasi-synoptic data sets, we corroborated the findings of Chapter 2 regarding the vertical velocity structure of the meanders to the south of the Santos Bifurcation. Comparing cyclonic meanders at different stages of

development we found that the intermediate flow indeed meanders consonantly with the BC above it, indicating a dynamical coupling south of 27°S.

The satellite imagery showed the cyclonic meandering is generally associated with a wave-like perturbation on the flow with mean wavelength of ~219 km. Moreover, we found that the sea surface chlorophyll-a imagery analysis was more efficient than the SST analysis in detecting the meander occurrence (5 to 6 times per year). Finally our EOF analysis indicate that more than half of the along-isobath velocity time series variance on the continental slope was explained by the BC mesoscale activity.

Appendix A

Model parameters and idealized experiments background states

All the scales and parameters used to build the background states and run the stability model are presented in Tables A.1, A.2 and A.3. Additionally, Figures A.1-A.6 depict the velocity background fields from the idealized experiments $24S_{nt}$, $24S_{bc}$, $26S_{nt}$, $26S_{bc}$, $30S_{nt}$ and $30S_{bc}$.

Table A.1: Scales of the background states used in the numerical experiments.

Parameters	24S	$24S_{nt}$	$24S_{bc}$	26S	$26S_{nt}$	$26S_{bc}$	30S	$30S_{nt}$	$30S_{bc}$
L_0 (km)	100.00	100.00	200.00	100.00	100.00	200.00	100.00	100.00	200.00
H_0 (m)	3040.21	1000.00	1000.00	2853.92	1000.00	1000.00	3212.92	1000.00	1000.00
V_0 ($m s^{-1}$)	0.50	0.50	0.50	0.54	0.54	0.54	0.46	0.46	0.46
N_0 ($10^{-3} s^{-1}$)	12.00	8.00	8.00	11.5	7.9	7.9	12.00	7.7	7.9
f ($10^{-5} s^{-1}$)	-5.93	-5.93	-5.93	-6.39	-6.39	-6.39	-7.51	-7.51	-7.51

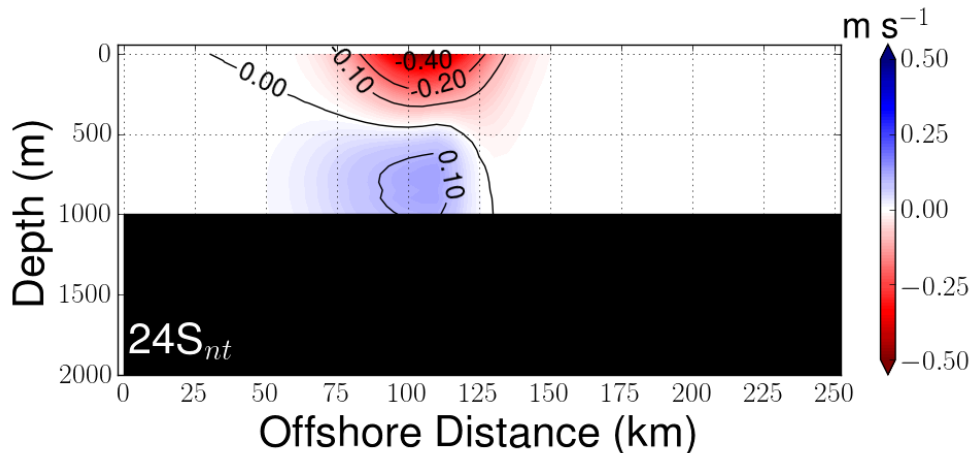


Figure A.1: The parametrized velocity field from the idealized experiment $24S_{nt}$.

Table A.2: Parameters of the background states used in the numerical experiments to the north of the Santos Bifurcation. For the idealized experiments (“Transect_{nt}” and “Transect_{bc}”) the modified parameters are shown in boldface.

Parameters	24S	24S _{nt}	24S _{bc}	26S	26S _{nt}	26S _{bc}
H_s (m)	50.00	1000.00	1000.00	70.00	1000.00	1000.00
H_d (m)	3040.21	1000.00	1000.00	2853.92	1000.00	1000.00
X_m (km)	123.90	-	-	129.43	-	-
α (km)	-63.63	-	-	-61.62	-	-
V_{c0} (m s ⁻¹)	-0.50	-0.50	-0.50	-0.54	-0.54	-0.54
Z_s (m)	299.67	299.67	299.67	495.15	495.15	495.15
X_{c0} (km)	105.00	105.00	180.00	100.03	100.03	199.44
L_c (km)	22.99	22.99	46.00	19.40	19.40	38.79
L_o (km)	22.99	22.99	46.00	27.76	27.76	55.51
A	10^{14}	10^{14}	10^{14}	36.56	36.56	36.56
V_{ci0} (m s ⁻¹)	0.17	0.17	0.17	0.18	0.18	0.22
Z_{is} (m)	1076.29	1076.29	1076.29	2190.19	2190.19	2190.19
Z_{ci0} (m)	897.20	897.20	897.20	970.67	970.67	970.67
h_{is} (m)	405.16	405.16	405.16	462.56	462.56	462.56
h_{ib} (m)	541.49	541.49	541.49	462.56	462.56	462.56
X_{is} (km)	26.14	26.14	52.00	11.25	11.25	11.25
X_{ci0} (km)	109.00	109.00	184.00	132.95	132.95	232.37
L_{ic} (km)	34.86	34.86	70.00	95.24	74.56	99.41
L_{io} (km)	11.86	11.86	24.00	24.85	24.85	49.71
A_i	$2.3 \cdot 10^5$	$2.3 \cdot 10^5$	$2.3 \cdot 10^5$	1768.70	1768.70	1768.70
B_i	19.52	19.52	19.52	100.82	100.82	100.82

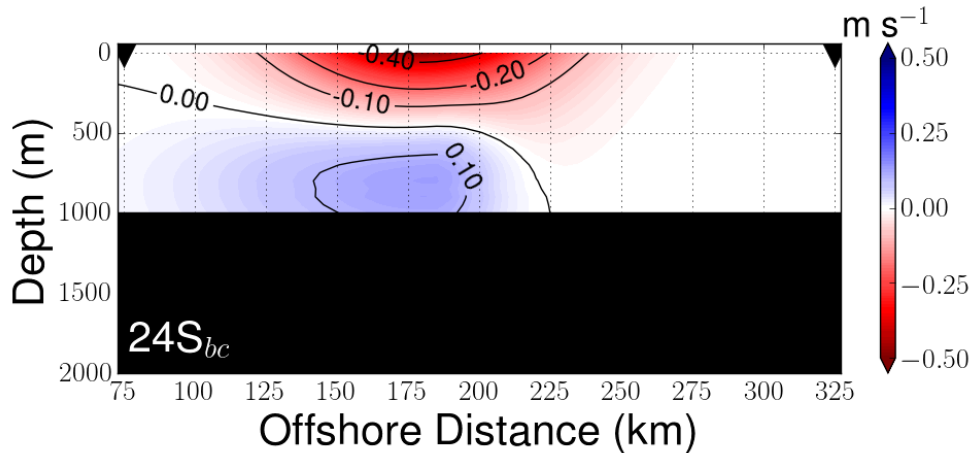


Figure A.2: The parametrized velocity field from the idealized experiment 24S_{bc}. Since this experiment had its horizontal boundaries extended we indicated the original area limits with the black triangles.

Table A.3: Parameters of the background states used in the numerical experiments to the south of the Santos Bifurcation. For the idealized experiments (“Transect_{nt}” and “Transect_{bc}”) the modified parameters are shown in boldface.

Parameters	30S	30S _{nt}	30S _{bc}
H_s (m)	140.03	1000.00	1000.00
H_d (m)	3212.92	1000.00	1000.00
X_m (km)	198.42	-	-
α (km)	-49.33	-	-
V_{c0} (m s ⁻¹)	-0.46	-0.46	-0.46
Z_s (m)	498.79	498.79	498.79
X_{c0} (km)	156.00	156.00	205.36
ℓ (km)	24.68	24.68	49.36
A	23.62	23.62	23.62
G_{10} (m s ⁻¹)	-0.13	-0.13	-0.13
G_{1L} (km)	22.49	22.49	44.98
G_{1X} (km)	116.00	116.00	127.24
G_{1Z} (m)	197.07	197.07	197.07
G_{1Zs} (m)	200.25	200.25	200.25
G_{20} (m s ⁻¹)	-0.08	-0.08	-0.08
G_{2L} (km)	16.47	16.47	32.93
G_{2X} (km)	196.00	196.00	286.51
G_{2Z} (m)	742.60	742.60	742.60
G_{2Zs} (m)	537.60	537.60	537.60

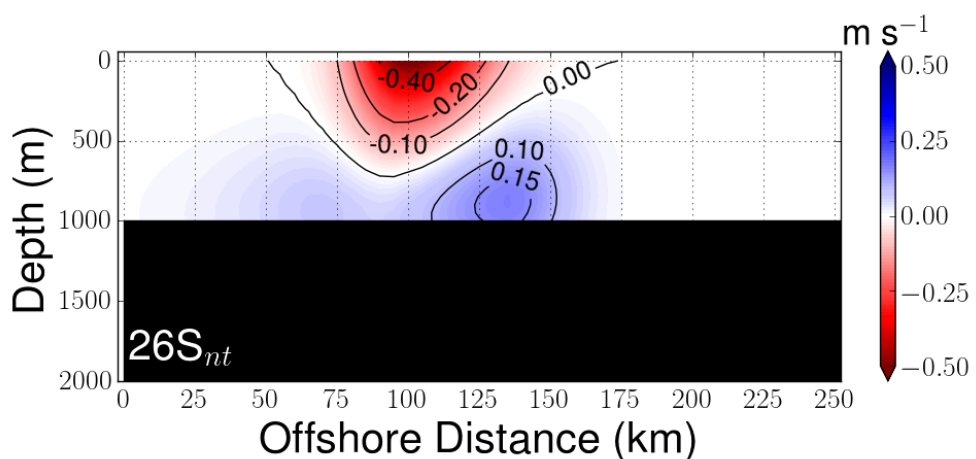


Figure A.3: The parametrized velocity field from the idealized experiment 26S_{nt}.

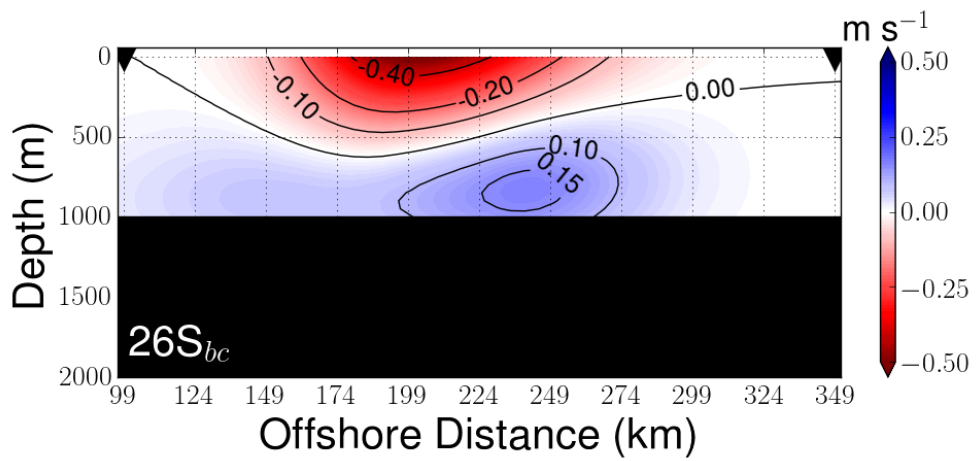


Figure A.4: The parametrized velocity field from the idealized experiment $26S_{bc}$. Since this experiment had its horizontal boundaries extended we indicated the original area limits with the black triangles.

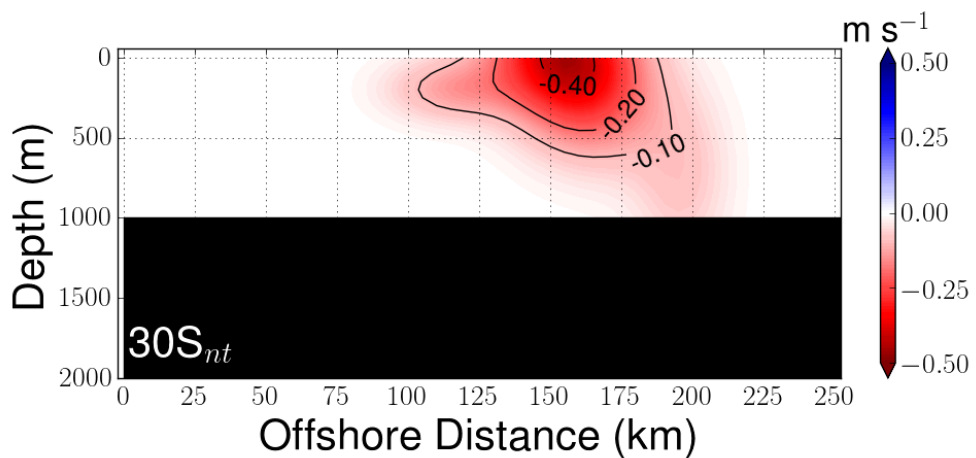


Figure A.5: The parametrized velocity field from the idealized experiment $30S_{nt}$.

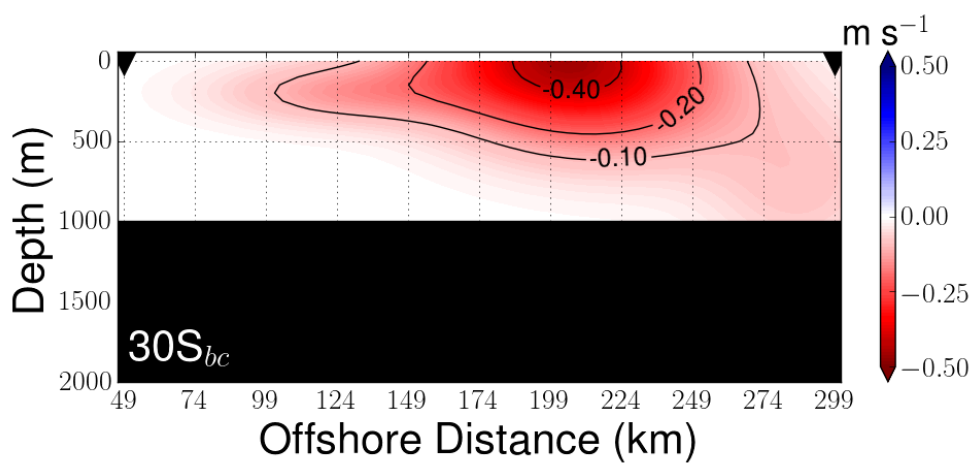


Figure A.6: The parametrized velocity field from the idealized experiment $30S_{bc}$. Since this experiment had its horizontal boundaries extended we indicated the original area limits with the black triangles.

Appendix B

Perturbations and energy conversion terms from the idealized experiments

Figures B.1-B.6 present the amplitudes of the perturbations fields and the energy conversion terms HHF, VHF and RS from the idealized experiments (indexes n_t and b_c). The plotted area off these figures are consistent with the experiments 24S, 26S and 30S for direct comparison.

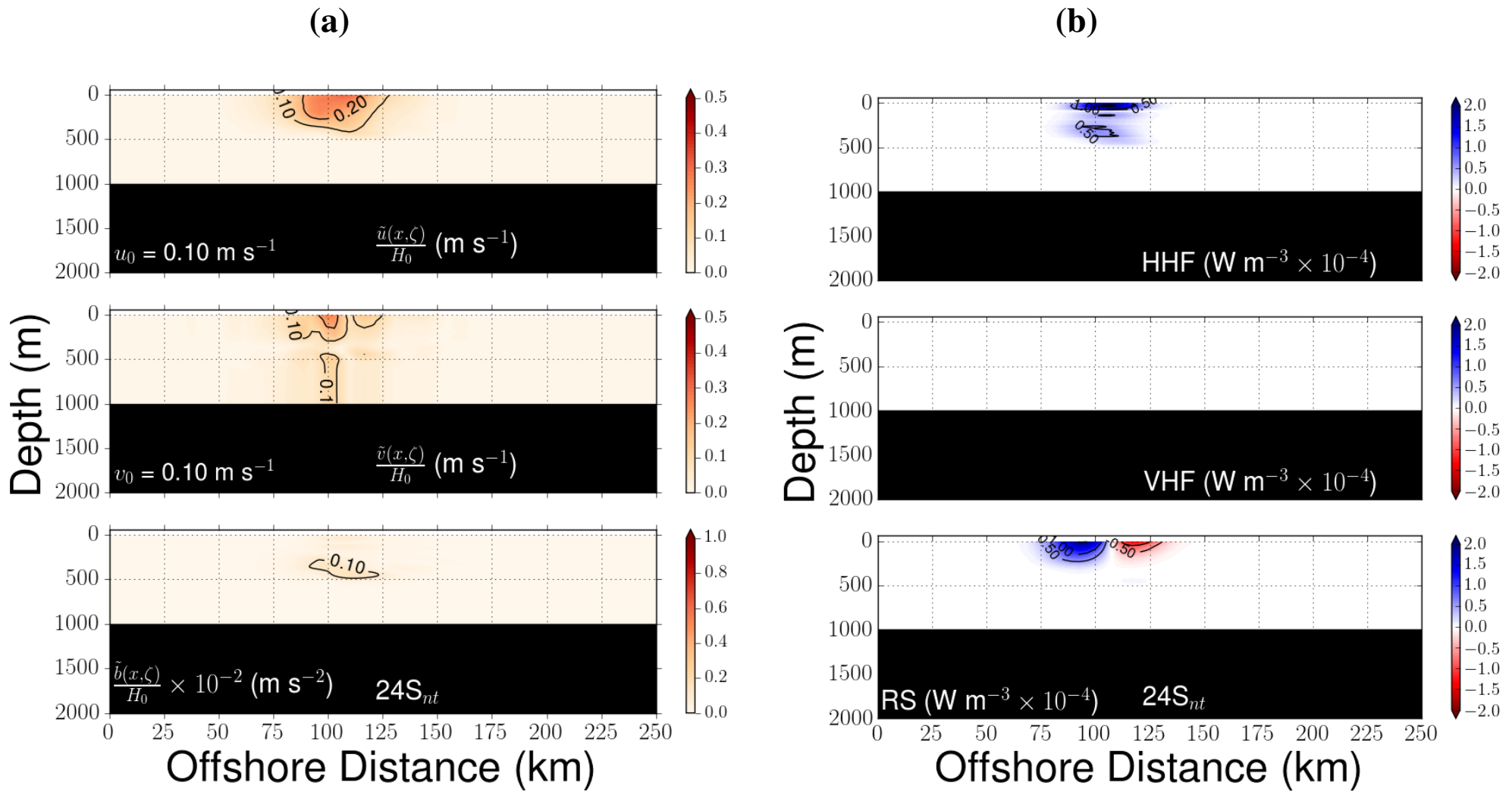


Figure B.1: **(a)** Amplitudes of the perturbations fields ($\frac{\tilde{u}(x,\zeta)}{H_0}$, $\frac{\tilde{v}(x,\zeta)}{H_0}$ and $\frac{\tilde{b}(x,\zeta)}{H_0}$) and **(b)** energy conversion terms HHF, VHF and RS from experiment $24S_{nt}$.

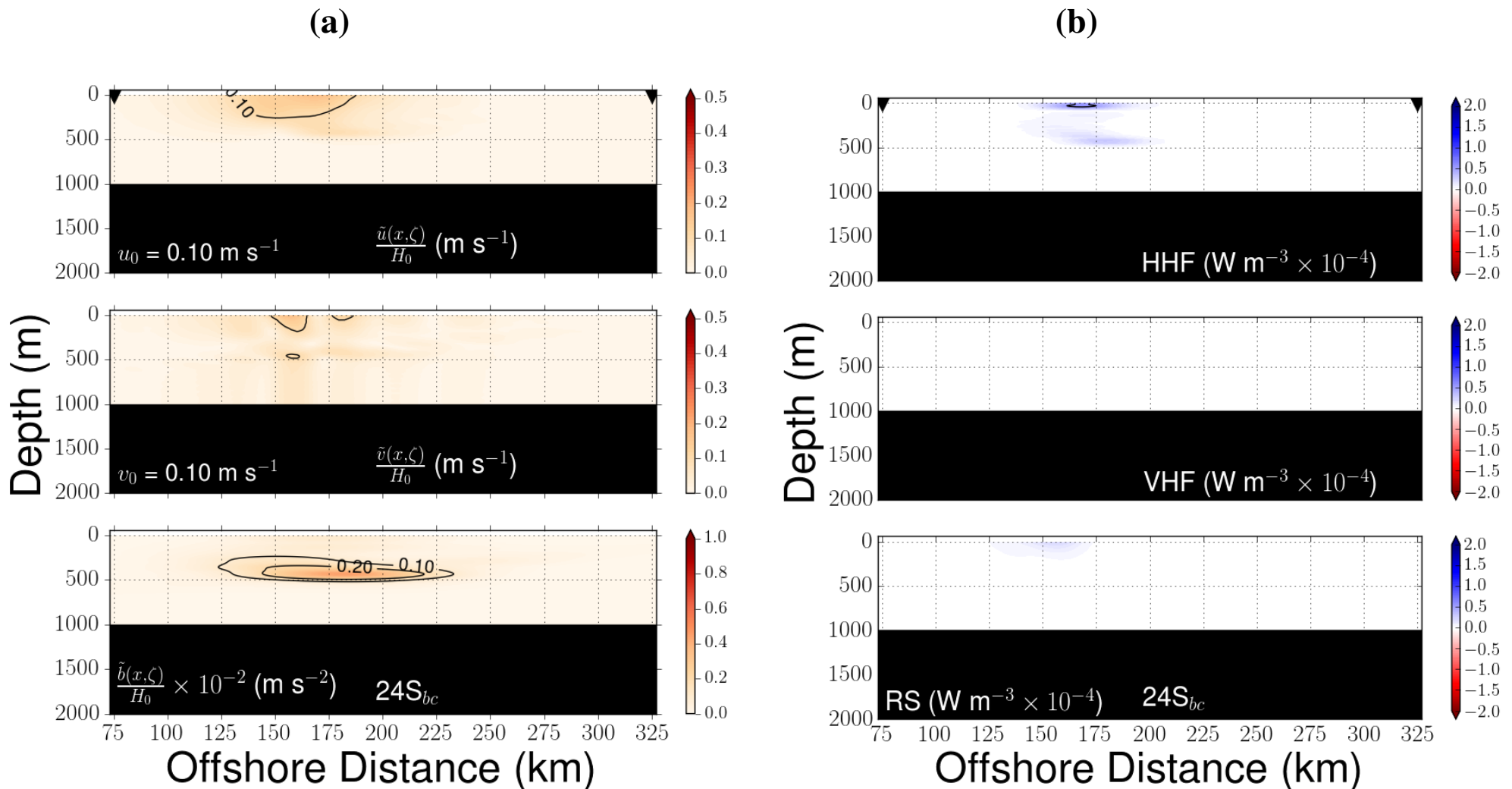


Figure B.2: **(a)** Amplitudes of the perturbations fields ($\frac{\hat{u}(x,\zeta)}{H_0}$, $\frac{\hat{v}(x,\zeta)}{H_0}$ and $\frac{\hat{b}(x,\zeta)}{H_0}$) and **(b)** energy conversion terms HHF, VHF and RS from experiment $24S_{bc}$. Since this experiment had its horizontal boundaries extended we indicated the original area limits with the black triangles in the upper panels.

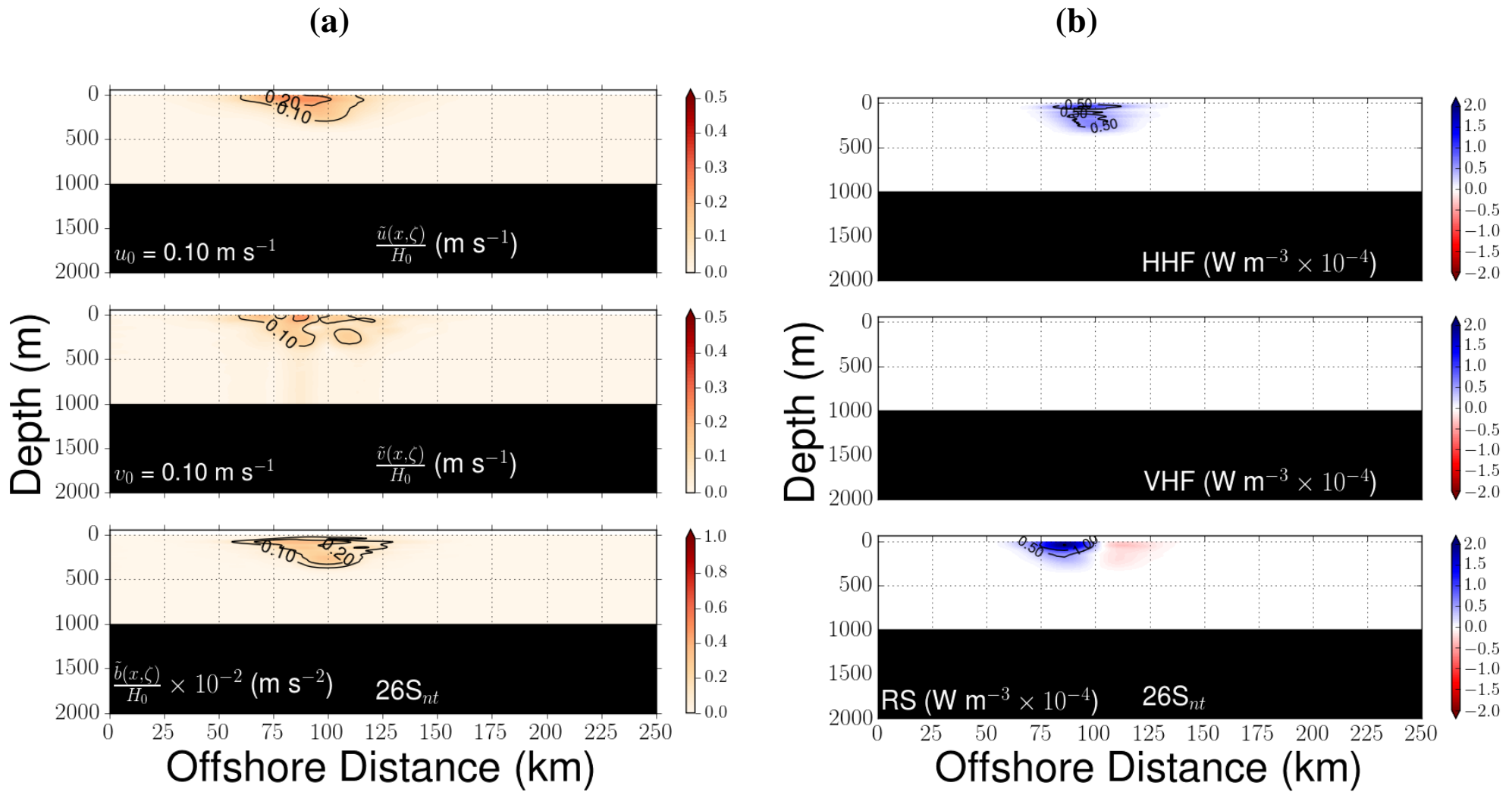


Figure B.3: **(a)** Amplitudes of the perturbations fields ($\frac{\tilde{u}(x,\zeta)}{H_0}$, $\frac{\tilde{v}(x,\zeta)}{H_0}$ and $\frac{\tilde{b}(x,\zeta)}{H_0}$) and **(b)** energy conversion terms HHF, VHF and RS from experiment $26S_{nt}$.

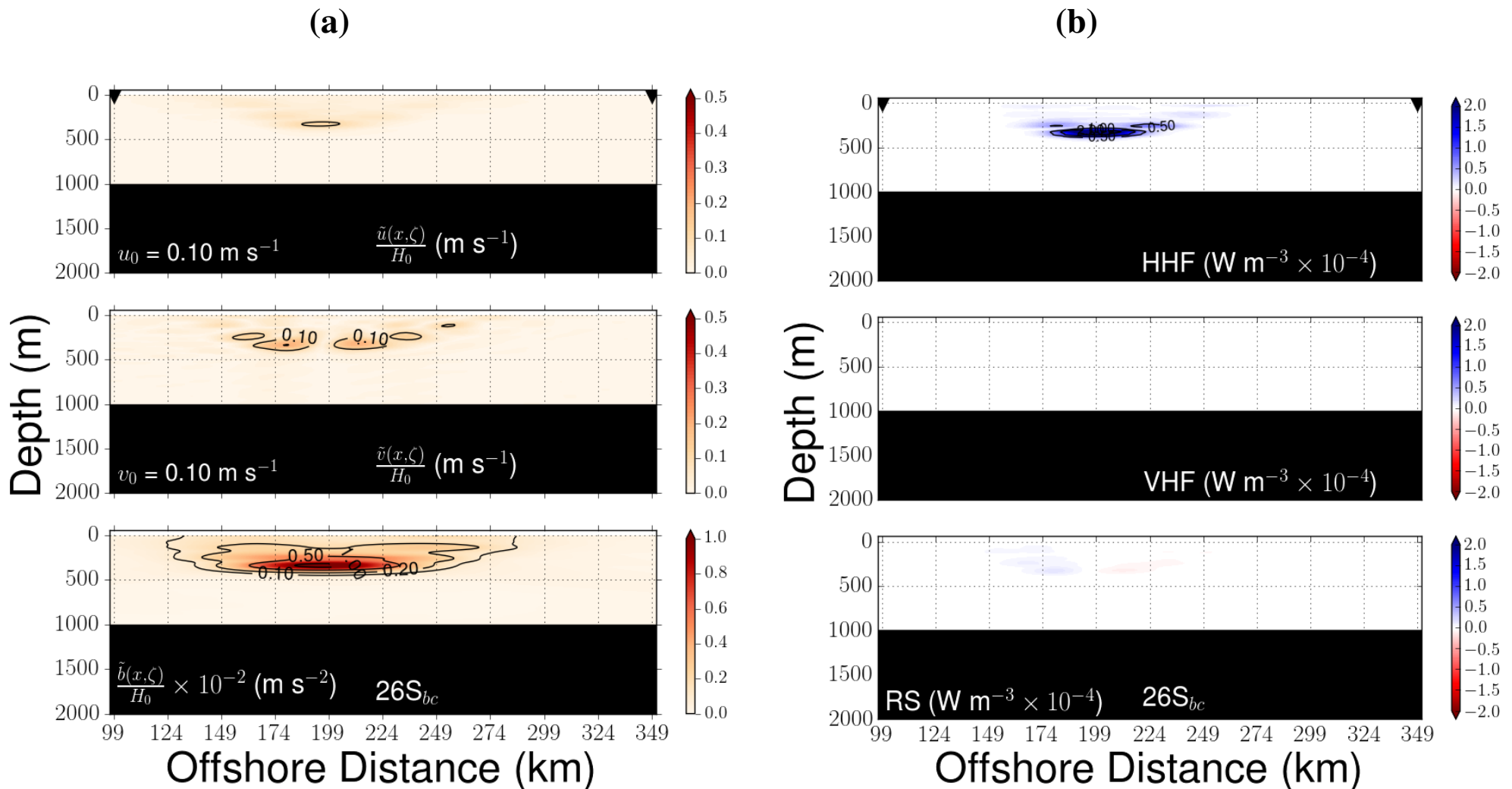


Figure B.4: **(a)** Amplitudes of the perturbations fields ($\frac{\tilde{u}(x,\zeta)}{H_0}$, $\frac{\tilde{v}(x,\zeta)}{H_0}$ and $\frac{\tilde{b}(x,\zeta)}{H_0}$) and **(b)** energy conversion terms HHF, VHF and RS from experiment $26S_{bc}$. Since this experiment had its horizontal boundaries extended we indicated the original area limits with the black triangles in the upper panels.

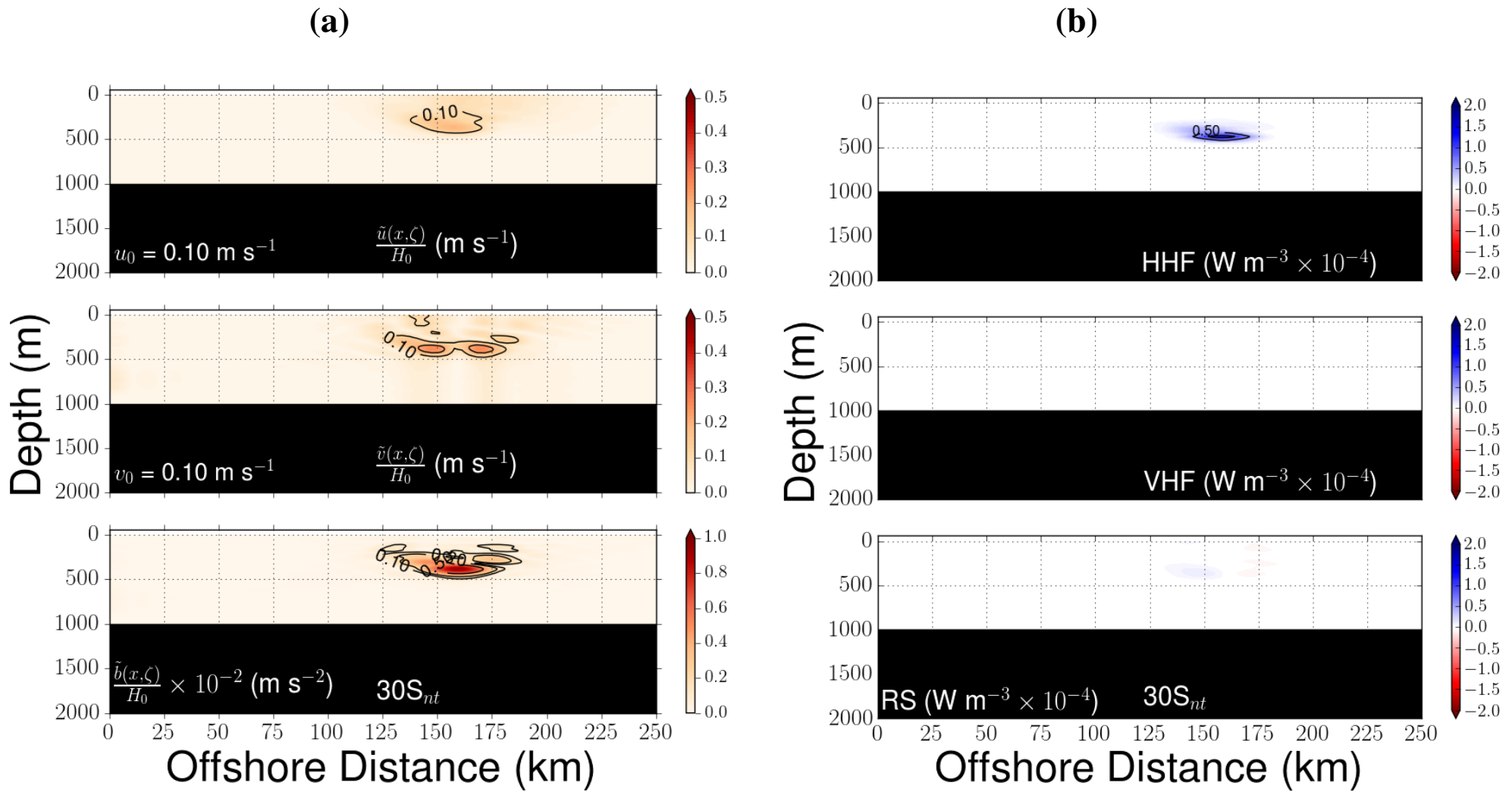


Figure B.5: **(a)** Amplitudes of the perturbations fields ($\frac{\tilde{u}(x,\zeta)}{H_0}$, $\frac{\tilde{v}(x,\zeta)}{H_0}$ and $\frac{\tilde{b}(x,\zeta)}{H_0}$) and **(b)** energy conversion terms HHF, VHF and RS from experiment 30S_{nt}.

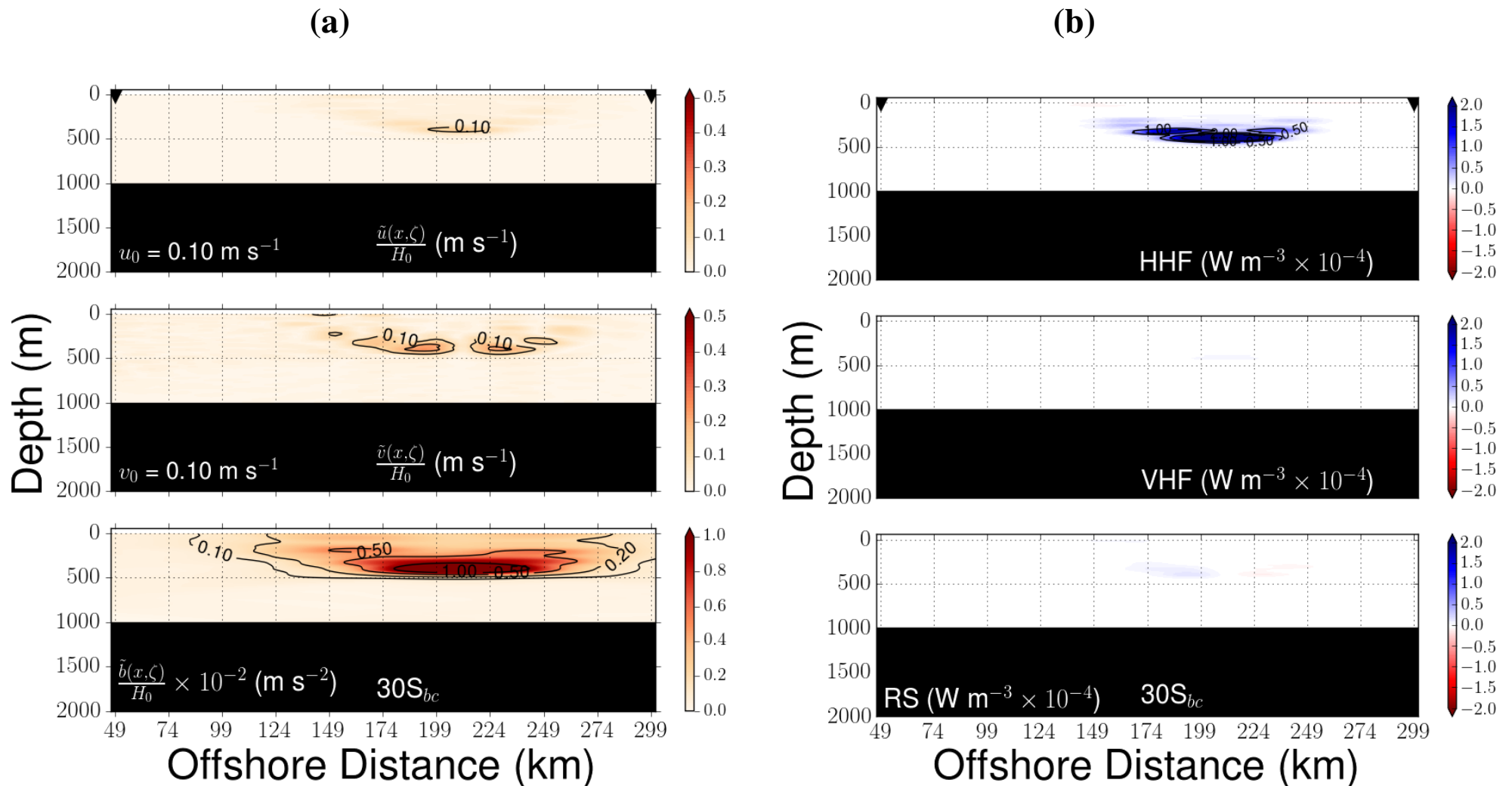


Figure B.6: **(a)** Amplitudes of the perturbations fields ($\frac{\tilde{u}(x,\zeta)}{H_0}$, $\frac{\tilde{v}(x,\zeta)}{H_0}$ and $\frac{\tilde{b}(x,\zeta)}{H_0}$) and **(b)** energy conversion terms HHF, VHF and RS from experiment $30S_{bc}$. Since this experiment had its horizontal boundaries extended we indicated the original area limits with the black triangles in the upper panels.

Bibliography

- Amante, C., and B. W. Eakiins (2009),ETOPO1 1 Arc-Minute Global Relief Model: Procedures, Data Sources and Analysis, NOAA Technical Memorandum NESDIS NGDC-24, national Geo-physical Data Center, NOAA. doi:10.7289/V5C8276M [acessed in June 2013].
- Biló, T. C., I. C. A. da Silveira, W. C. Belo, B. M. Castro, and A. R. Piola (2014), Methods for estimating the velocities of the Brazil Current in the pre-salt reservoir area off southeast Brazil, *Ocean Dynam.*, 64, 1431–1446.
- Boebel, O., R. E. Davis, M. Ollitrault, R. G. Peterson, P. L. Richardson, C. Schmid, and W. Zenk (1999), The Intermediate Depth Circulation of the Western South Atlantic, *Geophys. Res. Lett.*, 26(21), 3329–3332.
- Braga, E. S., V. C. Chiozzini, G. B. B. Berbel, J. C. C. Maluf, V. M. C. Aguiar, M. Charo, D. Molina, S. I. Romero, and B. B. Eichler (2008), Nutrient distributions over the Southwestern Atlantic continental shelf from Mar del Plata (Argentina) to Itajaí (Brazil): Winter-summer aspects, *Cont. Shelf Res.*, 28, 1649–1661.
- Bretherton, F. P., R. E. Davis, and C. B. Fandry (1976), A technique for objective analysis and design of oceanographic experiments applied to MODE 73, *Deep-Sea Res.*, 23, 559–582.
- Campos, E. J. D., J. E. Gonçalves, and Y. Ikeda (1995), Water mass characteristics and geostrophic circulation in the South Brazil Bight: Summer of 1991, *J. Geophys. Res.*, 100(C9), 18,537–18,550.
- Campos, E. J. D., Y. Ikeda, B. M. Castro, S. A. Gaeta, J. A. Lorenzetti, and M. R. Stevenson (1996), Experiment Studies Circulation in the Western South Atlantic, 77(27), 253–264.
- Campos, E. J. D., D. Velhote, and I. C. A. Silveira (2000), Shelf break upwelling driven by the Brazil Current meanders, *Geophys. Res. Lett.*, 27(6), 751–754.
- Castelao, R. M., E. J. D. Campos, and J. R. Miller (2004), A modelling Study of Coastal Upwelling Driven by Wind and Meanders of the Brazil Current, *J. Coast. Res.*, 20(3), 662–671.
- Castro, B. M., and L. B. de Miranda (1998), *The Sea. The Global Coastal Ocean - Regional Studies and Syntheses*, vol. 11, chap. Physical oceanography of the Western Atlantic continental shelf located between 4°N and 34°S coastal segment, pp. 209–251, A R Robinson and K H Brink.
- Cerda, C., and B. M. Castro (2014), Hydrographic climatology of the South Brazil Bight shelf water between São Sebastião (24°S) and Cabo São Tomé (22°S), *Cont. Shelf Res.*, 89, 5–14.

- Chen, C. (1989), The Structure of the Kuroshio West of Kyushu, Master's thesis, Massachusetts Institute of Technology and Woods Hole Oceanographic Institution.
- Chen, R., G. R. Flierl, and C. Wunsch (2014), A Description of Local and Nonlocal Eddy-Mean Flow Interaction in a Global Eddy-Permitting State Estimate, *J. Phys. Oceanogr.*, 44, 2336–2352.
- Cushman-Roisin, B., and J.-M. Beckers (1994), *Introduction to Geophysical Fluid Dynamics: Physical and Numerical Aspects*, International Geophysics Series, vol. 101, 2nded., Elsevier.
- Emery, W. J., and R. E. Thomson (2001), *Data Analysis Methods in Physical Oceanography*, Elsevier, Amsterdam.
- Emilson, I. (1961), The shelf and coastal waters of the Southern Brazil, *Bolm. Inst. Oceanogr.*, 7(2), 101–112.
- Evans, D. L., and S. R. Signorini (1985), Vertical structure of the Brazil Current, *Nature*, 315, 48–50.
- Evans, D. L., S. R. Signorini, and L. B. Miranda (1983), A note on the transport of the Brazil Current, *J. Phys. Oceanogr.*, 13(9), 1732–1738.
- Fernandes, A. M., I. C. A. da Silveira, L. Calado, E. J. D. Campos, and A. M. Paiva (2009), A two-layer approximation to the Brazil Current-Intermediate Western Boundary Current System between 20°S and 28°S, *Ocean Modeling*, 29, 154–158.
- Fischer, J., and M. Visbeck (1993), Deep Velocity Profiling with Self-contained ADCPs, *J. Atmos. Oc. Tech.*, 10, 764–773.
- Flierl, G. R. (1999), Thin jet and contour dynamics models of the Gulf Stream meandering, *Dynam. Atmos. Oceans*, 29(2), 189–215.
- Garfield, N. (1990), The Brazil Current at subtropical latitudes, Ph.D. thesis, University of Rhode Island, Rhode Island.
- Gille, S. T. (2003), Float observations of the Southern Ocean. Part I: Estimating mean fields, bottom velocities, and topographic steering, *J. Phys. Oceanogr.*, 33, 1167–1181.
- Godoi, S. S. (2005), Dinâmica Quase-Geostrófica do Sistema Corrente do Brasil no Embaixamento de São Paulo (23,5°- 27°S), Ph.D. thesis, Instituto Oceanográfico da Universidade de São Paulo.
- Grasshoff, K., M. Ehrhardt, and K. Kremling (1983), *Methods of Seawater Analysis*, second ed., Verlag Charmie.
- Hogg, N. G., G. Siedler, and W. Zenk (1999), Circulation and Variability at the Southern Boundary of the Brazil Vasin, *J. Phys. Oceanogr.*, 29, 145–157.
- James, C. (1996), Kuroshio Instabilities in the East of China Sea - Observations, Modeling, and Comparison with the Gulf Stream, Ph.D. thesis, University of Rhode Island.

- James, C., M. Wimbush, and H. Ichikawa (1999), Kuroshio Meanders in the East China Sea, *J. Phys. Oceanogr.*, 29, 259–272.
- Johns, W. E. (1988), One-dimensional baroclinically unstable waves on the Gulf Stream potential vorticity gradient near Cape Hatteras, *Dynam. Atmos. Oceans*, 11, 323–350.
- Killworth, P. D. (1980), Barotropic and Baroclinic Instability in Rotating Stratified Fluids, *Dynam. Atmos. Oceans*, 4, 143–184.
- Legeais, J.-F., M. Ollitrault, and M. Arhan (2013), Lagrangian observations in the Intermediate Western Boundary Current of the South Atlantic, 85, 109–126.
- Legeckis, R., and A. L. Gordon (1982), Satellite observations of the Brazil and Falkland currents - 1975 to 1976 and 1978, *Deep-Sea Res.*, 29(3A), 375–401.
- Lima, J. A. M. (1997), Oceanic circulation on the Brazil Current shelf break and slope at 22°S, Ph.D. thesis, university of New South Wales, New South Wales.
- Lorenzzetti, J. A., J. L. Stech, W. L. M. Filho, and A. T. Assireu (2009), Satellite observation of Brazil Current inshore thermal front in the SW South Atlantic: Space/time variability and sea surface temperatures, *Cont. Shelf Res.*, 29(17), 2061–2068.
- Luther, M. E., and J. M. Bane (1985), Mixed Instabilities in the Gulf Stream over the Continental Slope, *J. Phys. Oceanogr.*, 15, 3–23.
- Mano, M. F., A. M. Paiva, A. R. T. Jr., and A. L. G. A. Coutinho (2009), Energy Flux to a Cyclonic Eddy off Cabo Frio, Brazil, *J. Phys. Oceanogr.*, 39, 2999–3010.
- Matano, R. P., E. D. Palma, and A. R. Piola (2010), The influence of the Brazil and Malvinas Currents on the Southwestern Atlantic Shelf circulation, *Ocean Sci.*, 6, 983–995.
- Matano, R. P., V. Combes, A. R. Piola, R. Guerrero, E. D. Palma, P. T. Strub, C. James, H. Fenco, Y. Chao, and M. Saraceno (2014), The salinity signature of the cross-shelf exchanges in the Southwestern Atlantic Ocean: Numerical simulations, *J. Geophys. Res-Oceans*, 119(11), 7949–7968.
- Mémery, L., M. Arhan, X. A. Alvarez-Salgado, M. J. Messias, H. Mercier, C. G. Castro, and A. F. Rios (2000), The water masses along the western boundary of the south and equatorial Atlantic, *Prog. Oceanogr.*, 47(1), 69–98.
- Miranda, J. A. (2013), Dynamics of Brazil Current dipoles: barotropic instabilities and flow-topography interactions, Ph.D. thesis, University of São Paulo, São Paulo.
- Miranda, L. B., and B. M. C. Filho (1979), Condições do movimento geostrófico das águas adjacentes a Cabo Frio (RJ), *BOLETIM DO INSTITUTO OCEANOGRÁFICO*, 28(2), 79–93.
- Moore, G. W. K., and W. R. Peltier (1987), Cyclogenesis in Frontal Zones, *J. Atmos. Sci.*, 44, 384–409.

- Müller, T. J., Y. Ikeda, N. Zangenberg, and L. V. Nonato (1998), Direct Measurements of Western Boundary Currents off Brazil Between 20°S and 28°S, *J. Geophys. Res.*, 103(C3), 5429–5437.
- Ni, B. (1996), Temporal, Spacial and Pulse Instabilities of the Gulf Stream, Ph.D. thesis, Massachusetts Institute of Technology and Woods Hole Oceanographic Institution.
- Oliveira, L. R., A. R. Piola, M. M. Mata, and I. D. Soares (2009), Brazil Current surface circulation and energetics observed from drifting buoys, *J. Geophys. Res.*, 114(C10006).
- Palma, E. D., R. P. Matano, and A. R. Piola (2004), A numerical study of the Southwestern Atlantic Shelf circulation: Barotropic response to tidal and wind forcing, *J. Geophys. Res.*, 109(C08104).
- Palma, E. D., R. P. Matano, and A. R. Piola (2008), A numerical study of the Southwestern Atlantic Shelf circulation: Stratified ocean response to local and offshore forcing, *J. Geophys. Res.*, 113(C11010).
- Pedlosky, J. (1964), The Stability of Currents in the Atmosphere and the Ocean: Part I, *J. Atmos. Sci.*, 21, 201–219.
- Pedlosky, J. (1987), *Geophysical Fluid Dynamics*, second ed., Springer.
- Piola, A. R., E. J. D. Campos, O. O. Moller, M. Charo, and C. Martinez (2000), Subtropical Shelf Front off eastern South America, *J. Geophys. Res.*, 105(C3), 6565–6578.
- Piola, A. R., S. I. Romero, and U. Zajaczkovski (2008), Space-time variability of the Plata plume inferred from ocean color, *Cont. Shelf Res.*, 28, 1556–1567.
- Preisendorfer, R. W. (1988), *Principal Component Analysis in Meteorology and Oceanography*, Elsevier, Amsterdam.
- Preu, B., F. J. Hernández-Molina, R. Violante, A. R. Piola, C. M. Paterlini, T. Schwenk, I. Voigt, S. Krastel, and V. Spiess (2013), Morphosedimentary and hydrographic features of the northern Argentine margin: The interplay between erosive, depositional and gravitational processes and its conceptual implications, 75, 157–174.
- Rocha, C. B., A. Tandon, I. C. A. Silveira, and J. A. M. Lima (2013), Traditional quasi-geostrophic modes and surface quasi-geostrophic solutions in the Southwestern Atlantic, *J. Geophys. Res.-Oceans*, 118, 1–12.
- Rocha, C. B., I. C. A. da Silveira, B. M. Castro, and J. A. M. Lima (2014), Vertical structure, energetics and dynamics of the Brazil Current System at 22°S-28°S, *J. Geophys. Res-Oceans*, doi: 10.1002/2013JC009143.
- Rodrigues, R. R., L. M. Rothstein, and M. Wimbush (2007), Seasonal Variability of the South Equatorial Current Bifurcation in the Atlantic Ocean: A Numerical Study, *J. Phys. Oceanogr.*, 37, 16–30.
- Sato, R. M. (2014), O meandramento ciclônico da Corrent do Brasil ao largo do Cabo de Santa Marta (~28,5°S), Master's thesis, Instituto Oceanográfico da Universidade de São Paulo.

- Schmidt, A. C. K., W. C. Belo, I. C. A. Silveira, and J. A. M. Lima (2007), Modelo Paramétrico Analítico para a Estrutura de Velocidade do Sistema Corrente do Brasil, *Rev. Bras. Geofis.*, 25(1), 75–91.
- Schott, F. A., M. Dengler, R. Zantopp, L. Stramma, J. Fischer, and P. Brandt (2005), The Shallow and Deep Western Boundary Circulation of the South Atlantic at 5°-11°S, *J. Phys. Oceanogr.*, 35, 2031–2053.
- Signorini, S. R. (1978), On the circulation and the volume transport of the Brazil Current between the Cape of São Tomé and Guanabara Bay, *Deep-Sea Res.*, 5(25), 481–490.
- Silveira, I. C., J. A. M. Lima, A. C. K. Schimdt, W. Ceccopieri, A. Satori, C. P. F. Francisco, and R. F. C. Fontes (2008), Is the meander growth in the Brazil Current System off Southeast Brazil due to baroclinic instability?, *Dynam. Atmos. Oceans*, 45, 187–207.
- Silveira, I. C. A., A. C. K. Schimdt, E. J. D. Campos, S. S. de Godoi, and Y. Ikeda (2001), A Corrente do Brasil ao largo da costa leste brasileira, *R. bras. Oceanogr.*, 48(2), 171–183.
- Silveira, I. C. A., L. Calado, B. M. de Castro, M. Cirano, J. A. M. Lima, and A. S. Mascarenhas (2004), On the Baroclinic Structure of the Brazil Current-Intermediate Western Boundary Current at 22°-23°S, *Geophys. Res. Lett.*, 31, 4308.
- Soutelino, R. G., A. Gangopadhyay, and I. C. A. da Silveira (2013), The roles of vertical shear and topography on the eddy formation near the site of origin of the Brazil Current, *Cont. Shelf Res.*, 70, 46–60.
- Stommel, H. (1965), *The Gulf Stream: A Physical and Dynamical Description*, University of California Press.
- Stramma, L. (1989), The Brazil Current transport south of 23°S, *Deep-Sea Res.*, 36(4A), 639–646.
- Stramma, L., and M. England (1999), On the wather masses and mean circulation of the South Atlantic Ocean, *J. Geophys. Res.*, 104(C9), 20,863–20,883.
- Talley, L. D., G. L. Pickard, W. J. Emery, and J. H. Swift (2011), *Descriptive Physical Oceanography: An Introduction*, sixth ed., Academic Press.
- Vianna, M. L., and V. V. Menezes (2011), Double-celled subtropical gyre in the South Atlantic Ocean: Means, trends and interannual changes, *J. Geophys. Res.*, 116(C03024).
- Visbeck, M. (2002), Deep Velocity Using Acoustic Doppler Current Profilers: Botton Track and Inverse Solutions, *J. Atmos. Oc. Tech.*, 19, 794–807.
- Xue, H., and G. Mellor (1993), Instability of the Gulf Stream front in the South Atlantic Bight, *J. Phys. Oceanogr.*, 23, 2326–2350.
- Zemba, J. C. (1991), The structure and transport of the Brazil Current between 27°and 36°South, Ph.D. thesis, Massachusetts Institute of Technology and Woods Hole Oceanographic Institution.